A COMPUTER CONTROLLED FILAMENT WINDING TECHNIQUE FOR MANUFACTURING CEMENT BASED COMPOSITE LAMINATES

by

Andrew Pivacek

A Thesis Presented in Partial Fulfillment
of the Requirements for the Degree
Master of Science

ARIZONA STATE UNIVERSITY

May, 2001

A COMPUTER CONTROLLED FILAMENT WINDING TECHNIQUE FOR MANUFACTURING CEMENT BASED COMPOSITE LAMINATES

by

Andrew Pivacek

has been approved

May, 2001

APPROVED:

_____,Chairperson

_____

_____

Supervisory Committee

ACCEPTED:

_____

Department Chairperson

_____

Dean, Graduate College

ABSTRACT

A filament winding system was developed for manufacturing various types of fiber/cement composite materials. The computer controlled system is easily configured to construct uniaxial composite laminates, cross and angle ply laminates, pipes, wraps, and pultruded sections. The electrical and mechanical system components are discussed in detail. Manufacturing process parameters such as impregnation, pressing, and additives are investigated.

The present system made various cement based composite laminates using continuous alkali-resistant (AR) glass and polypropylene fibers. Closed loop uniaxial tensile and third point flexure tests measured composite mechanical responses. Results indicate that uniaxial tensile strength exceeded 50 MPa using 4.5% AR glass fibers. The ultimate tensile strain capacity was increased to more than 2% for AR glass fiber composite by varying the stacking sequences. Ultimate tensile strength for uniaxial polypropylene with 7% fibers reached 18 MPa at a strain capacity of 8.5% without composite failure. Uniaxial AR glass flexural proportional elastic limit averaged 11MPa at a deflection of 1 mm. Modulus of rupture stress reached 50 MPa with a deflection exceeding 5 mm. Tension and flexural toughness measurements were conducted.

Stable microcracking was achieved in uniaxial AR glass and polypropylene composites. Debonding was the main microstructural factor of AR glass composite failure. Experimental observations and results were compared with the ply discount method and indicate that current composite materials theories can be easily adopted for design and analysis of cement based composite laminate systems.

ACKNOWLEDGMENTS

I am deeply grateful to my committee chair, Dr. Barzin Mobasher, for his guidance, expertise, and considerable patience. I would also like to extend thanks to Dr.Rajan, Dr. Mamlouk, Henry Anderson, Fred Sierra, Walter Bernaultis, Reza Rajabian, and the entire ELS staff for their continual technical and moral support. I would also like to acknowledge Marc Castagna, David White, and Tim Karcher for their assistance with the imaging system. Finally, I dedicate this to my parents for having me, without which this entire endeavor would have been obviously impossible.

TABLE OF CONTENTS

LIST OF TABLES

.

LIST OF FIGURES

Figure Page

Figure Page

CHAPTER 1

Introduction

1.1 Overview

The most widely used construction/structural material in the world is concrete averaging into the billions of tons per year. Any improvement in concrete's performance becomes economically promising. Concrete's popularity is from its desirable properties of strength in compression, stiffness, durability in hostile environmental conditions, and its ability to be formed into any shape desired. If proportioned, mixed, placed, finished, and cured properly the concrete becomes extremely resistant to degradation of these properties. This enables concrete to retain its strength, abrasion resistance, resistance to hostile environments, and other valuable properties for extensive periods of time.

Concrete does have some undesirable mechanical properties that limit its structural applications. Concrete, and especially the cement paste, have low toughness and tensile capacity. The fracture resistance and elastic/plastic properties of any material depend on the nature of the heterogeneous microstructure (1). The resistance to crack growth in the matrix of the concrete is due to the presence of the aggregates. If unbroken, the aggregates can increase toughness by bridging crack tip and forcing a more torturous crack growth path. However concrete contains many inherent flaws from porosity, improper bonding, shrinkage, and unhydrated cement that can develop into minute cracks under loading conditions. Under these conditions there exists a good potential for cracks sites, growth, and early failure with cured concrete matrix (1). This

creates a higher safety factor and therefore a greater consumption of material per application.

The idea of using discontinuous fibers to limit crack growth has recently received more attention. The use of fibers dates back as far as the Egyptian civilization using straw in mud bricks to control shrinkage cracking. Recently the use of small fibers of several material types have increased the tensile, flexural, and toughness properties that were so lacking. The fibers also increase the impact resistance, ductility, first-crack strength, flexural strength, and post-crack load resistance of the matrix (2). The fibers bridge the crack as it attempts to grow giving a closing force. This force depends on the fiber/matrix bond strength and the fibers tensile strength. Many of the fibers pullout of the matrix. All of these help to dissipate energy giving increased toughness and pseudo-ductility (3). The influence of the fibers depends on their type, aspect ratio, length, alignment, bond, percent volume in the matrix, and spacing in the matrix. Sometime in its structural life a section compromised of concrete will under go a tensile force. With fiber inclusion, the section can withstand the force with less probability of failure. With this ability, the durability and therefore quality and economic value of the material is enhanced.

The use of fibers in cement products was first developed around 1900 by Hatschek whose self-named process produced asbestos fiber reinforced boards. However the asbestos fibers have been found to be cancer causing making the need for a replacement to be sought out. Many producers have converted to use wood or polymer fiber reinforcement. The wood fibers decrease the overall weight of the product but the sugars it contains inhibit cement setting and curing. Their removal takes another process

expending more energy and cost. Also, the strength of the wood/cement composite decreases with time (4). Polymer fibers are classified into two sections, fibers with a lower elastic modulus than concrete, such as polypropylene, and fibers with a higher elastic modulus, such as carbon. At low volume the polymer fibers increase toughness greatly. However the fibers are still expensive due to manufacturing costs.

In the 1970's Alkali-Resistant (AR) glass fibers were developed and used to make Glass Fiber Reinforce Concrete (GFRC). The production method was based on simultaneous spraying of a mortar mix and chopped glass fibers into a precast mold. About 5% glass fibers were used by weight. The units were sold as architectural cladding panels for large structures. The panels had a 28-day tensile strength of 12 MPa and a tensile strain of 1% at the peak tensile strength. This is about 100 times the strain capacity of plain cement.

Despite the alkali resistance the GFRC material shows drastic loss of strength, and ductility over time. The loss is attributed to two factors. The first is fiber integrity loss due to alkali attack and secondly the loss of straining capacity from the infilling of the porous interface zones by C-H hydration (1,5 & 6). The loss of these properties is measured in flexural and tensile tests (5). Many factors influence the rate of loss including weather exposure. The end result is that GFRC panel cannot be considered as load carrying units. Also, the fibers are expensive due to the zirconia compound (ZrO_2) included for alkali resistance needing a higher melt temperature in production (7).

The inclusion of a small percentage of randomly oriented fibers increases the post-peak load carrying capacity but does little to increase the strength of the composite. If a higher volume percentage of fibers is used the ultimate tensile and flexural strengths

as well as the strain capacity increase dramatically. Toughness is increased by orders of magnitude (4). Li used a high energy mixer and an extrusion machine to decrease porosity and produce better quality specimens of up to 16% fiber volume fraction. The additional volume also led to better crack control. In these composites, the cracking distributes over a small volume of material instead of a opening a discrete crack surface. This is due to the numerous fibers bridging the area and redistributing the stresses more efficiently. However, at 16% fiber volume fraction the composite contained excessive porosity reducing strength. Short glass fibers were used to increase the strength of concrete specimens by Marsh and improve the ultimate flexural strength over 5 times that of the unreinforced matrix (8). The strength increased as the fiber length increased from 1/2" to 2".

The aligning of continuous fibers is advantageous if a production technique can be developed. Polypropylene fibers were hand pultruded through a cement bath and aligned by Mobasher, Stang, & Shah to produce stable and wider spread microcracking in test specimens (9). The distributed microcracking increased the strain capacity and therefore the energy absorption or toughness of the composite. The entire section can be mobilized to resist the applied forces with this type of fiber inclusion. The pultrusion of fibers is a more efficient technique when compared to other FRC manufacturing methods in realizing the ultimate strength of the fibers more as shown in figure 1.1.

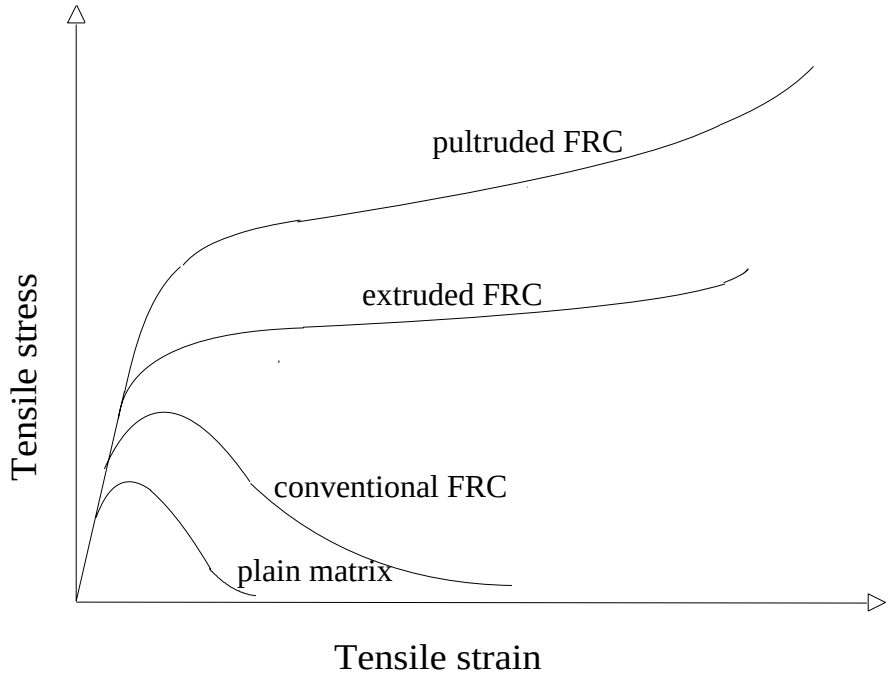

Figure 1.1 The efficiency of manufacturing techniques in FRC production.

Laminated composites were developed to increase the strength, stiffness, and performance of the composites. They consist of high strength and high modulus fibers encased in a matrix material. The fibers and matrix materials retain their properties and physical shape causing a distinct boundary between them. Together they achieve what neither could do on their own (10). Usually the fibers carry the load while the matrix protects them from damage and offers a stress transfer medium. Many of these composites consist of thin layers of oriented fibers called laminates, which are stacked together. The order of the stacking sequence and the fiber layer orientations can vary the overall properties of the composite greatly. Filament winding is one of the many types of production techniques used in plastic and epoxy composite production. The method leads to a composite of known properties and stable dimensions (7). A roving of material

is impregnated in a bath of matrix material and spun around a mold or mandrel. There usually is a guidance carriage to align the fibers on the mold as they are laid out (11).

The inclusion of pins in the matrix bath improves the impregnation of the roving. The pins diameter is equal to the roving's and is placed perpendicular to the roving path direction. It has been shown that four pins can increase impregnation of the roving to 100% with epoxy resins. The pressure of the fibers on the pins and the spreading of the fibers are factors in this increase (12). With the glass fibers the impregnation can also be improved by removing the sizing from the fiber bundle allowing it to spread out more easily. Running the roving through a clean water bath over pins and a draining bin effectively removes the sizing. The slightly wetted fibers will not dry their pathway in the cement bath removing the need for intense agitation.

Smart motion systems can be used to control a filament winding setup to increase the tolerances and reproducibility of products. A smart motion system was designed and implemented to automate composite production. The system consists of a feed, a guide, a take up (mold) section, an electrical support system, and a computer. The computer used LabView and Motion Architect to control a closed loop servo system that guided two encoded servomotors. System configuration determined the winding, pulling, and guidance of the composites, while the take up section controlled the fiber lamina orientation. Fiber distribution was uniform and the continuous and aligned state of the produced lamina provided a higher level of consistency and performance (13).

1.2 Statement of Problem

Since concrete is a common structural material, improvements in performance and reliability are always sought. Pultruded fiber/cement composites have displayed improved mechanical properties over other fiber/cement composites. Computer controlled manufacturing systems have produced more reliable components at a cheaper cost than man-made ones. By combining these two ideas an improvement in cement based composite behavior can be achieved. This can lead to material economy and more reproducible section properties. Our research effort will find if continuously aligned fiber cement composites can enhance material properties even more.

This study will concentrate on laminated cement based composites of different orientations, or lay-ups. Research aspects are based on mechanical property evaluation and processing procedures. Different fibers will be used at a constant volume fraction to identify varying mechanical properties and manufacturing methods for the differing laminated composites. Ten-percent silica fume, superplasticizer, and a retarder modify cement matrix rheology. A computer-controlled filament winding system is developed and incorporated to automate the manufacturing process. This insures repeatability of results and composite quality.

The composites will be tested in flexure and tension. The tests will be performed on a closed loop servo hydraulic system. Flexure tests will incorporate a single LVDT for center point deflection measurement in the third point flexure test. Tension tests will use two LVDTs mounted to specimen's opposing surfaces. The LVDT signal will be the feedback parameter controlling all tests.

CHAPTER 2

Experimental Setup

2.1 Introduction to the Filament Winding System

Computer aided manufacturing allows development of economic and versatile materials. The full potential of fibers as reinforcement in cement-based materials is enhanced by uniform placement and the use longer length fibers. Since the manufacturing technique is fully controlled the composite laminates can be designed for the specific service loads. This type of automation gives the ability to reproduce more of the same product with ease and consistency in final product performance.

The mechanical components of the system consists of the feed section, guide, and the take up sections as shown in figure 2.1 The electrical components consist of several servomotors, encoders, limit switches, and a computer. The computer uses object oriented programming languages to monitor a closed loop system that controls at least two servomotors. Configuration of the servomotors determines the winding, pulling, and guidance of the roving which influences the fiber volume fraction and their uniform spreading within the composite. The take up section controls the fiber (lamina) orientation and supplies the power to rotate the fiber spool. This generates tension in the roving throughout the wetting and draining, enhancing the process. Fiber orientation and fiber volume fraction greatly influence composite mechanical response.

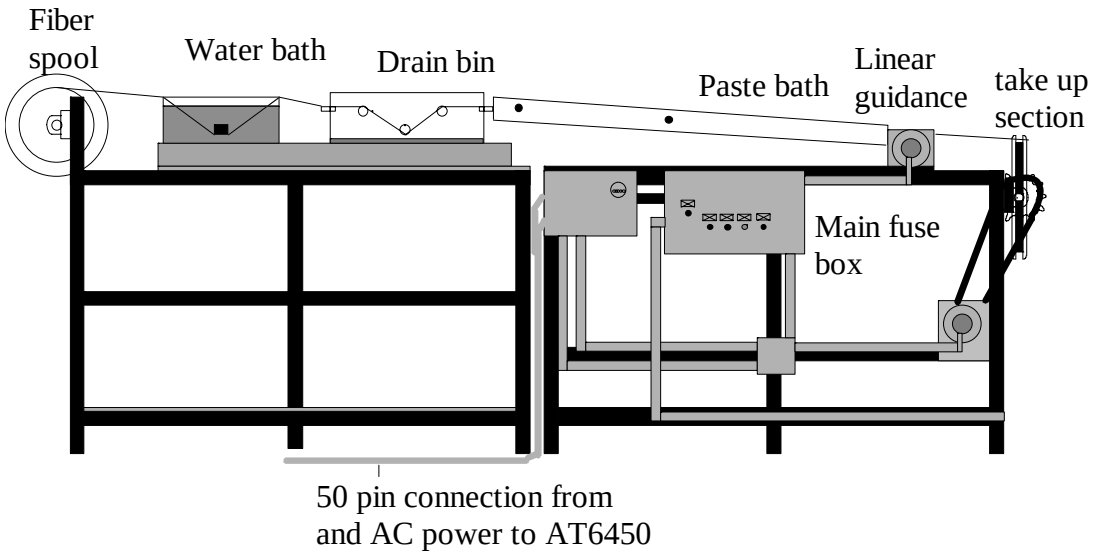

Figure 2.1 Side view of the filament winding system

2.2 Physical setup

2.2.1 Feed Section

The feed mechanism for this pultrusion system consists of a spool of fiber, a watering tank, a draining tank, and a cement paste bath. The spool and tanks rest on the feed table while the paste bath is connected to the end to the drain tank.

The center of the glass fiber spool is a 3” diameter hollow. Therefore a plastic cylinder made of a 2.5” inside diameter PVC tube with two unions fitted on each end was used to fill this void. The unions were friction fitted with a 1/2” thick Plexiglas disk with a centered 3/4” hole. A 3/4” diameter steel bar fits this opening and supports the entire spool apparatus. The polypropylene spool has a 3/4” hole and is therefore supported only by the steel bar.

Frictionless Browning bearings are attached to each end of the steel bar and are mounted to a unistrut arm extending 2’ above the feed table. The steel bar is leveled horizontally with the spool center resting 12” above the table height. Two aluminum

disks apply pressure on the spool ends keeping the fiber roving from wrapping around the bar or otherwise becoming entangled. The 10” diameter 3/8” thick disks have a 1 1/4” hexagon knuckle welded to their center on one side. A 3/4” centered hole was drilled through both the knuckle and disk for supporting bar access. The holding disks maintain the spool’s position with alan screws tightened to the steel bar. The steel bar is also held in position by alan screws located on the frictionless bearings.

The spool setup is pictured in figure 2.2. Power to rotate the spool is supplied by the take-up servomotor which it rotates the mold and pulls the roving. A manually adjustable variable speed AC motor with a chain sprocket can also supply power. The spool rotational speed is determined by the rotational speed of the take-up mold and the shrinking spool diameter as it loses material. Another way of feeding the fiber roving is to lay the spool on one of its circular ends on the ground and pulling the single loose roving from the center hole. No spool rotation is needed eliminating the need for a separate power supply. This eliminates the energy dissipated on the inertia of rotating the 40 lb glass spool and the friction in the bearings. However, the roving is twisted along its axis and these twists will be included in the composite lamina. It is known that twists increase the strength of the fiber/matrix bond (4). In this study only the rotation method was used.

The single macro fiber roving coming off the spool contains 30 main strands with each strand containing 204 single fibers. A sizing holds the 6,120 single fibers together.

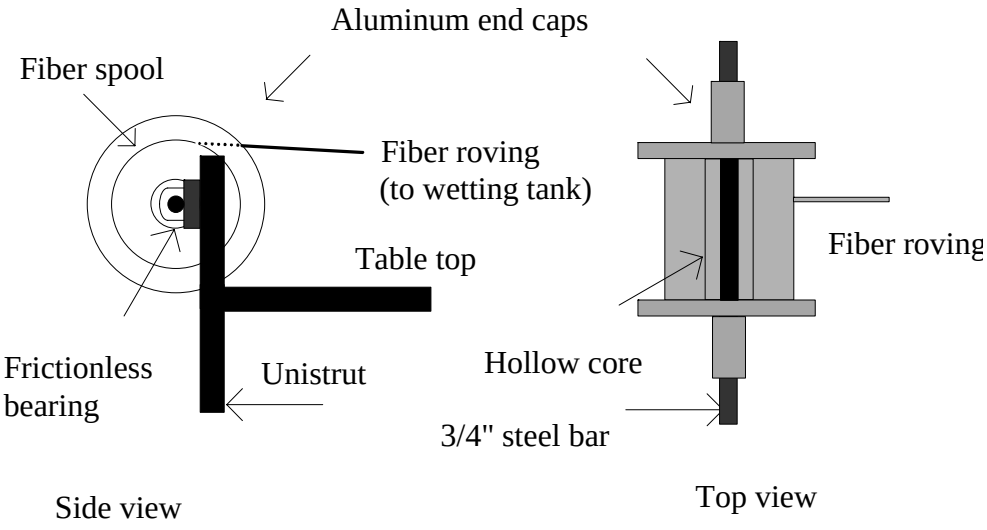

Figure 2.2 Side and top views of the fiber spool in the feed section.

The sizing binds the fibers inhibiting full impregnation. The water in the cement paste bath may also dissolve the sizing. This causes a premature hardening of the paste along the fiber pathway. The roving would then pass through the bath without any paste impregnation. Therefore the roving was wetted to remove the sizing and increase its impregnation capacity.

Pins or points of pressure allow more access to the interior of a roving for impregnation (14). This is accomplished by the spreading of the fiber roving and applying pressure between the moving fibers and the steel rods. This concept was used in

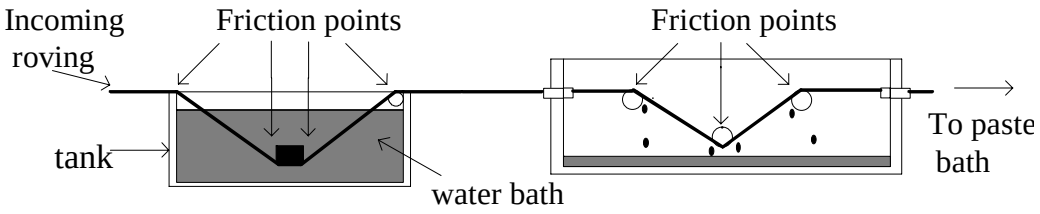

Figure 2.3 Side view of the wetting and drain tanks in the feed section.

the water tank and fiber path design as seen in the figure 2.3. The water has more access to dissolve the sizing as the fiber path traverses through the pressure points. Steel rods and bars were used for the pressure points because the fiberglass's frictional abrasive characteristics. The water in the tank is replaced after the manufacture of a single specimen.

After being wetted down, the roving then passes through an empty tank weaving through three steel bars. The water/sizing mixture left on the fibers is partially squeezed off by the pressure of the passing fibers on the bars. This process provided further fiber separation from the roving and allowed for a reduction in the water/cement ratio of cement paste bath. Without the drain tank the excess water on the roving would dilute the cement paste. One specimen run usually left 1-2" of the water/sizing mixture at the 24" x 16" tank bottom. The sizing removal and the enhanced fiber separation increased the fiber contact surface in the paste bath, resulting in a higher degree of fiber roving impregnation.

At the end of the drain tank a 1.5 m long 10 cm diameter PVC tube was installed containing a cement paste with a 0.3~0.35 w/c ratio. This is the paste bath that

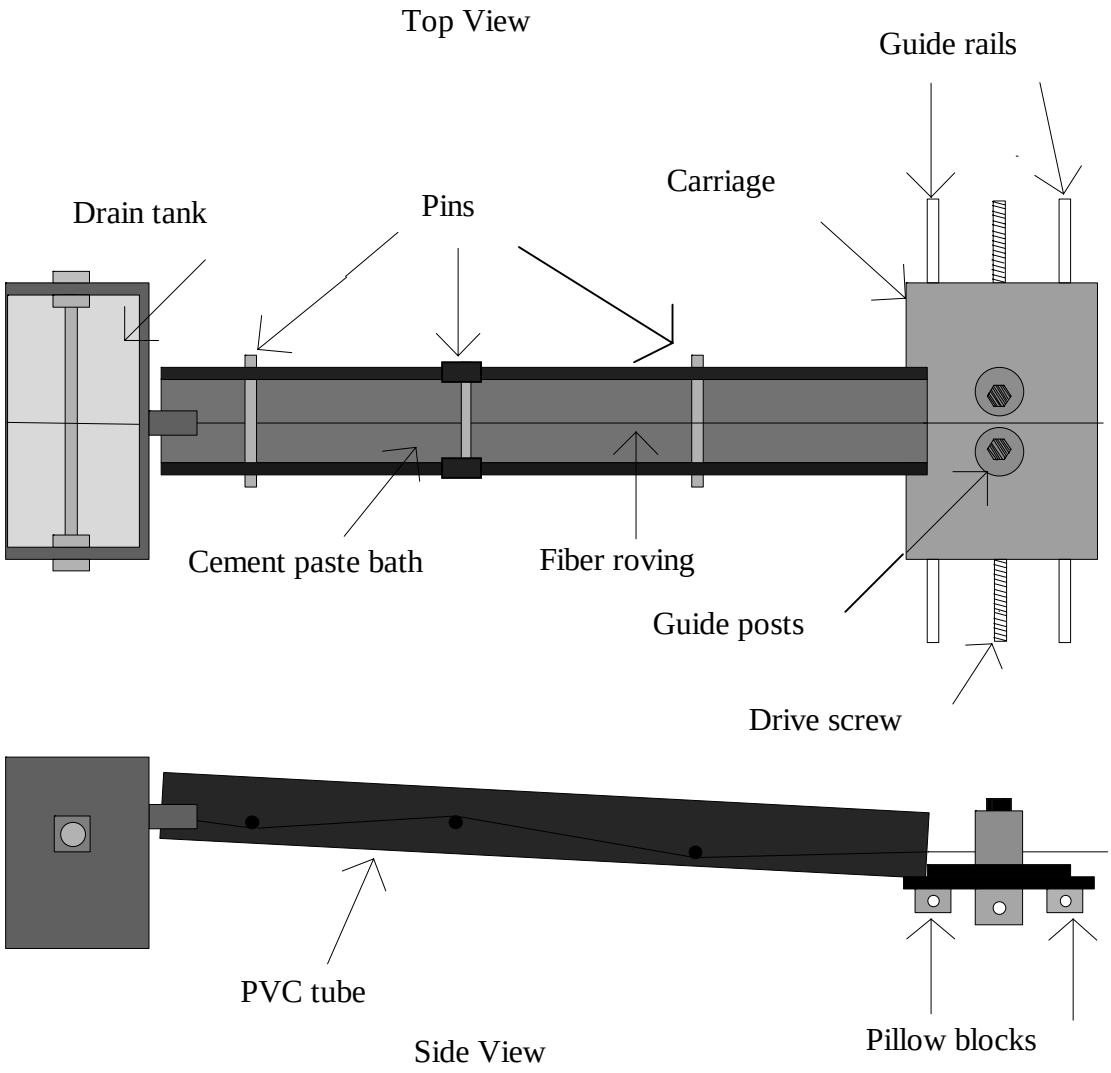

Figure 2.4 Top and side views of the cement paste bath tube in the feed section.

impregnates the roving and is shown in figure 2.4. This tube is cut in half lengthwise and contains three pins along the path of fibers for increased impregnation (12). The guide table of linear guidance system supports the tube's end.

2.2.2 Guidance Section

To align the fiber roving onto the molds, two AC Powerslides from Thompson Industries, Inc. were used to make a linear position system with a carriage assembly.

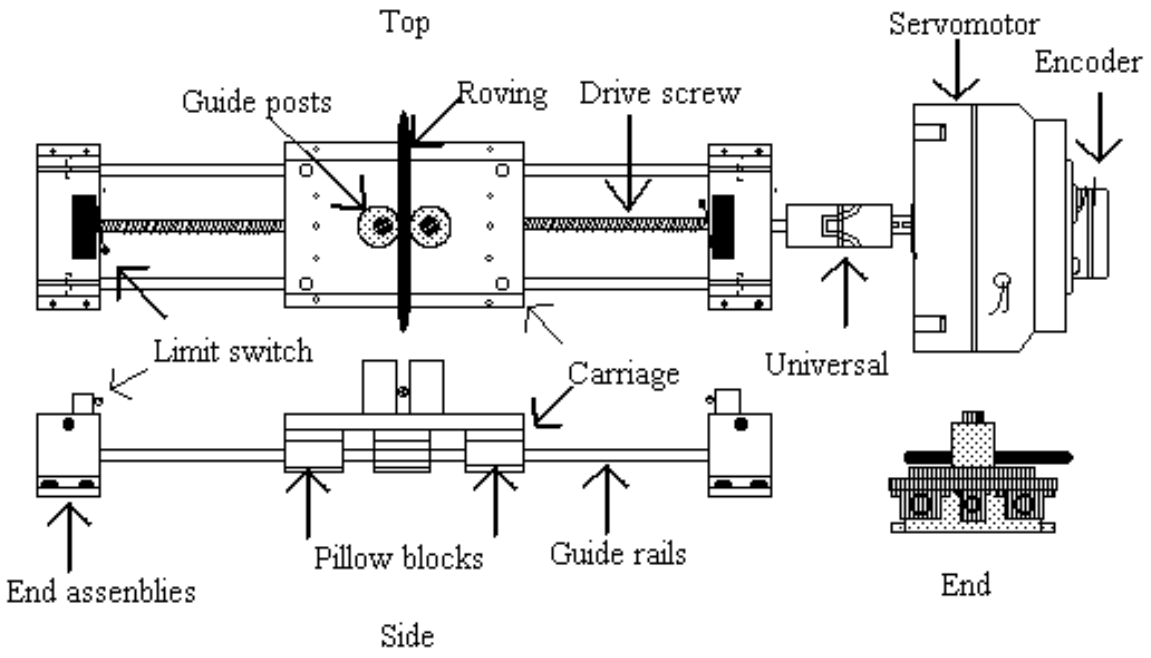

Figure 2.5 Top, side, and end view of the linear guidance section.

This guidance section has a double shaft integrated end supported system with a ball screw assembly and carriage and is pictured figure 2.5. A servomotor and encoder supply power and control through a universal connection.

The end assemblies have angular ball bearings and support a drive screw that is a precision machined 10 thread per 25 mm sleeve over a 9.5 mm bar. The flat carriage is supported by four ball bushing frictionless bearing pillow blocks on two solid guide rails and by the ball screw assembly/drive screw interface. A direct drive servomotor with an 80:1 gear reduction ratio powers the drive screw rotation. The motor pushes the ball screw assembly connected to the carriage. The carriage slides along guide arms giving

rise to the linear motion of 45 cm range. Two 25 mm diameter 50 mm high steel cylindrical posts are bolted to the top of the carriage with a 9.5 mm gap between them. The roving leaves the cement paste tube resting on the carriage and passes through this gap. Movement of the system controls the tube end. The posts hold the roving perpendicular to the take up direction, keeping the ply fibers positioned on the mold.

An optical encoder mounted to the back of the servomotor monitors the distance, velocity, and acceleration of the drive shaft during operation. The velocity of the take-up servomotor determines the amount of fibers applied to a section of the mold. Encoder control and precision screw assembly give a high accuracy of the actual distance traveled across the mold and the fiber amount when compared to the programmed values.

On the top of the each end assembly limit switches were installed for hardware safety and the ability to terminate motion before the carriage would contact the end assemblies. The switches are placed to stop motion 3 mm before contact and are software controlled for enabling and disabling. Once activated, the servomotor is stopped instantly with no deceleration. Only motion in the opposite direction can be initiated with the controlling software automatically re-enabling the limit switch error capability. This setup prevents catastrophic damage to the precision sleeves and end assemblies. The safety system is needed because the torque limits on this powerful servomotor are too high for the medium load linear motion system in use.

2.2.3 Take up section

This section manufactured specimens by the filament winding process using different molds, fiber orientations, and take up speeds. Figure 2.6 represents a schematic

drawing of the section. A 3/4” diameter stainless steel bar supports all molds and connects to the table by two frictionless Browning bearings.

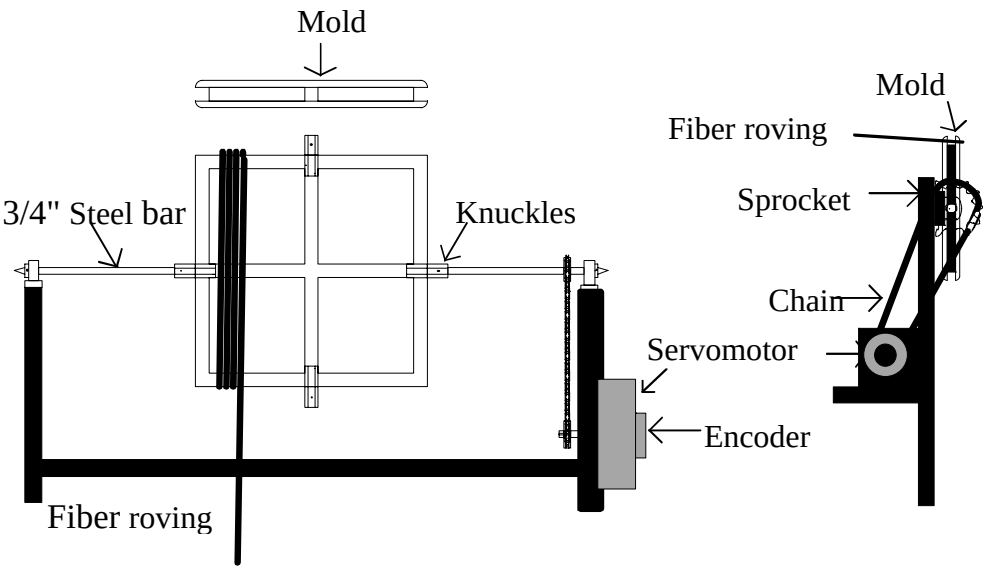

Figure 2.6 Top and side view of the take up section.

A chain and chain sprocket were attached to the bar transferring power from a second servomotor located below on the table. The 3/4” steel bar has a tapered point over the last 2 inches to easily pierce an already woven fiber layer. The bar serves as the axis for orthogonal layers to be woven. Torque transfer to the mold is accomplished by 8 cm long hexagon shaped knuckled collars machined to fit between the mold’s top and bottom interior surfaces. The knuckles are inserted into the mold where the guide slots have been widened 4 cm. An alan screw secures the knuckles to the bar. The servomotor has a 15 tooth sprocket attached to its axis while the steel bar has a 21 tooth sprocket resulting in a 1:1.5 ratio. This allows a varied range of mold rotational speed.

2.3 Mold types

There were several molds used with the same basic setup. All the molds were made of Plexiglas sheets glued together with acidic acid. A universal mold capable of making 0°, 90°, and 45° plies is shown in figure 2.7.

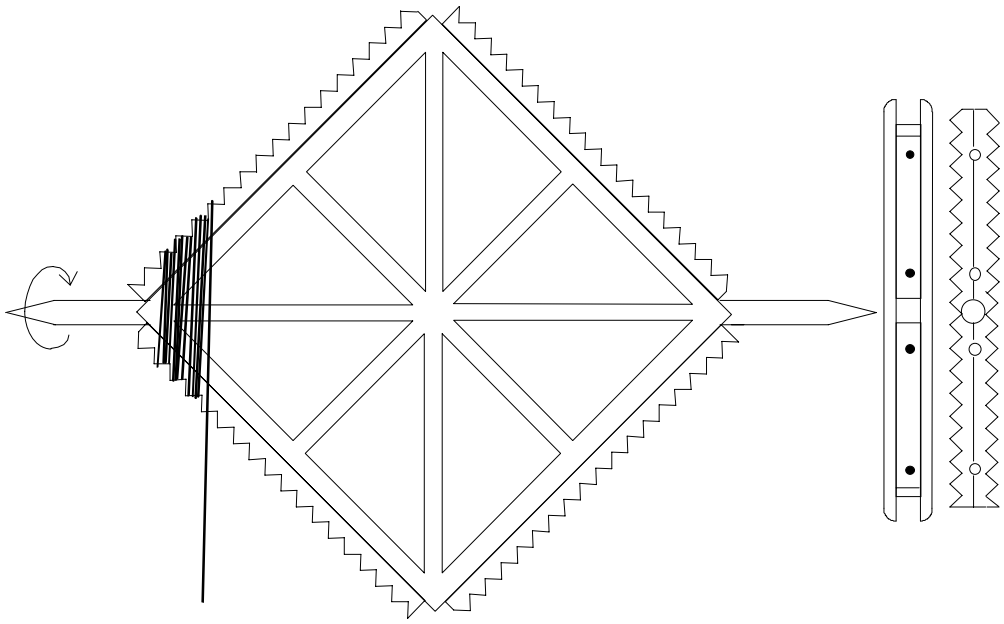

Figure 2.7 The mold used to make multiple ply orientation composites.

Early uniaxial samples were made from a mold with dimensions of 18” X 13” X 1.75”. A lengthwise notch and fillet along the 18” direction allowed for easy removal of the specimen after curing. The 0/90/0, 0/90/90/0, and 90/0/90 samples were made from a 16” X 16” X 1.75” mold. This was made with two pieces of 16” X 16”X 3/8” Plexiglas glued to 4 6.5”X 6.5” X 1” blocks. The blocks were spaced 3/4” ± 0.005” apart to accommodate for the two rotational axis 90 degrees apart. All four edges were filleted and the 1” blocks were left short of the filleted edge for cutting purposes. This easily accommodated an angle grinder blade to cut the specimen after curing. This same design

was used to build a mold for making layers of 0°, 90°, and ±45°. Extra 3/4" ± 0.005" accessways made along the mold diagonals gave the ability to make ±45° layers. Another way of constructing these samples was to attach 4 1.5" X 1.5" X 1/8" steel angle irons in the open ends of the mold. The angle irons were machined in 90° sawtooth shapes that prevented the fibers from slipping down the mold edge.

Other molds and/or setups were constructed. A mold for hollow cylindrical samples was made of a four inch diameter PVC pipe with steel collars. This mold was used to make samples of pipes that could be tested by hydraulic pressure applied within the pipe. Also, a compression set up exists for the wrapping of existing cylinders with the fiber roving. This would increase confinement of the sample cylinder and therefore increase the compression capacity.

2.4 Servo Control System

The reason for using a servo control system is to achieve accuracy and repeatability in the automated production of a composite. A servo system is a closed loop system that measures output variables, feeds them back to the controller for comparison to the desired input variables. The schematic representation of a closed loop system is illustrated in figure 2.8.

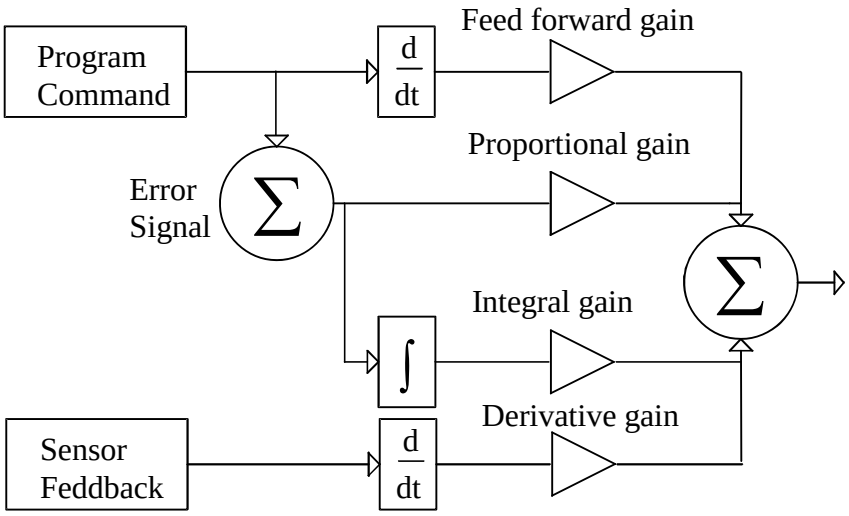

Figure 2.8 The closed loop system whose output is the command signal.

Any deviation from the desired input is defined as the error and is amplified and used to correct the error (15). In a servo system the motor is constantly acting to correct the difference between the actual and the desired parameters inputted. This makes the choice of feedback type, motor and drive characteristics, and proper servo tuning very important to overall system performance. System accuracy is determined by the encoder resolution. All servo systems must include an amplifier, an actuator (motor), and a feedback device (encoder). These devises are all bi-directional, meaning they can control motor speed and torque in both clockwise and counter clockwise directions or all four quadrants (15). Since a servo system is always adjusting its parameters it must be tuned to a state of stability otherwise changes in loading or friction will diminish proper functioning. If accurate components are chosen and tuned properly, a servo system can give the precision needed for automated manufacturing of composite materials.

2.5 Electrical support systems

2.5.1 Introduction

The main components of the electrical system for the servo filament winding setup are a 486 DX 33 MHz IBM compatible PC, a multi-axis servo controller, four servo amplifiers, a main power bus, a step-down transformer, and two DC gear reduced motors with incremental encoders. Two panel boxes are used to enclose some of the components.

Waterproof Sealtite cabling and connections protect all exterior wiring. This protects all the components from water damage and the user from other hazards especially electrical shock.

The computer controls the filament winding system through the Microsoft Windows compatible languages of Motion Architect and National Instruments LabView. LabView is an object oriented programming language that allows the creation of virtual instruments and their integration into a simulated control panel. All human interfaces to the filament winding system's motion control originate from the LabView control panel. The controller command language interpreter called Motion Architect then interprets the inputs. An extensive communication library containing several virtual instruments (VI's) called Motion Toolbox has been written specifically for the communication of LabView to Motion Architect. The VI's imitate and represent the behavior of actual instruments. This library allows easy access to build basic communication between the languages shortening programming time. All VI's used for the LabView filament winding controlling program Simplemotion3-4.vi were from this library.

2.5.2 Controller - AT6450

The AT6450 is a microprocessor-based four axis servo controller located in the 12” X 8” fuse box. The AT6450 and its wiring diagram are shown in Appendix A. It is designed for sophisticated multi-axis control of many servomotor/drive systems and is connected to the 486 IBM compatible PC computer via an open 16 bit expansion slot. The AT6450 receives the computer signals through the 50 pin connector to the main board. The AT6450 operating system is the 6000 Series Command Language that is downloaded to the AT6450 card during computer boot up. This language can be operated in either Microsoft Windows or DOS environments. Small lights on the AT6450 signal the status of the controller and the four axes. This indicates that the controller is prepared to download the command language. Other lights indicate the enabled or disabled status for each axis.

The controller is an integral part of this system. It is a processor-based controller, which, through output connections to the drives, determines all the parameters associated with motor performance. The controller has a built in microprocessor whose operating program is stored in ROM. The program interprets the command signals received from the PC based command language giving the desired position, velocity, and acceleration. The microprocessor uses this information to control the programmable pulse generator to produce the step and direction signals that control the servo drives. This controller possesses many inputs and outputs that have varied applications. Inputs can come from the human interface (computer), directional limit switches, auxiliary analog connections, or a joystick connection. All inputs and outputs can be interrogated or monitored before

action is taken. Outputs can initiate other functions or be used as indicators for program status. These functions are in the 4 triggering connections or the 4 auxiliary outputs connections. All connections are optically isolated

The AT6450 uses incremental encoder feedback to close the positioning loop and can control servo drives in both velocity and torque mode. It also has a fast Digital Signal Processor (DSP) that uses digital proportional, integral, and velocity feedback as well as acceleration and velocity feedforward for servo control. The capability to interrupt or stop program execution by human request or occurrence of error conditions exists. The AT6450 has several built in capabilities for end of travel limit switches in the clockwise and counter clockwise direction on all four axis. There is also the capability for auxiliary eight-bit ±10 V analog outputs through the AUX connection. Other capabilities exist for 4 trigger inputs, 48 general purpose inputs/outputs (24 each), 4 auxiliary outputs, joystick control of all axis, and 4 ±10 V, 14 bit analog inputs.

The AT6450 are wired by a color sequence for the encoders and drives connections. The controller receives feedback signals directly from the two encoders while supplying their 5V DC power for operation. The encoders translate the mechanical motion of the motors into electric signals for servo controller monitoring of the position and/or velocity of the system. The AT6450 drive wiring first connects to the servo amplifiers before being transmitted to the motors. The end of travel limits are wired directly from the AT6450 to the guidance linear position system using the LIM 1/2 connection. The switches are enabled during startup processes and guard against out-of-limit clockwise motion on one end and counter clockwise on the other.

The encoder and drive connections on the AT6450 board are wired with twelve-cable color-coded wire. The drive terminals require four separate connections each while the encoder terminals require eight wires each. One 12-cable wire was used for two drive terminals. Another 12-wire cable was used to connect to encoder terminals. All wiring passes through the waterproof cabling to the second fuse box where the drive cables are connected to the amplifiers. The encoder cabling passes through the second panel uninterrupted.

2.5.3 Amplifiers

The amplifier delivers the power to operate the motors after acquiring the low level commands from the controller via the wiring scheme shown in Appendix A. The KXA pulse-width modulated (PWM) servo amplifiers used here are designed for driving the DC servomotors and are contained in a 18” X 24” fuse box. Pulse-width modulation controls the mean current in a motors phase windings by varying the duty cycles of the transistor switches. This allows motor operation in both CW and CCW directions. The main AC power source must pass through an isolated step-down transformer before connection to the AC input terminals on the TB3 power module of the amplifier. The secondary AC voltage must be in the 19-37 V range. The amplifier converts this into the required input power of 16-48V DC. The DC motor supply power leaves via the #1 and #2 terminals on the TB2 module. Output capabilities are 8.0 amps continuous current with 16 amp peak current and 12-44V DC range depending on the input voltage magnitude. The amplifier is easily matched to the servo application through manipulation of the Adjustment Potentiometers (Pots). The Pots allow for maximization

of servo system behavior by adjustment of the command signal gain, the feed-forward response, the continuous and peak current limits, and adjustment of the offset motor speed to zero to match the zero command speed.

The amplifiers supply the needed 24V DC to power the servomotors. Electronic current limits protect the motor. Additionally, fault protection in these amplifiers guard against short circuits, power supply failure, excess temperature, and excess current. Dip switches set the mode of operation, the feedback type, the use of torque or velocity mode, and the use of an emf or tachometer. Torque mode was used in this study.

The drive wires connect to the TB1 mating connection terminal on the amplifier. The four drive wires connect to the Enable (terminal #6), IN-1 (terminal #4), and two GND's (terminals #2 & #5),. The Enable connection enables the amplifier for operation. The IN-1 terminal is the command input signal for controlling the amplifier while the GND's are signal grounds.

2.5.4 Transformer

The T-26-16 isolation and voltage reduction transformer supplies power to the two amplifiers. The transformer takes in a standard 115V AC supply that is run to a main switch located on the second fuse box face. This switch allows control of the power flow to the transformer's two input supplies. The transformer supplies 16 amps and 48V AC that splits out into the two terminal sets. The terminals are wired to a set of four switches also located on the face of the second fuse box. The switches allow for a manual on/off operation of a single axis or combination of axes in an emergency. The light indicates power or current being supplied to the amplifier and can indicate a power problem if

unlit. After power has passed through these switches it finally reaches the amplifiers. The amplifiers then supply the servomotors with 24V DC.

2.5.5 Servomotors

A 12FG Ferrite Servo Gearmotor was used for both the linear guidance and take up applications in the filament winding system. The servomotor is shown in figure 2.5. The amplifiers supply 24 V and a continuous 8 A current while the motor demands are 21.0 V and a continuous 6.9 A.

The motor has several useful features desired in servo motion control systems including constant torque over the entire velocity range, low inertia, zero cogging, low voltage operation, and full reversibility. Low inertia allows faster acceleration and more accurate response to command signals. Full reversibility means all characteristics of motor operations in one direction exist in the opposite direction. This allows the motor to be back driven and operated in both CW and CCW directions. Zero cogging keeps the motor running smoothly, especially at very low speeds, increasing the operational velocity range of the entire system. This also maintains motion control accuracy at a high level throughout the entire range.

The Ferrite servomotor is prepared for encoder attachment if desired. The encoder is the actual position indicator and its resolution determines the accuracy of the system. The position signal is compared to the desired position to get the error signal in the closed loop system. The resolution can be adjusted by software and here is set at 2000 counts/revolution.

The motor is geared down by an 80:1 ratio giving a 160,000 counts/revolution encoder resolution. This gear ratio also results in a continuous output torque of 17.5 N-m at a rated speed of 36 rpm. The continuous output torque is essential in the systems ability to keep a constant tension on the fiber roving while being wound into place on the selected mold.

2.6 Computer languages

2.6.1 Motion Architect

Motion Architect is a software development tool that allows the creation of set-up code and custom test panels, as well as the editing and execution of motion control programs. Motion Architect has four main modules that allow simplified access to its internal hierarchical system. The System Configuration module takes set-up information for your specific controller so that a motion program may be executed. Information such as the enabling/disabling of the limits, scaling factors, default values for acceleration/deceleration when limits are encountered, participating axis, and encoder mode are relayed setting up the controller for motion commands. The Program Editor module is used for writing or editing Motion Architect code. The Terminal Emulator module allows direct interaction with the AT6450 and therefore the linear motion system. Finally the Test Panel module simulates the motion programs with debugging and flow check capabilities. This increases system safety from possible damage due to unforeseen coding problems with the inputted motion commands. Once a program is written and saved in the Program Editor it can be called up and transferred by the Terminal Emulator to the controller and executed. The Editor was used to create the “startup.pgm” program

that initializes the values of the system before first use and the “clear.pgm” program that is used to restart the system when problems occur. They are called up by the Terminal Emulator and executed by the AT6450. More complex programs can be written with Motion Architect but it is much simpler and quicker to code in LabView.

Added to this configuration is the Servo Tuning capability under the Utilities module. The servo tuner allows access to the Proportional, Integral, Velocity and Feedforward (PIVF) gains in the closed loop system which determines system response to the given inputs of acceleration, velocity, and distance. The term 'closed loop' indicates that the system response is based not only on the command signal but the feedback of how the system is responding to the command signal as well. The feedback signal emanates from the encoders located on the back of both servomotors returning to the controller for comparison to the inputted value. This module allows the direct and graphical monitoring and adjustment of the gains (tuning values) to achieve optimal servomotor performance and system stability. This utility allows the velocity drive system to be tuned while the position loop is disabled. The position loop or controller can then be tuned to observe the accuracy of the system’s motion. The graphical display shows the commanded parameter and the actual system response to meet while allowing for direct monitoring of the gain adjustments. These tuning values are used in LabView motion program Simplemotion3-4.vi as part of the system initialization.

In this project the Terminal Emulator module is used to prepare the system for use and to control motion upon system breakdown or problems. In the Terminal Emulator module abbreviated versions of commands are used with the command fields for the motors following. Each command field is for a separate motor. The first two fields are

for two servomotors that are not used in this project. The take-up section servomotor is located in the third field and the guide servomotor is located in the fourth field. An example of the use of the Terminal Emulator module is the GO command that can initiate motion on a specified axis.

>GO0,0,1,1(enter)

This signal would initiate motion on the third and fourth axis while leaving axis one and two motionless. There are several commands that can be used to build and debug motion programs, configure and tune the servo system, and show the status of the system parameters in the Terminal Emulator module.

The ‘”startup.pgm”' program sends the gain values that optimize the system (for SGI, SGV, SGP) as well as the initial values for the velocity, distance, and acceleration of all the motors to the controller. This program is called up by the Terminal Emulator module and transferred to the AT6450 to initialize the system for movement under Motion Architect control. The “clear.pgm” is then down-loaded as the second part of system initialization but is not executed. To execute this program the letters ‘cl’ followed by a return must be entered into the Terminal Emulator making it similar to a batch file. The ‘cl’ enables the drives as well as re-establishes the current position to zero (0) (TPE0,0,0,0) and the position error to zero (0) (TPER0,0,0,0) for all four axis. The hard limits are also enabled (LH3,3,3,3). If a fault or limit occurred or motion had to be halted the clear program was used to re-enable the drives/axis and clear any existing error

condition. The program was used in case of problems with the ‘Simplemotionfor 3-4.vi’ during its use.

2.6.2 LabView

LabView is a graphical or object oriented programming language that allows the construction of an simulated instrument to suit many application needs. In LabView Virtual Instruments (VI’s) are built which can control instruments, acquire and analyze data, and present all of these in several forms. The VI’s are similar to subroutines in text based languages and can therefore be used in a hierarchical sense. Within one VI may be many more VI’s, now referred to as subVI’s, being called upon to support the purpose of the main VI. The VI is a structure with three main parts, a front panel, a block diagram, and the icon/connections.

LabView’s front panel acts as an interface between the user and the instrument being controlled emulating a control panel of a machine. The front panel consists of a combination of controls and indicators that allow the manipulation of the physical instrument. The controls imitate real input devices and supply the input to the instrument. Indicators provide convenient output formats for user observation. The data is input by a keyboard or mouse to the front panel. The behavior of the system can be adjusted during operation by front panel controls if needed with the output showing the manifestation of the adjustments.

The block diagram is a logical sequence of procedures that is the graphical source code of the VI. The diagram consists of objects that perform functions, send or receive data, and control the flow of execution. These blocks may perform a variety of functions

including mathematical manipulations, comparisons, conversions, input/output to other systems, or advanced analysis of incoming data. The blocks may be built-in function from one of Lab View's libraries like an addition function or a user built VI that performs a custom operation. The entire diagram may be broken down into three categories of basic elements - nodes, terminals, and wires.

Programming elements and structures are called nodes and are the pictorial representations of text-based language's functions, operators, statements, and subroutines. The nodes have source, sink, or special terminals to accept or send data. The terminals can be thought of as ports for input and output to the nodes. The nodes may be case statements, for next loops, an addition function or a VI. The structures that are nodes graphically surround the icons that they control. The case statement has special terminals that are affixed to its outside edge by the user. Any data that needs to be sent to the case statement will be sent to the terminals. Output control is performed in the same manner. A control or indicator on the front panel has its value represented by a different terminal on the block diagram. The control or indicator terminal has a rectangular shape which has the data type written on its' face and is always a source of data. The control or indicator terminal cannot be erased unless the control or indicator is deleted from the front panel.

The blocks pass data between the terminals along wires that are drawn with a special wiring tool. The wires have different colors that represent their type of data. For instance an integer is a blue wire, a real is orange, a character is pink, and a Boolean is green. Many of the problems in text-based languages are avoided by this wiring technique. For example, LabView eliminates some conversions by always matching up

the type. Also, a source terminal can only be linked to a sink terminal. Neither can be wired to the same type. This eliminates possible errors for the programmer.

Program execution is controlled by data flow in LabView. A node activates only when all the sink data has been received. It then executes its function and outputs the data to its source terminals. The data can then move on to its next sink terminal. LabView has a debugging tool that allows the user to visually observe this flow and execution order to see where problems may be occurring. This is different from most languages that execute on the basis of the order of the written code. This makes control of flow instruction driven while in LabView it is data driven.

The icon is a symbolic representation of the VI when it is being used as a subVI. As stated before, a VI is similar to a subroutine and here is used just like one. The data comes in through its source terminals and goes out its sink terminals after it has performed its function. The icon is used for communication to and from the subVI within the block diagram. The terminals correspond to the indicators and controls of the VI that make up the connector. The connector is the icon surface that shows all the terminals and their color-coded type. LabView offers the option to either show the icon or show the connector as seen below in the figure 2.8. This makes it easier to wire the diagram correctly while programming. The icon's look or representation can be a reminder to the programmer of what the VI is capable of performing. This allows for a better understanding of the data flow through the program.

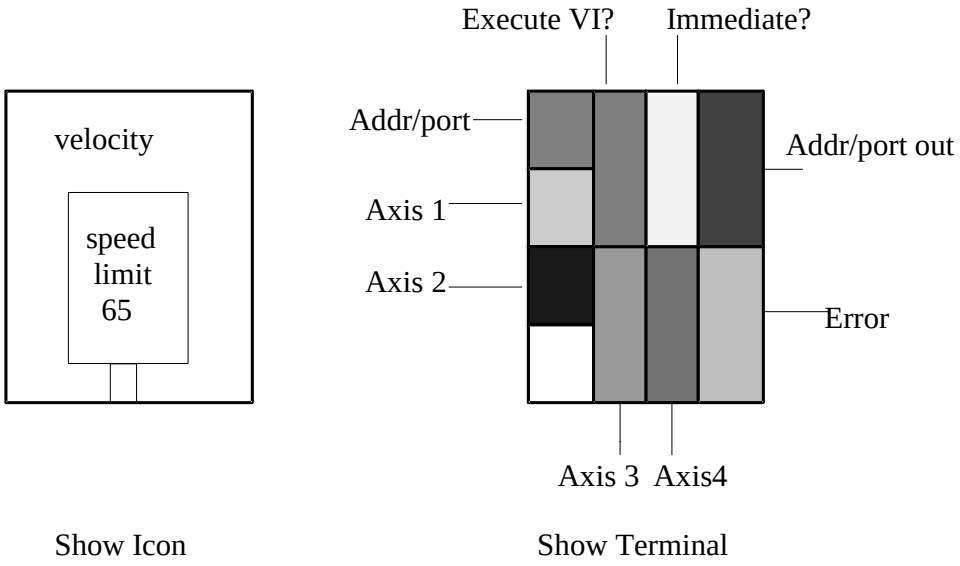

Figure 2.8 The Velocity icon representations in LabView

2.7 Fiber Properties

There are several types of fibers available that have a wide variety of properties and applications. The overriding factors in choosing a fiber is the application and the cost. Many fibers have attractive properties but are very expensive. Since the fibers are for tensile reinforcement all applications demand a high tensile strength. The other major properties are the modulus of elasticity (E), strain failure percentage, and bonding strength. Cement matrix to fiber stress transfer is more efficient with a high ratio of the fiber modulus of elasticity/cement modulus of elasticity. Higher strain failure percentages will give the matrix more ductility especially in the post-peak load region (4).

The fibers used in this study were in the form of spools containing a single roving containing numerous single fibers. The AR glass and polypropylene rovings are pictured in figure 2.10. A glass strand is bent over and spread out showing the approximately 204

fibers in the one of the 30 single strands in each roving. The polypropylene fibrillations can also be seen.

The AR glass fibers used have a Young's modulus of 70 GPa and a single fiber tensile strength of 3600 MPa with a 2% strain at failure. The fiber strand tensile strength was 1450-1900 MPa. The coefficient of thermal expansion is about one half that of

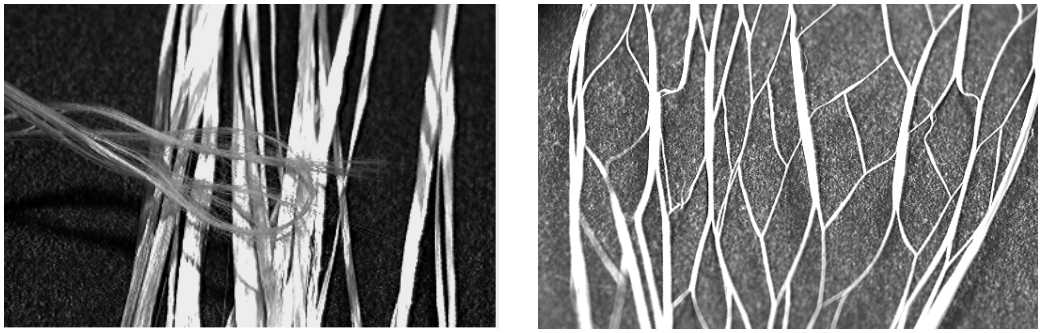

Figure 2.10 The rovings of AR glass and polypropylene.

hardened cement paste. The fibers are prone to alkaline attack when subjected to prolonged exposure to calcium hydroxide. The use of microsilica (silica fume) was used as a pozzalon to combine with the $Ca(OH)_2$ and other cement matrix alkalines reducing the chance of alkaline attack (7). For this purpose, a dose of 10 % silica fume was used.

Polypropylene fibers have a Young's modulus of 8.5-12.5 MPa with an ultimate tensile strength of 340-500 MPa. Fiber diameter was 35-250 μm (16). Polypropylene fibers increased the toughness with their post-crack bridging and high straining capabilities. The fiber's strength is not mobilized until they have been sufficiently elongated (17). Polypropylene fibers have no chemical affinity for the cement paste and depend mainly on the fiber surface texture for mechanical bonding. Most of this bond is mechanical anchoring and interlocking along with some interfacial adhesion (4).

There are characteristic parameters of the fibers that affect the behavior of the composite material. The aspect ratio is the ratio of the fiber length to its equivalent diameter. This aspect ratio will be extremely high due to the use of continuous fibers. The critical length of embedment (lc) is another factor that describes fiber behavior when excessive stress is being carried by the composite. At the critical length the fiber will tear and fracture rather than debond and pull out (18). Use of fibers with a high aspect ratio will lead to a higher load carrying capacity in flexure, shear, and torsion resulting in more efficient material use. Due to the continuous fiber lengths used there will be no fiber pullout in the conventional sense.

The fiber volume fraction is the volume of fibers compared to the total volume of the mix. Percentages range from near zero to 2% for low volume and up to 15% for high volume mixes. In general, the percent volume and bonding characteristics are most influential on the mechanical response of the composite (17).

The spacing factor parameter depends on the fiber dimensions, amount of impregnation, and the percent of fibers used. The closer the fibers are spaced the higher the first crack strength and more uniform spreading of the cracking after first crack initiation (19).

2.8 Cement matrix

The mix proportion used for the matrix phase in this study is given below in table 2.1. This mix is used throughout the entire study. The water/cement ratio used was 0.35. Set retarders were used to prolong the workability of the mix. Superplastizer was also

used to enhance the mobility of silica fume to within in the cement matrix and increase roving impregnation.

Table 2.1 Cement Paste Mix

Material	Weight (g)
Portland cement Type I/II	4713.8
Water	1814.8
Silica fume	471.4
Superplasticizer	25 ml
Retarder	4 ml

Table 2.1 Cement paste bath mix used for the composite construction.

CHAPTER 3

Manufacturing Procedures and Specimen Preparation

3.1 Computer Program development

The AT6450 controller board communicates with the 6000 series Motion Architect language. Once basic communication between the user and the controller was established using Motion Architect, the LabView programming could begin to be coded to ultimately control the system. To accomplish this task a library containing special tools of communication easily between Motion Architect and LabView was used.

3.1.1 LabView

The LabView program used for constructing the composite samples was Simplemotion3-4.vi. The control panel for this VI is pictured below in figure 3.1.

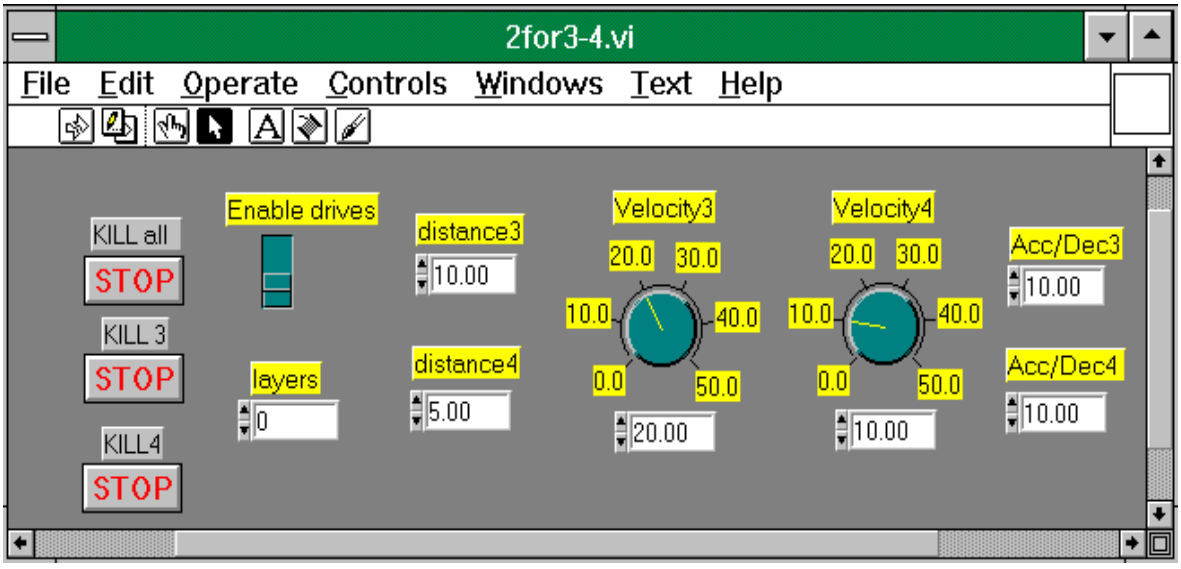

Figure 3.1 The front panel of Simplemotion3-4.vi.

The front panel serves as the interface to the user while emulating the looks of a control panel of a typical machine.

LabView's front panel allows the manipulation of a physical instrument by the inputs and the observation of outputs. The front panel controls are used to control the system and can be adjusted at any time with a mouse or keyboard, even while the VI is running. The adjustments can be noticed immediately in the systems behavior and in the panel's outputs. The desired distance of travel, velocity, and acceleration/deceleration are input by the operator in the front panel of the figure shown. The KILL switch is used to stop motion on one or all axis for safety or adjustment reasons. The Enable Drives switch re-enables the motors and drives after the KILL switch has been used.

The front panel in figure 3.1 shows the distances (d3, d4), velocities (Vel3, Vel4), and accelerations (Acc3, Acc4) as inputs through numeric controls for both servomotors. The deceleration rate is the same as the acceleration value.

The inputs are determined by the desired sample dimensions, i.e., width of a sample, ply thickness, and/or overall piece thickness. The d4 value determines the width of the sample and doesn't influence thickness. This input was calibrated to represent width in inches. The thickness of the individual layers and therefore the overall piece depend on the next inputs Vel3 and Vel4. The faster the guidance system (Vel4) moves the thinner the layer given a constant take-up speed or mold rotation (Vel3). Conversely if the guidance system speed is held constant the thickness of a layer increases with increased take-up speed. To simplify and establish a standard the Vel3 is set at 20. The input has been converted to be the number of revolutions per minute. Usually the guide speed (Vel4) would be set at one half of this value giving a fiber layer that has no gaps

between adjacent fiber rovings on the mold. For example if a 0/90/90/0 sample is being made the guide speed can simply be cut in half for the 90 degree pass and accomplish the desired thickness in one pass. The distance of the take-up motor is determined by the ratio of the velocities multiplied by the guidance distance d3 = d4 * Vel3 / Vel4.

The numeric control for the layers signifies the number of passes the guidance system will execute to make the composite. For example, a uniaxial piece of X thickness can be made in one slow pass of the guidance system. Therefore a value of 1 would be entered. Alternatively, it may be desired to construct the same X sized sample in two or three passes but the composite will still consist of only one direction of fibers.

The Enable drives switch is a Boolean control with a defaulted of false. It is switched on when vel3 & vel4 have been entered. The three kill buttons are also Boolean controls and are used to stop motion during the program execution. The block diagram for this program involves two screens because of the use of a sequence statement. The first block diagram is shown in figure 3.2.

Program hierarchy requires four configuration type VI's to be executed first. These VI’s establish how motion will be executed and axis encoder resolution for the third and fourth axis. Following this the motors are energized. The Enable Hard Limits VI's then enable the hard wired limits for the third and fourth axis. This protects the system from damaging the linear motion system by any possible input placement error. The rest of the sequences pictured are string commands

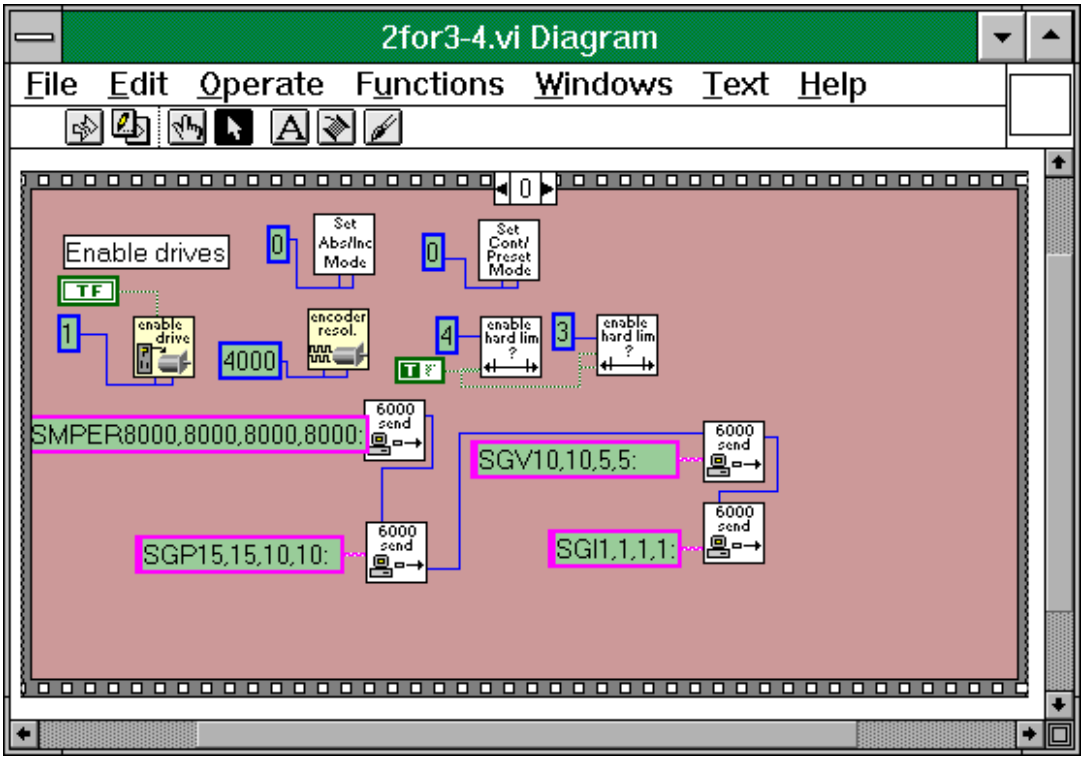

Figure 3.2 The wiring diagram for the first sequence of the control panel.

sending the gains to the AT6450 by using the Send 6000 Block vi. This screen was the initialization procedure, preparing the system to receive input and execute it. The second sequence contains all the motion VI's and inputted numeric controls within a ‘for’ loop. This block diagram is shown in figure 3.3. The inside of the loop is wired so that the VI's execute in a certain order. This is the blue wire coming in from the top left address port and leaving the top right address port for each motion VI. The inputs from the numeric controls have the same label as their counterparts on the control panel and, with the exception of the distance inputs, are wired into their VI's directly. The distance d4 is multiplied by the 1.6 million encoder counts per inch to convert the linear guide system to inches. To finish at the same time the take-up motor is also multiplied by 1.6 million. The formula node gives alternating signs for the

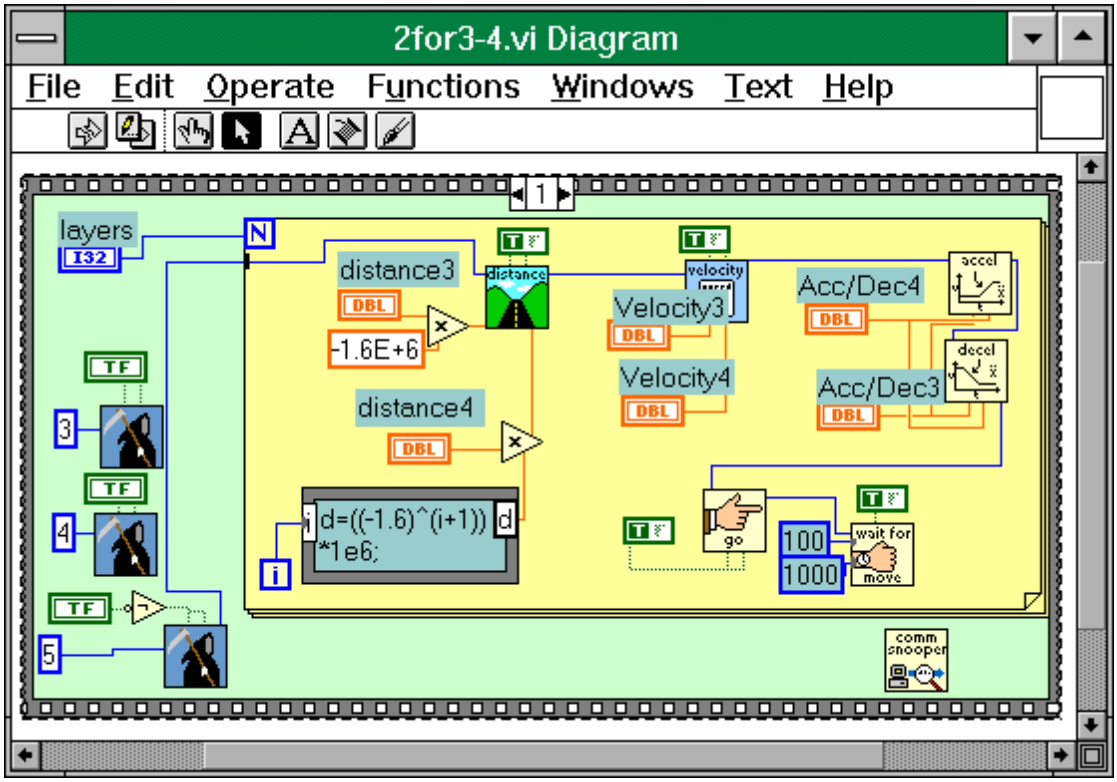

Figure 3.3 Wiring diagram for the second sequence of the control panel.

guide distance so it can change direction after completing one complete pass. The parameter I equals zero for the first loop execution therefore the guide moves toward the motor in a counter-clockwise fashion. This procedure works for uniaxial pieces. The cross ply composites require the sign to be changed for d4 on the control panel. Re-alignment of the roving with the guidance carriage was too time consuming after mold axis was changed. It was easier to stop the program, move the carriage, and then resume under the same original inputs

By following the blue wire for execution sequence, the velocity, acceleration, and deceleration values are sent to the proper VI's and then executed. The system then receives the go command form that VI which executes the motion according to the

inputs. The Wait For Next Move VI then holds all commands until both servomotors finish the inputted command distances and come to rest. This acts to keep the timing of the system from getting out of control.

The ‘layers’ numeric control on the front control panel determines the number of loop executions. Most of the time the 0/90/90/0 or other cross ply's entered execution number was equal to 1. This is because the mold axis was changed and this took varied amounts of time. An option was to add sequence screens with the different inputs and a Stop Motion VI between them. This proved to be more complicated than just changing the d4 distance for the guidance system to negative and starting the program again after re-alignment of the mold axis.

3.2 Set up procedure for manufacturing

The matrix mix proportions were weighed out and mixed according to the desired w/c ratio and silica fume content. The silica fume and water were blended in a food processor for improved dispersion. The water, portland cement (type I-II), and silica fume/water slurry are then mixed together in the Hobart mixer. A nominal amount of superplasticizer was added to lower the w/c ratio and increase workability. In addition, 4 ml of retarder was added to allow more working time.

Clean water was placed in the wetting tank as well as dry clothes in the drain bin to soak up the extra water. The desired sample composite determined the mold selected and the software sequence. The chain sprocket, knuckles, and Plexiglas mold were then attached to the axis bar. The chain sprocket was placed on the bar’s left end.

The power to the electrical system was turned on and the computer downloaded the AT6450 operating system. The power to the amplifiers was then turned on. The controlling software programs opened the Motion Architect Terminal and the control panel to the LabView program. The “startup.pgm” and “clear.pgm” were downloaded from the Editor through the Transfers toolbar and pulling down the Send Motion Program selection. This initialized the Motion Architect system and enabled the servomotors. At this point Motion Architect and LabView were functional to execute input commands.

The controlling servomotor was run a minimal distance aligning the chain sprockets. The bar sprocket was then tightened down with two alan screws. The Plexiglas mold with inserted knuckles was then positioned to maximize sample size and secured to the 3/4” axis bar. The Plexiglas mold was covered with a clear plastic wrap and the fiber roving was hand run through the system and tied down to the mold. The motors were then run to warm them up and make sure there were no stability or vibration problems. The guide system platform was moved to align the fiber roving with the desired Plexiglas mold starting position. Finally, the feed tube was tied to the drain bin and guide posts and then filled with cement paste.

3.3 Sample preparation

The control panel input values were for the distance, velocity and acceleration of the servomotors. The encoder resolution was 2,000 counts/revolution and with a gear reduction ratio of 80:1 there was 160,000 encoder counts/revolution. The drive screw was 10 threads/inch resulting in 1,600,000 counts/inch. System accuracy depended on the servo tuning performance. Once the sample size was known the total number of

encoder counts was determined and inputted as distance 4 (d4). The second servomotor distance (d3) was usually determined by the desired layer thickness. A multiple of d4, usually between 2 and 3, was chosen to find d3, v3, and v4. A thicker layer was obtained by using higher multipliers resulting in more mold revolutions over the same guidance distance.

The uniaxial sample, pictured in figure 3.4, was constructed without program

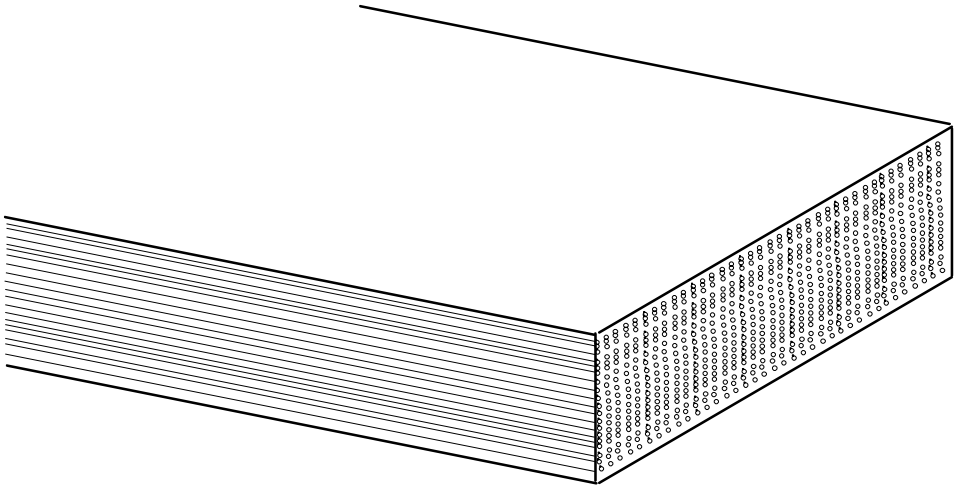

Figure 3.4 A view of the fiber orientation of a uniaxial sample.

interruption requiring the least amount of effort. The number of fiber orientations in a composite sample determined the “layers” input on the control panel. Cross ply laminate production required a program interruption to rotate the mold. The bearings, chain

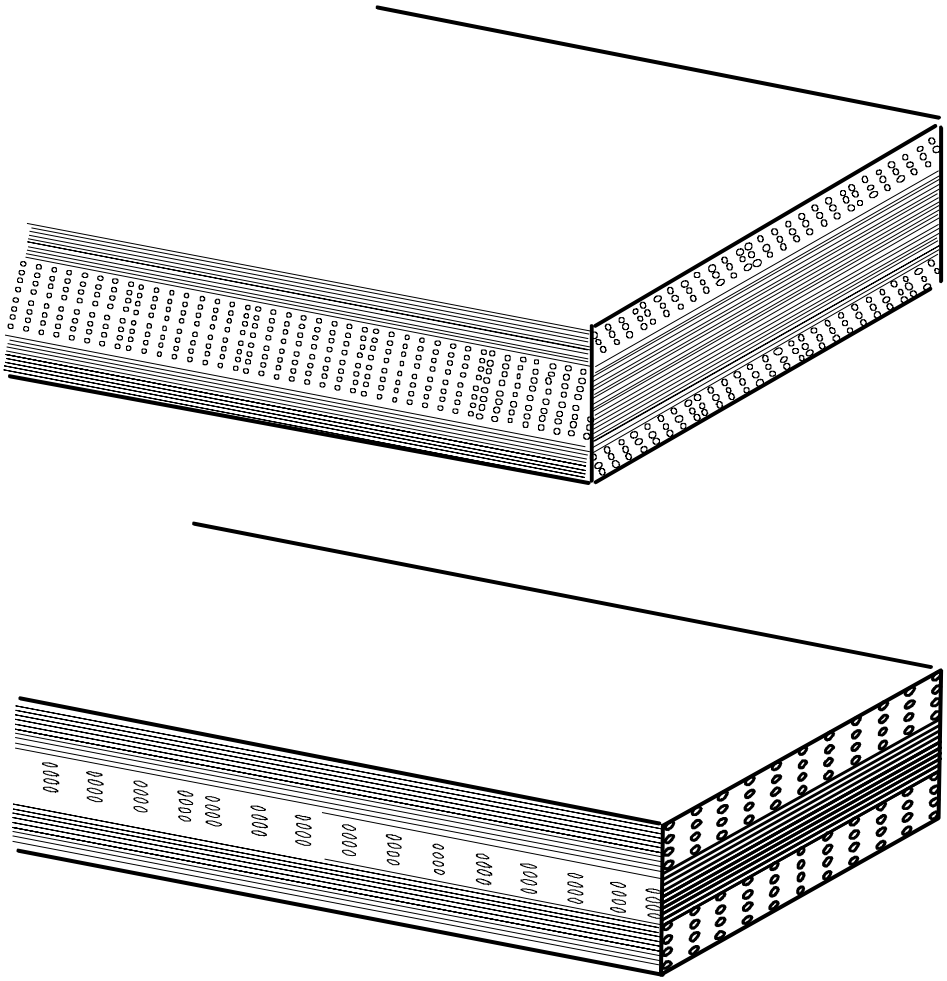

Figure 3.5 The fiber orientations in $(0/90)_s$ (top) and a 0/90/0 composites.

sprocket, and knuckles were loosened and the bar extracted and inserted to the new orientation. The knuckles, chain sprocket, and the bearings were then refitted. Guidance system input d4's sign was reversed allowing travel opposite to the previous direction. The same procedure was followed for all fiber direction changes.

Following production the mold and sample were removed, wrapped in clear plastic and placed under hydraulic ram pressure of 35 kPa for two hours. This removed excess water, increased fiber roving impregnation, and stabilized dimensional quality reducing the surface grinding required for specimen preparation. The sample was then

removed and placed in a steam curing room for 24 hours. An angle grinder fit with a diamond blade cut and removed the sample from the mold. The sample then placed in a calcium hydroxide water bath for at least 28 days.

3.4 Calculation of V_f

The fiber volume calculation was performed before the sample was cut into the specimens with the formula

$V_{fiber} = A_{fiber} / A_{composite}$

where

$A_{fiber} = N * \pi * r^2 * \eta_1 * \eta_2$

with

N = the total number of windings or mold revolutions in constructing the sample. (400)

r = the average radius of the single glass fiber. (12 μm)

η_1 = the number of fiber bundles in the roving. (30)

η_2 = the number of single strands in a bundle. (204)

and

$A_{composite} = \int_0^l z*dx = [z_i * w_i]*l$

where

z_i = the specimen thickness at the given point. The measurement points were spaced out at 1/2 inch intervals across the sample surface in both the x and y directions.

w_i = the weight given to the point, here all equal to one. Cross-sectional composite area was the average material thickness multiplied by the sample length.

$A_{fiber} = 400 * \pi * 12\ \mu m^2 * 30 * 204 = 1.10745\ e\ (-3)\ m^2$

$A_{composite} = 2.468\ e\ (-2)\ m^2$

$V_{fiber} = 0.04487 \approx 4.5\%$

3.5 Specimen preparation

Individual 3 inch by 12 inch test specimens were cut from the sample by a water-cooled diamond blade tile saw. Rotating the cutting surface 90° cut the 0/90/90/0 and 90/0/0/90 specimens from the same samples. Due to notch sensitivity of the brittle matrix material, a Do-All bench grinder removed any warping, dimensional discrepancies, and scratches from the specimen surface. The early specimens were not ram pressed and needed excessive grinding. Ram pressing reduced grinding time significantly. Even plastic wrap creases could serve as initial crack sites causing premature cracking affecting the modulus of elasticity measurement.

Tensile specimens were then cut into a dogbone shape as shown in figure 3.6.

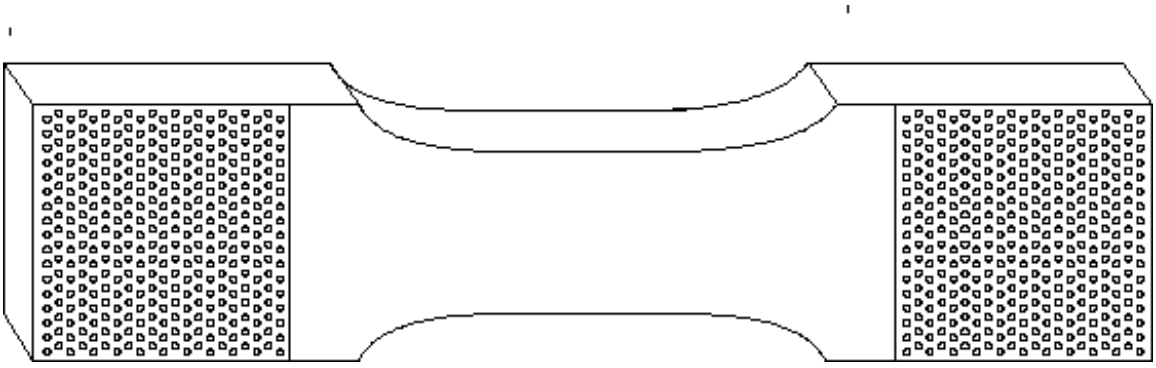

Figure 3.6 The tensile specimen cut into a dogbone shape.

A carbide bit router cut around the dogbone shaped steel template clamped to the specimen. Following this all specimens were dried for 24 hours. Perforated 1/16 inch

thick steel plates were epoxied to the top and bottom gripping surfaces. The plates were pressed allowing the epoxy to enter the perforations. For grip slippage to occur the epoxy/steel bond and the epoxy in the perforations would have to be sheared. The plates served as a more durable and less brittle medium for load transference from the grips to the specimen. Two ton and Five minute epoxy was used.

CHAPTER 4

Mechanical properties of composites

4.1 Experimental scope

Tension and flexural tests were performed at the Arizona State University Structures Laboratory using a closed loop servo hydraulic controlled MTS 810 material test system with a 225 kN load capacity. Test Star software controlled the closed loop testing with linear variable differential transducers (LVDT) being utilized as the feedback signals. A 12-bit resolution data acquisition system was used. Fracture surfaces, morphologies, microcracking and macrocracking were studied by vacuum epoxy-dyed impregnation of tested samples. A fiber volume fraction of 4.5% for AR glass and 7% for polypropylene specimens was used.

4.1.1 Tension testing

Closed-loop uniaxial tension tests were performed on 32 samples: 27 AR glass and 5 polypropylene. Six specimens were not ram pressed. Instron's 500 kN hydraulic grips with serrated jaw-faces secured the specimens to the loading frame as pictured in figure 4.1. This grip system utilized wedge action to create fixed-end conditions and uniformly distributed displacement across the specimen width. Gripping pressure ranged from 1.4 -21 MPa.

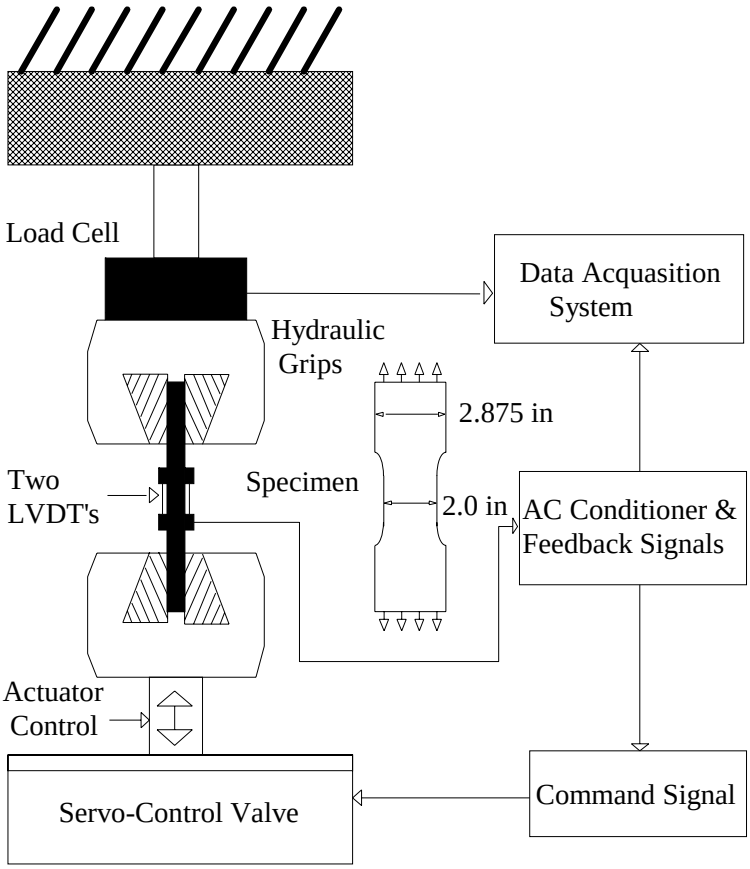

Figure 4.1 The schematic view of the tensile test apparatus.

Load transference occurs through the grip's serrated faces to the epoxied metal plates. A dogbone shaped specimen was chosen to limit grip system influenced failures.

Two LVDTs were placed on the specimen's opposing neck surfaces to reduce bending effects due to frame misalignment or single lamina failure. The averaged LVDT signals monitored the 90mm gage length elongation with a ±1.27 mm (±0.05 inch) range. The LVDTs rested on glued 1/16 inch thick steel edges yielding an exacting gage length.

A 3/8 inch rod aligned the mounts while rubber bands secured the LVDT placement system until glue drying. The data acquisition system recorded the stroke, load, LVDT, and time increments from the test start.

The testing procedure started under force control until an 88 kN preload was achieved. Following this LVDT controlled testing with strain rates of 0.0005 mm/second or 0.001 mm/second until LVDT range was exhausted. Testing then proceeded under a stroke controlled rate of 0.001 mm/sec until failure.

4.1.2 Flexure testing

Four-point flexure tests were performed on 18 AR glass samples. The test setup applies only vertical line loads to the specimen and is displayed in figure 4.2. Pin connections minimizing tortional forces by allowing rotation of one base support and the entire upper fixture Center point deflections are measured from a frame attached to the specimen above the base supports. The single spring loaded LVDT is located at the midspan of the undeflected points. This eliminates support settlement or seating problems (20).

Test procedure started under LVDT control with a 0.005 mm/second strain rate until the ±2.54 mm (±0.1 inch) range was exhausted. The test then proceeded under stroke control at a rate of 0.001 mm/second until specimen failure or other ending condition.

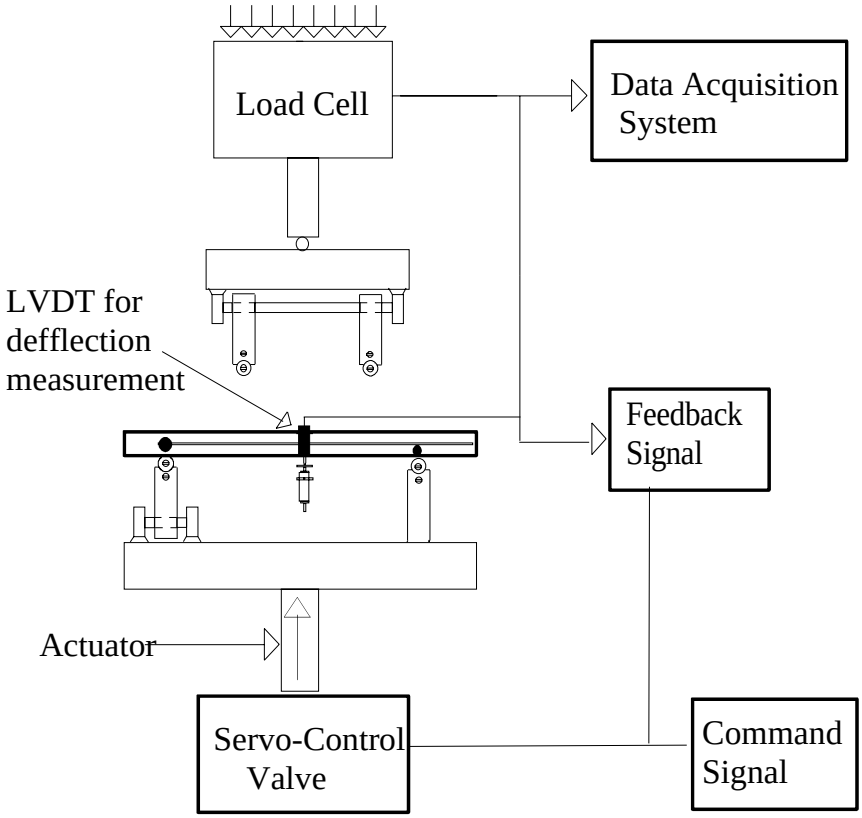

Figure 4.2 The schematic view of the flexure test apparatus.

4.2 Specimen tension test response

4.2.1 Overall characteristics of tensile testing cement composites

Past fiber reinforced cements (FRC) with randomly dispersed short fibers and low volume fraction displayed increased toughness until first crack formation. The matrix did not significantly contribute to the composite strength past this point. Higher short fiber volume fractions arrested and bridged microcracks transferring stress into the uncracked matrix increasing the toughness significantly (16). Once a certain fiber volume fraction for a mixture was exceeded the FRC ultimate strength and ultimate strain increased considerably (5). However, this led to difficulties in mixing and porosity.

Modulus of elasticity of cement composites increase little by adding fibers due to the low volume fraction mixing allows and the relatively similar fiber/cement modulus values. Using the Rule of Mixtures, a 15% glass fiber volume fraction (E_{glass} = 75 GPa, E_{cement} = 20 GPa and efficiency factors of fiber length and orientation to applied load = 1) the projected composite modulus would be 32.5 GPa. Assuming homogeneous behavior, this is a minor increase for a tensile structural material. However, fibers do dramatically increase the tensile strength, strain, toughness, and impact resistance past plain matrix levels.

These findings initiated use of spray-dewatered glass fiber reinforced cement (GFRC) panels with 5% randomly distributed short fibers. GFRC's mechanical properties will be compared to the results found here given the similar fiber volume fraction. It has also been shown that pultruded FRC has the highest tensile and pseudo strain hardening response than other conventional or extruded FRC's (21). This allows more economical use of the expensive fibers.

4.2.2 Tensile testing-AR glass

Tensile testing of AR glass and polypropylene cement composites was investigated. Typical parameters determining material tensile response are the modulus of elasticity (E), first cracking stress and strain, bend over point (BOP or proportional limit), ultimate strength, pseudo-strain hardening, and the toughness. These parameters described the randomly distributed short fiber composites and are noticed here also.

The stress was the applied load divided by the specimen neck cross-sectional area. The averaged signal from two LVDT's and a 90 mm gage length gave the strain.

Composite orientations of uniaxial (0°), $(0/90)_s$, 0/90/0, and $(90/0)_s$ were tested in a similar manner. Tension test results are in table 4.1.

Table 4.1 Tensile Test Results

Lay up	#	E (GPa)	E_2 (GPa)	σ_{BOP} (MPa)	ε_{BOP} (mm/mm)	$\sigma_{ultimate}$ (MPa)	$\varepsilon_{ultimate}$ (mm/mm)
0 G	10	22.33	9.15	12.06	0.92E-3	45.22	8.2E-3
0/90/0 G	4	8.46	2.82	6.91	1.41E-3	21.81	12.5E-3
$(0/90)_s$ G	5	21.63	1.89	9.86	2.39E-3	38.27	18.4E-3
90/0/90 G	4	11.31	2.47	11.58	1.27E-3	34.29	14.1E-3
PP 0	5	22.50	0.22	7.80	0.90E-3	14.02	39.4E-3

G = AR glass PP = polypropylene

Table 4.1 The average results of the different composites tested in tension.

4.2.2.1 Initial response

The initial response of the composite was semi-linear. The composite modulus of elasticity (E_c) for uniaxial and $(0/90)_s$ specimens were close to values given by the Rule of Mixtures and by other models (22). A typical stress-strain curves for uniaxial and $(90/0)_s$ are shown in figure 4.3 and figure 4.4. Composite modulus of elasticity values for 0/90/0 and $(90/0)_s$ were lower than expected.

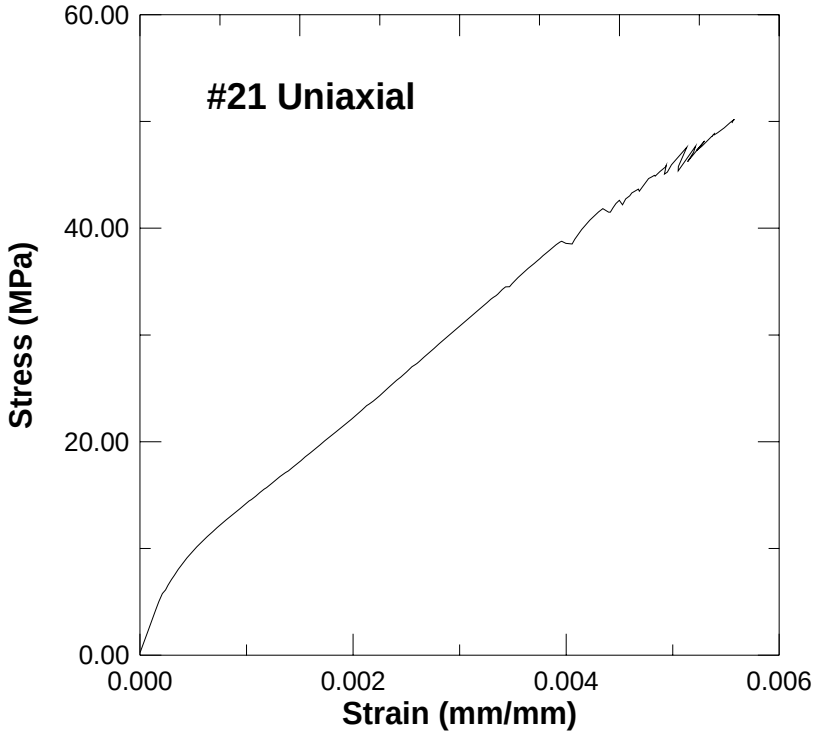

Figure 4.3 Stress-strain curve of a uniaxial specimen.

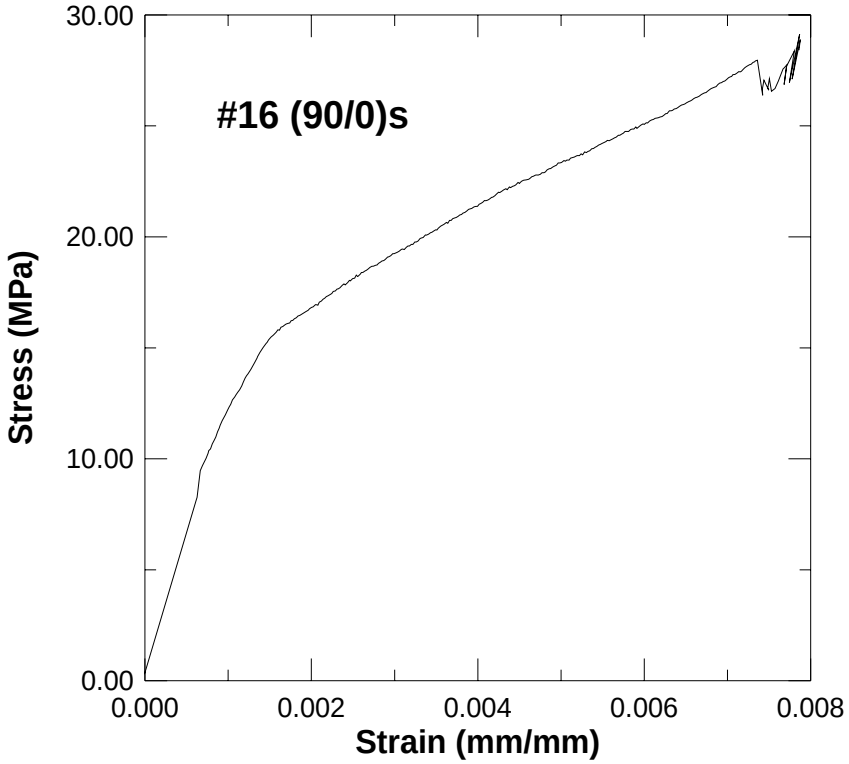

Figure 4.4 Stress-strain curve of a $(90/0)_s$ specimen.

Conventional short random fiber reinforced cements (SRFRC) sharp bend over point (BOP) was replaced by a smoother “knee” transition to the secondary linear response. SRFRC glass specimens exhibit this “knee” transition at higher fiber volume fraction than used here. The fibers delay the main crack localization by bridging the initial microcracking, giving a smoother BOP transition. The BOP transition starts by an isolated crack forming. The transition ends when the one single crack propagates across the entire specimen width (21). The glass fibers uniform placement in the matrix allowed more efficient microcrack arresting. Also, the load increased as the strain increased indicating further load transference to the matrix. Typical SRFRC behavior is for a constant load after first crack formation due to the fibers carrying the entire load over the increasing strain. The Aveston, Cooper, and Kelly model predicted this at a constant load at a large volume of strain (23).

4.2.2.2 Secondary response

Following the BOP transition stress increased linearly as pseudo-strain hardening took place until failure was reached. The secondary linearity (E_2) was modeled with a slope equal to $E_f V_f$ or 3.75 GPa (given E_f = 75 GPa and V_f = 5%). Fiber volume fraction determines secondary response with SRFRC, which generally follows the $E_f V_f$ value. The uniaxial samples here averaged of 9.15 GPa for E_2, more than twice the expected value. The other secondary stiffness results were 50 - 75 % of the expected value. However, orthogonal lamina has cracked at the elevated strain levels and isn’t carrying

any load. The E_2 values signify that the matrix is still carrying a portion of the applied load even with the high strain and cracking.

4.2.2.3 Comparison of composite types

The cross ply specimens exhibited increased strain capacities with reduced ultimate stresses when compared to the uniaxial specimens. Many cross ply composites had ultimate strains in the 1% - 2% range. Average ultimate strains increased 124% for $(0/90)_s$, 71% for 90/0/90, and 52% for $(90/0)_s$ composites when compared to the uniaxial samples. BOP strains also increased with $(0/90)_s$ composites being 260% larger than the uniaxial samples. The ultimate stresses were reduced due to fiber lamina orientation. Only the 0° plies were carrying the applied load at the higher strain levels. Cross ply stress values above 30 MPa with strains over 1% were common.

Stiffness values for 0/90/0 and $(90/0)_s$ composites were lower than the uniaxial and (0/90) specimens . However, the 0/90/0 specimens were manufactured before fiber/cement bonding was maximized therefore reducing the effective cross sectional area. $(90/0)_s$ composite testing experienced difficulty with only two of the four specimens giving worthwhile E_c data. Ultimate strengths in four uniaxial and one $(0/90)_s$ specimen exceeded 50 MPa, while two of these had ultimate strains over 1.2%. Testing apparatus was observed to influence failure mode perhaps leading to a lower representation of composite ultimate strength. Improvements in specimen processing and a better grip system would lead to more accurate test results.

4.2.2.4 $(\pm 45)_s$ composite response

The initial tensile test response is linear but well below the value range of plain cement (10-30 MPa). A ±30° off axis fiber alignment to the applied stress results in composite weakening and reduced microcracking, which was identified here (24).With the fibers at a 45° angle only half the stress is directed along the fiber axis. The other half becomes a debonding force and illustrated in figure 4.5.

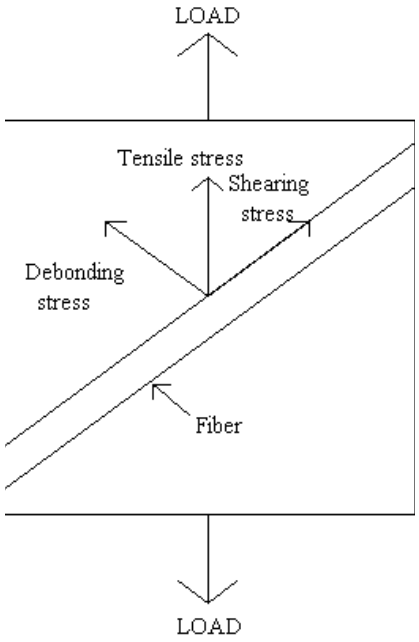

Figure 4.5 The development of debonding force with off axis fiber orientation.

The fiber roving was not completely impregnated during manufacturing and ram pressing was not performed. This left the composite cross section with several inherent weak areas and high w/c ratio resulting in low tensile strength. The mean ultimate strength was 5.6 MPa at 0.25% strain. This is 13% of the average uniaxial specimen ultimate strength.

A single major crack along the fiber's axis led to each layer's failure. Since no other cracking occurred, the secondary strength was the delamination resistance of this composite.

4.2.3 Tensile testing-polypropylene

Five uniaxial polypropylene specimens were tested. Modulus of elasticity values were in the plain concrete range as expected. Ultimate strains of 2.5% were easily obtained since no specimen ultimately failed. The stress and strain levels were still rising at every test termination with four specimens reaching the 11-12 MPa stress level. Specimen #5 was tested to an 8.5% strain with a 18MPa stress. Strain and stress were still increasing. Gripping pressure did not effect any test outcome. The specimen's visible cracking was both parallel and transverse to the fiber orientation. The microcracking spacing and distribution was so thorough it appeared as if a grid system had been drawn on the surface of the specimen. As the load increased the cracks began to separate.

The linear phase ended with a very distinct bend over point (BOP) as expected with the fiber's low E_p. The stress-strain curves followed the ACK model shape. Unlike the GFRC specimens, all polypropylene test responses were extremely similar here and to tests performed by Mobasher and Stang (25). The composite test response was semi-linear to the 8 MPa stress level. Hand pultruded composites by Krenchel and Stang (26) and later by Mobasher (23) had similar results showing that mechanized pultrusion can repeat previous results.

Past the BOP was a multiple cracking phase, signified by increasing strain at a constant stress. Initial secondary response roughness was due to stress release by significant cracking and the fibers need to be stretched before mobilizing strength to carry stress. The response soon smoothed out as expected. The secondary response depends on the fiber/matrix bonding and the interface properties. The fineness or closer microcrack spacing dictated the smoothness of this phase (12).

4.3 Specimen flexure test responses

Flexural testing of AR glass/cement specimens in four point bending was investigated. The flexural test is a preferred testing method for quality control and design specifications due to its simplicity and real life loading conditions. Twelve uniaxial specimens were tested, eight to conclusion. Six $(0/90)_s$ specimens were tested, five to conclusion.. Linear elastic behavior was assumed and used in calculating flexural properties.

The proportional elastic limit (PEL) is the point where the flexural stress-deflection curve deviates from linearity. The limit of proportionality (LOP) is where the flexural stress-deflection curve loses all linearity and proceeds into secondary stages of crack growth. The modulus of rupture (MOR) is the ultimate load carried by the specimen. Five specimens were not tested to failure and their properties are not included in the ultimate calculations. Flexure testing results are in table 4.2

Table 4.2 Flexure Test Results

Lay-up	#	E_c (MPa)	σ_{PEL} (MPa)	d_{PEL} (mm)	σ_{LOP} (MPa)	d_{LOP} (mm)	σ_{MOR} (MPa)	d_{MOR} (mm)
0	12	16.75	11.15	1.05	48.20	4.61	49.78	5.36
$(0/90)_s$	6	22.82	13.81	0.62	20.71	2.03	23.24	11.37

d = deflection

Table 4.2 Summarizing the flexure test results.

4.3.1 Flexural modulus of elasticity

The typical flexural stress-deflection curve is shown in figure 4.6. The flexural modulus of elasticity was in the range for random fiber glass/cement composites. Any fiber, matrix or fiber/matrix failure gives a non-linear response in the test. The large specimen thickness yields rapidly increasing stresses in the outermost tensile fiber. Shrinkage cracks could have existed lowering the initial response under the intensified stress. Mallick suggests a ratio of 60:1in flexural testing or else shear stresses can develop to a significant level. However, large deflections when using high L/t ratios can enable significant end forces to develop (27). Flexural specimens tested were in the range of 16:1 for Length: thickness (L/t) ratio, which is the lowest limit suggested for flexural modulus testing.

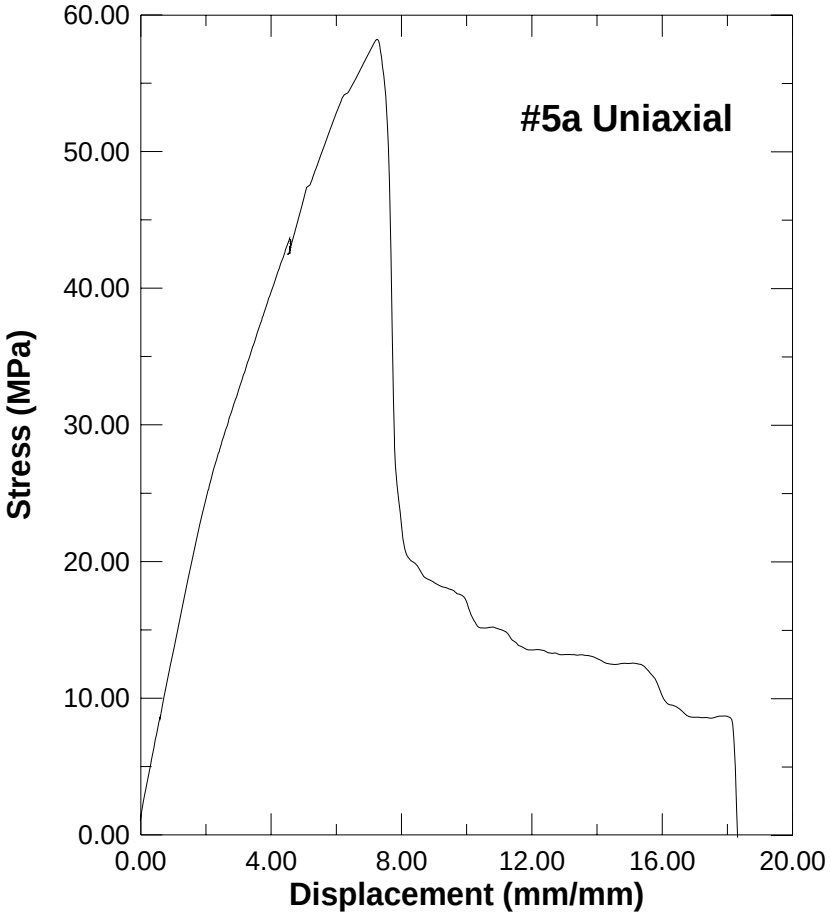

Figure 4.6 Flexural stress-deflection curve of a uniaxial specimen.

4.3.2 Proportional elastic limit (PEL)

The PEL averaged above 11 MPa for uniaxial samples and 13.8 MPa for $(0/90)_s$ samples. Previous PEL values of 7.2 MPa (2) and 9.0 MPa for SRFRC wee exceeded (6). The PEL deviated at a higher stress than the tensile tests. The PEL deflection was nearly 1 mm for uniaxial specimens and 0.85 mm for $(0/90)_s$. This was well above the PEL deflection values for glass SRFRC of 0.18 mm (23).

With SRFRC the PEL is a sharp bend with loss of linearity due to the first crack widening. No PEL point was evident in any flexural stress-deflection curves. The PEL

was similar to the “knee” response in the tension tests as only a slight slope change occurred. Here the PEL was an initial non-linearity as microcracking was initiated. This results from distributed cracking by the aligned continuous fibers.

The PEL to the LOP phase was stiffer than SRFRC composites due to fiber alignment across all cracks. The pseudo-linear response exists up to the LOP in almost all cases. This illustrates the increased efficiency of the proper fiber placement, alignment, and available length to bridge any crack.

4.3.3 Limit of proportionality (LOP)

The average values for the LOP are in the table 4.2. The LOP signifies the first permanent material damage. The $(0/90)_s$ composites average LOP deflection was less than one half the uniaxial composite’s deflection. The lamina orthogonal to the applied stress could not contribute as the outer most fibers carried the load alone. The four uniaxial specimens were tested only to LVDT range (±2.5 mm) end and showed little or no permanent damage.

4.3.4 Modulus of rupture (MOR)

The MOR was significantly higher than previous studies (1,2, & 6). The uniaxial specimens were twice the SRFRC values averaging nearly 50 MPa while the $(0/90)_s$ were 23 MPa. The uniaxial specimens MOR and LOP were very similar in value and curve location.

In only one of eight uniaxial tests carried to conclusion did the MOR differ from the LOP significantly. In seven tests strength decreased quickly over a 1-3 mm

deflection range after the LOP/ MOR. The one differing test had of 3 MPa difference between the MOR and LOP values but an increased deflection of 4.3 mm. This specimen (#13) shows the extended deflection as a plateau after the LOP before reaching the MOR.

Four of the five $(0/90)_s$ tests carried to conclusion had the MOR slightly higher than the LOP. This followed the uniaxial specimen's pattern. The average flexural stress difference was 2.5 MPa while the average deflection difference was 12.6 mm.

The one $(0/90)_s$ test that was ending at LVDT range showed damage after 2 mm of deflection. A stress plateau is observed past the LOP signified the growing permanent damage in the 0° layer and is shown in figure 4.7.

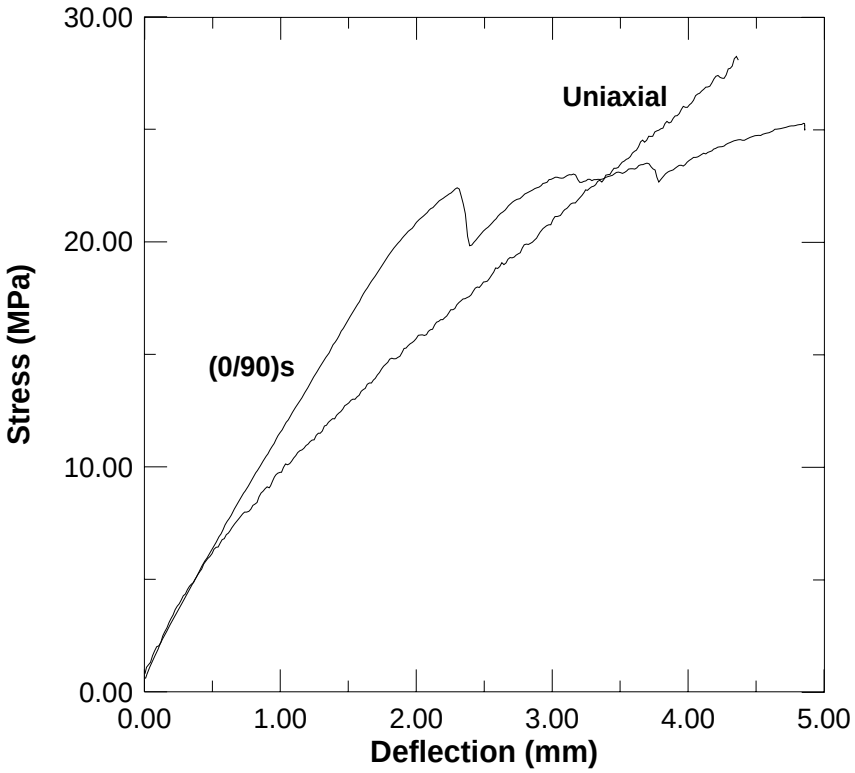

Figure 4.7 A uniaxial specimen vs. a $(0/90)_s$.

4.3.5 Overall

For uniaxial specimens the LOP/MOR point was extended to an average 5 mm range using a 305 mm span and 16:1 L/t ratios. A significant load carrying ability remains for several millimeters after the LOP/MOR. The LOP deflection values exceeded typical SRFRC values by a significant amount. Extending the mechanical properties further into the deflection zone can change this material's structural applications.

$(0/90)_s$ LOP range was extended to 2 mm with the MOR occurring at over 11 mm. After the MOR there is no catastrophic failure, rather the specimens load carrying ability steadily decreases.

4.4 Toughness

4.4.1 Introduction

The definition for toughness for brittle matrix composite testing varies widely. Toughness indexing was not performed due to the inability to reliably locate the first crack. Results of toughness measurements are in table 4.3. The tension toughness was normalized by multiplying the gage length and dividing by the cross sectional area. Since the ultimate strain didn't reach 1% in 9 of 12 uniaxial tension specimens, the 1% toughness was not used.

Table 4.3 Toughness Measurements

Type	Toughness at:	1% ε (N/mm)	Test end (N/mm)
0 T-G		-	16.08
$(0/90)_s$ T-G		16.42	42.49
0/90/0 T-G		12.30	14.94
$(90/0)_s$ T-G		15.73	27.96
$(\pm 45)_s$ T-G		3.26	3.77
0 T-PP		7.57	24.70
		MOR (N/mm)	
0 G-F		12.62	44.90
$(0/90)_s$ G-F		13.42	28.26

T= tension sample F= flexure sample G=AR glass PP= polypropylene

Table 4.3 Results from toughness measurements taken.

4.4.1 Tension

The tensile toughness was taken as the area under the load-LVDT elongation curve. This makes the results gage length dependent. Toughness has several contributing factors such as fiber tension, fiber breaking, fiber debonding, fiber plastic deforming, the matrix plastic deforming and cracking, the friction of broken fiber pullout from the matrix, and fiber-to-fiber friction during elongation or pullout (28).

The ultimate toughness values may not be well represented here. Many times ear cracking and grip shearing caused early test shut down leaving behind specimens that still had significant load carrying ability. The grips were operated at 5-7 MPa over a 45 cm^2 area resulting in a permanently reduced specimen thickness by test end. This energy was not counted in specimen absorption.

Higher energy absorption for the cross plies was due to the extended strain range before failure. Uniaxial specimens rarely broke without test apparatus influence. The single uniaxial specimen to break across its center had the highest toughness. Also, the ram pressed specimens absorbed almost three times more energy than the non-pressed specimens. The $(\pm 45)_s$ specimens had approximately 1/5 the uniaxial composites toughness. This was expected from fiber orientations exceeding ±30° off axis fiber alignment.

Uniaxial polypropylene specimens absorbed more energy than glass specimens due to an extended strain range. Their low strength limited testing apparatus effects. No polypropylene sample tested failed leaving the ultimate toughness still an unknown. All five specimens behaved consistently. Specimen #5 was taken to 8.5% strain and absorbed 108 N/mm and extremely consistent behavior in all specimens.

4.4.2 Flexure

The flexure toughness was taken as the area under the load- LVDT deflection curve divided by the specimen cross sectional area. Stress distribution changes the toughness contribution of the factors listed previously. Additional factors influencing flexural toughness are matrix yielding due to compression at the exit of a bridging fiber from the matrix, friction between the fiber and matrix or fiber due to local compression at the bend (28).

The uniaxial specimens absorbed the most energy due to fiber alignment with the stress. Delaminations formed in the $(0/90)_{sc}$ specimens after the formation of transverse

cracks in the 90° layers. This curved the specimen off the support anvil while it was still stressed, therefore the toughness may be less than reported.

4.4.3 Overall

Aligned fiber composite tension and flexure toughness dramatically increased compared to SRFRC composites. The toughness is usually defined as the work to fracture. However many specimens never failed, especially in flexural testing. Also, AR glass tension samples suffered from testing system influence lowering test results. Therefore, this performance was not the full composite potential.

Chapter 5

Failure Behavior & Mechanisms

5.1 Introduction

Fibers affect a composite's behavior through the fiber type, shape, amount, and distribution in the matrix (5). The fiber's type influences the composite with its Young's modulus, Poisson's ratio, ultimate stress, specific surface, surface texture, and affinity to bond to cement. Fiber shapes can be mats, rovings, short, continuous, single, films, and meshes. The fiber amount is the volume fraction. Fibers can be distributed randomly, linearized, or laminated (stacked sequences). This study maintained a constant volume fraction and used the conventional AR glass and polypropylene fiber material reinforcement. The only alterations compared to conventional FRC was using continuous fibers and stacking oriented lamina.

Fiber composite behavior depends on the microstructural interfacial zone, where stresses are transferred from the matrix to the fibers. The transfer efficiency controls crack spacing, toughness, ultimate loading in tension and flexure, ultimate straining, and deflections. Continuously aligned and placed fiber composites aim to establish stable microcracking throughout the entire material structure. This optimizes other performance factors (σ_{cu} , ε_{cu} , τ, toughness, ect.) and matrix material usage. Fibers are well known as crack arresters and closers, and can affect crack patterns. Fiber uniform placement and orientation in the cross sectional area allows more effective controlling of microcrack growth than random fiber placement. Failure behavior and mechanisms were similar to glass fiber reinforced plastics (GFRP) and other classical fiber/plastic behavior (29).

Tensile tests were halted at a specific strain to observe crack distribution and type. Steel blocks were epoxied to the surfaces freezing the crack pattern (5), while the load was held constant to inhibit crack closure during curing. The specimens were then vacuum impregnated with low viscosity yellow-dyed epoxy for optical study. The epoxy filled the existing crack structure and hardened permanently preserving the cracking state. The epoxy appears green due to the dark gray background of the cement matrix.

The images were captured by a 16 bit Sigma Scanpro software using S-type video and either an Infinivar Video microscope or a Mitutoya Ultraplan microscope at the Arizona State University Goldwater Optical Microscopy Laboratory. The Infinivar was fitted with a telescopic lens allowing magnifications ranging from 1.5X - 150X. The Mitutoya microscope had magnification settings of 100X, 200X, 500x, and 1000X under either normal or cross-polarized light. Specimens were ground smooth to the 0.3 μm alumina powder level.

5.2 Cracking Behavior

The optical studies viewed all three surfaces noted in figure 5.1. The x-y plane was the specimen surface, while the x-z plane was the cross sectional area perpendicular to the applied load. The y-z plane was the specimen thickness.

5.2.1 Distributed microcracking

The continuously aligned fibers allowed the formation of distributed microcracking throughout the composite material. This behavior was observed in tension tested AR glass and polypropylene specimens.

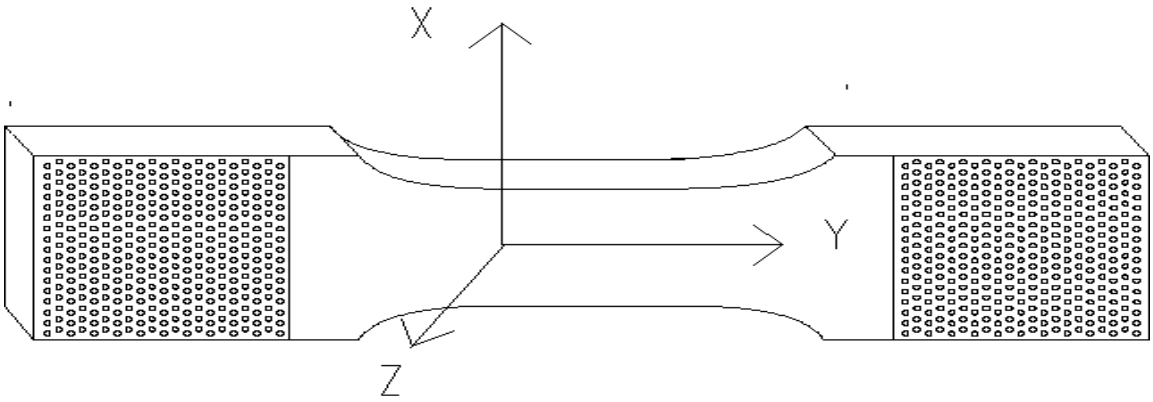

Figure 5.1 Planes of orientation for optical study.

5.2.1.1 AR glass uniaxial

Uniaxial specimen cracking was mostly perpendicular to the fibers/applied stress direction. Figure 5.2 illustrates microcracking on an AR glass y-z plane. Microcracking was observed between the large delamination cracks (green-yellow bands) caused by fiber/matrix debonding. Some crack shifting along the fiber axis and deviation from a direct perpendicular path was seen. Some crack splitting was also observed.

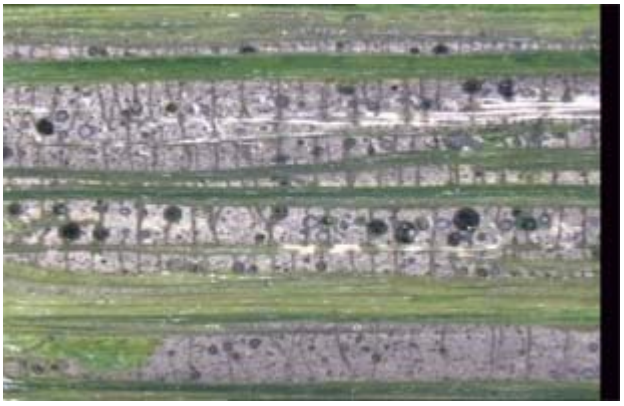

Image 26 - 8mm wide.

Image 28 - 4 mm wide.

Figure 5.2 Distributed microcracking in an AR glass uniaxial specimen.

Crack spacing ranged from 0.3 - 0.7 mm in the cases shown. Cracking was difficult to detect in some instances. Therefore, the range of spacing may even be smaller than noted here.

No glass specimens were frozen at an elevated strain level due to their erratic failures. The stiff glass fibers closed the microcracks making it difficult to discover a specimen with thoroughly distributed microcracking visible at lower magnifications. The

microcracking was visible at a 200X magnification level. However, a representative image of its distributed nature was too difficult to piece together.

5.2.1.2 Polypropylene

Polypropylene microcracking was seen in figure 5.3. All five polypropylene specimens clearly displayed microcracking on both the y-z and x-y plane due to higher strain levels attained. Cracking in the y-z plane is once again

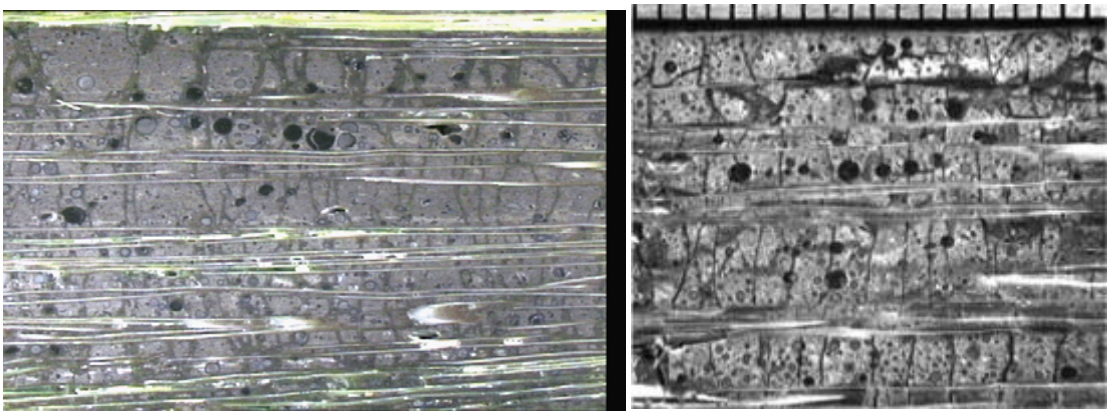

Image 46 - 12.5 mm wide. Image PPr3 - 20 mm wide.

Figure 5.3 Microcracking in a polypropylene specimen.

perpendicular to fiber direction. Debonding did cause delaminations but these cracks were not as wide as in the glass specimens. Crack spacing varied but was near the 1 mm average in these images. Surface cracks became visible at higher strain levels during testing. The microcracking was a slightly different pattern on the x-y plane than the y-z plane. The epoxied steel blocks may have froze the surface strains well but not the interior strains as the interior fibers apply closing force.

5.2.1.4 Flexure

Flexure specimens displayed microcracking with a wider spacing of 2-4 mm range when compared to tension cases. Distributed microcracking was underdeveloped due the stress relief from fiber/matrix debonding and the formation of delaminations. Further load application continued the fiber/matrix debonding, extending the delamination cracks. Figure 5.4 shows 200X magnifications of cracks with a glass roving on the bottom of both images.

The grid appearance of tension microcracking occurred in approximately 25% of the viewed specimens as pictured in the flex2 image. The rest of the specimens displayed cracks as in the flex3 image. The crack direction was off axis with a range of 15° - 45°. The microcracking also only existed in the tensile section.

Image flex1 – 1.1mm wide

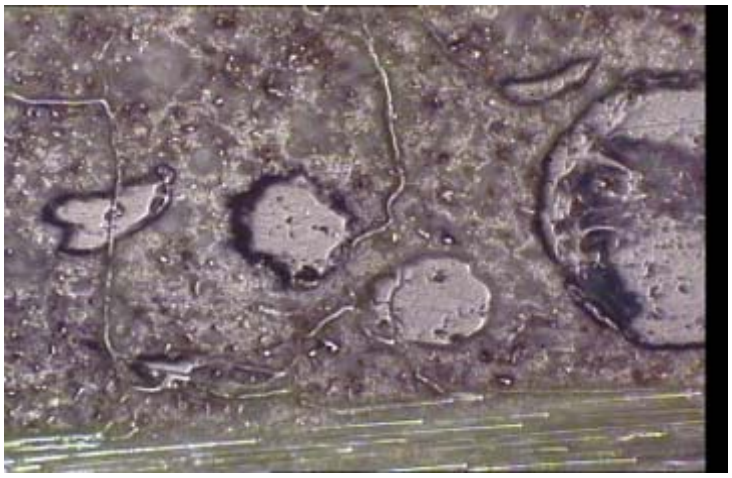

Image flex2 - 1.125mm wide

Image flex3 - 1.125mm wide

Figure 5.4 Microcracking in the tension zone of flexural specimens.

5.2.2 Patterns of microcrack deflection

The crack path deflections and patterns varied for different composites. The four Diamond and Bentur crack type patterns were observed here as displayed in figure 5.5 (10). Other patterns observed are included in the figure. The crack propagation direction was not included due to the posterior nature of the optical study.

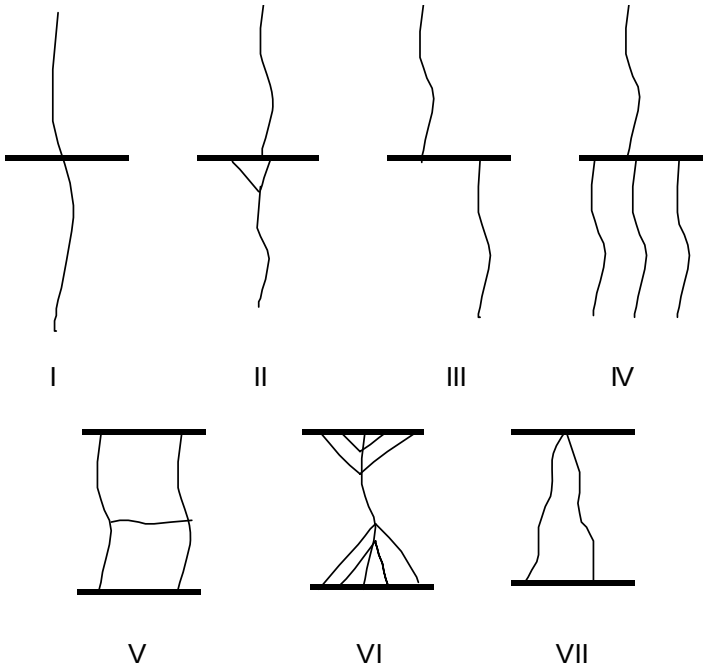

Figure 5.5 Types of microcracking patterns observed.

5.2.2.1 Tension tested AR glass

Glass specimens exhibited all types of patterns shown with some displayed in figure 5.6. Type III was the most frequent. Many of the glass specimen cracks shifted a

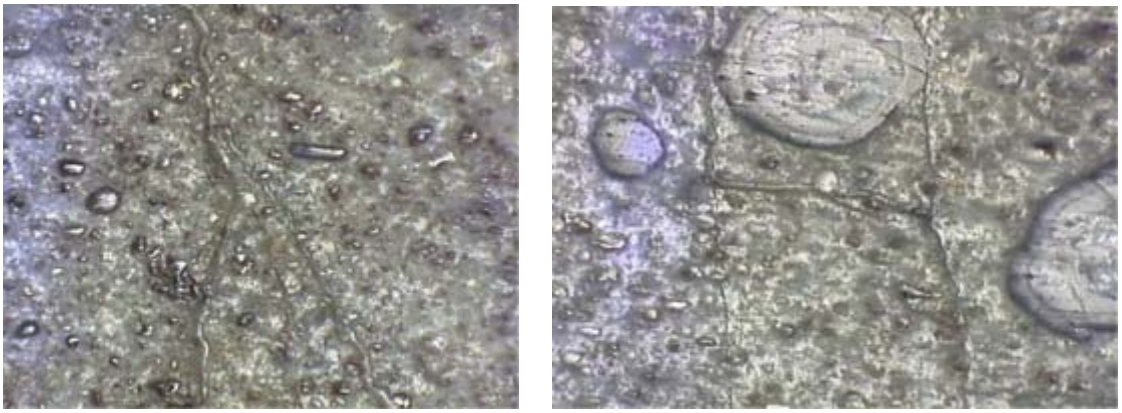

a) Gtimage 9 - 0.5 mm wide

b) Gtimage 7 - 0.5 mm wide

c) Gtimage1 - 0.25 mm wide

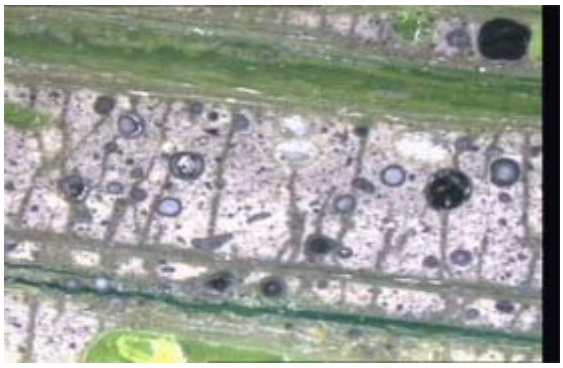

d) Image 20 - 1.75 mm wide

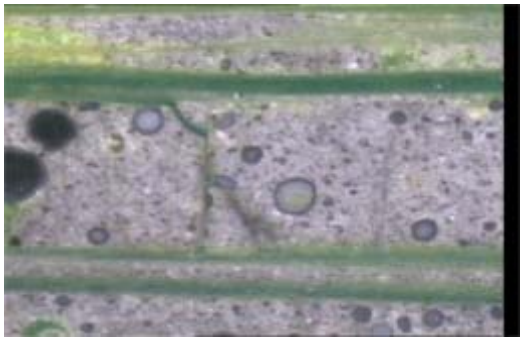

e) Image 38 - 0.75 mm wide

Figure 5.6 Cracking type examples in AR glass specimens.

very small amount and could only be observed at high magnifications (200X - 500X) as in figure 5.6c. Type V was observed in all specimens to some degree (5.6b). Type VI was infrequent but was demonstrated in figure5.6a and 5.6e. In 5.6e the perpendicular crack between fibers most likely occurred first. Following this, the fiber stretches further and the 45° crack formed breaking away a piece of the matrix. The 45° crack path was shorter than a path to a neighboring fiber requiring less energy. The image in 5.6a was a demonstration of crack branching. Full branching patterns were observed rarely in glass specimens. The glass usually developed crack splits with two or three branches.

Surface cracking occurred running parallel to the fibers and was very rarely traverse connecting the fiber debonding or intralaminar cracks.

5.2.2.2 Tension tested polypropylene

The uniaxial composite microcracking is shown in figure 5.7. All types of cracking patterns were observed. Figure 5.7a, b, and e displays a single crack shifting. The crack in 5.5a splits after fiber crossing and then shifts away in both directions debonding the fiber from the matrix between the two cracks. Type V was illustrated in 5.7c and type VI in 5.7d. Type II was shown in 5.7f and in figure 5.10b. Type I was demonstrated very clearly in other images but type III was the most common. Figure 5.5c shows a fibrillation debonding in the upper right hand corner.

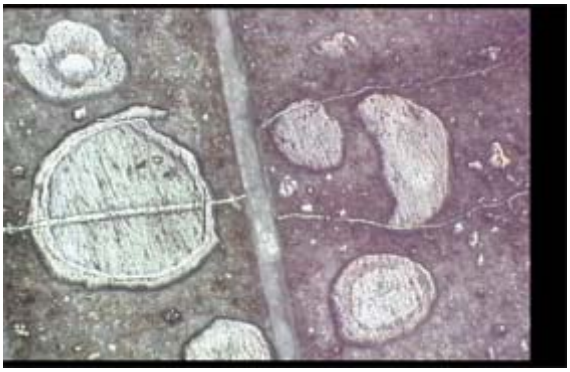

a) Image 11 - 2.25 mm wide

b) Image 8 - 1.125 mm wide

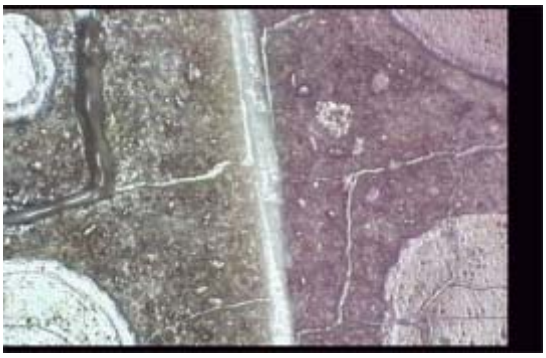

c) Image 14 - 2.25 mm wide

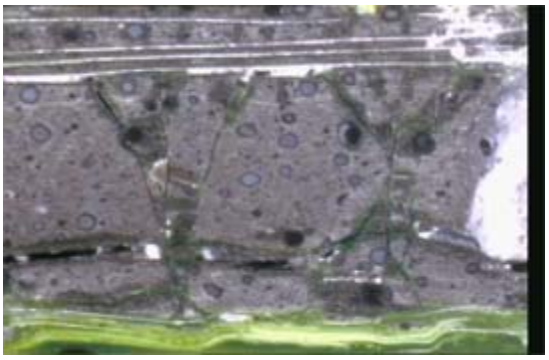

d) Image 40 - 5.5 mm wide

f) Imagepp8 - 1.125 mm wide

Figure 5.7 Crack Type II and IV demonstrating shifting and splitting.

Other images showed cracks parallel to the fibers connecting the transverse cracks. Also, parallel fiber cracking occurred frequently between transverse cracks in-between the fibers. Surface cracking occurred often with the polypropylene specimens.

5.2.2.3 Tension tested $(0/90)_s$ & 90/0/90

Distributed microcracking was not readily observed so the patterns were not as evident. The observed cracking occurred in similar patterns. Within the 90° layers was intralaminar cracking in the composites as pictured in figure 5.8.

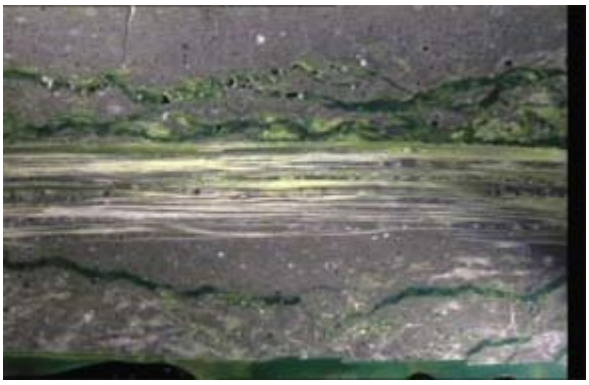

a) Image 100 - 25 mm wide

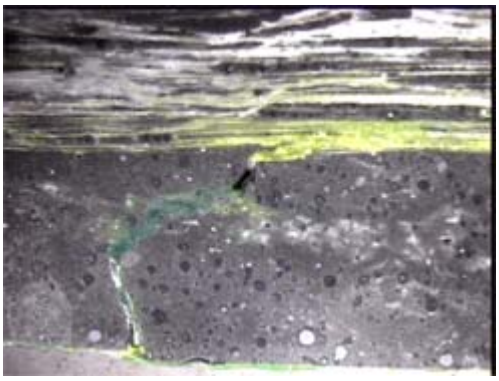

b) Image ten6 - 8mm wide

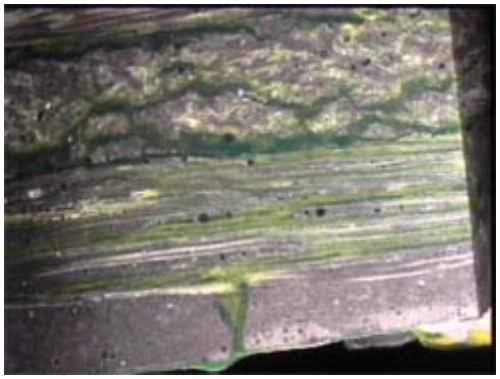

c) Image ten3 - 8mm wide

Figure 5.8 The cracking in cross-ply composites.

Cracks extended through the fiber/matrix interface in the layers orthogonal to the applied stress. The cracks reached into the interfacial zones to form delaminations. The cracks branched off and returned back to the fibers. An intralaminar crack that was not as fully developed is shown in figure 5.15c. Figure 5.8a shows a $(0/90)_s$ composite's cross

sectional area with the tensile stress out of the page. The fiber debonding into intralaminar cracks was evident appearing as the dark bands. Figure 5.8c was a 90/0/90 composite with the crack at the bottom of the image showing the distance between surface cracks. The surface crack reached into the adjacent layer, extending the interfacial debonding.

5.2.2.4 Flexure tested AR glass

Flexure specimens displayed behavior similar to the $(0/90)_s$ and 90/0/90 tension tested composites within the layers orthogonal to the applied stress as seen in figure 5.11a. The main crack was deflected along the fiber length. Finer cracking was observed under 200X magnification and was pictured in figure 5.4. This quasi-parallel cracking to the fibers occurred in the specimen's tensile zone.

5.2.3 Debonding

Distributed microcracking and fiber debonding became the mechanisms for larger scale cracking. Debonding led to macroscopic behavior such as delaminations, fiber pullout during fractures, deflections of cracks, and the intralaminar cracks.

5.2.3.1 AR glass tension uniaxial

Fiber debonding affected the uniaxial glass specimens as seen in figure 5.9.

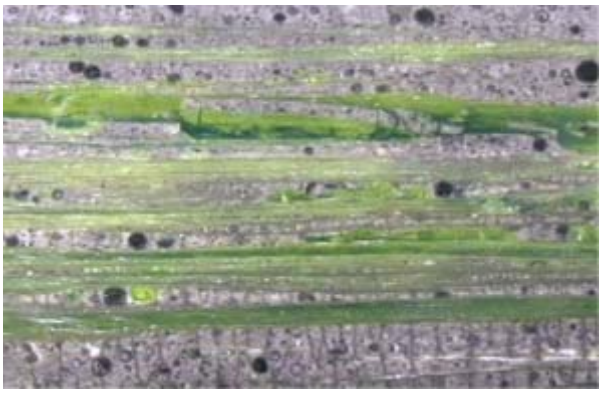

a) Image 31 - 10.5 mm wide

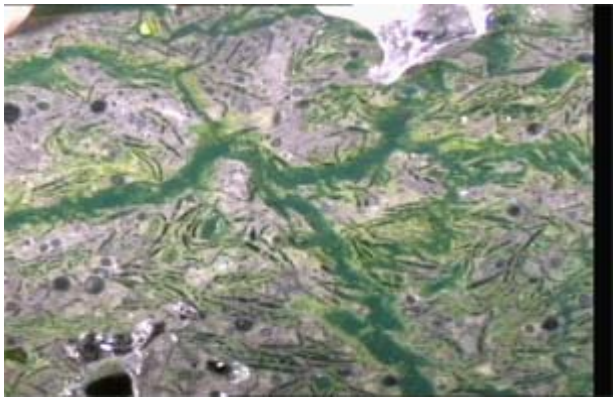

b) Image 34 - 4 mm wide

Figure 5.9 Debonding in glass uniaxial specimens

Figure 5.9a shows the characteristic dark bands on the y-z plane (thickness) while 5.9b shows their appearance on the cross sectional area. Almost all failures had some type of debonding associated with them. Whether the failure was shear grip tearing or simple cracking, the path included some measure of debonding. The figure 5.9a accentuates the size difference with the intralaminar debonding cracks compared to the distributed microcracks.

The ear cracks were a direct result of debonding due to stress intensity, or stress transfer of the load to the specimen center zone. These cracks did affect the LVDT signal enough to cause test ending. These ear cracks occurred in every polypropylene specimen but they weren't severe enough to cause test end.

5.2.3.2 Polypropylene

Polypropylene specimens exhibited debonding with a thinner width as shown in the figure 5.10. Figure 5.10a was the surface (x-y plane) of a specimen and 5.10b is the y-z plane.

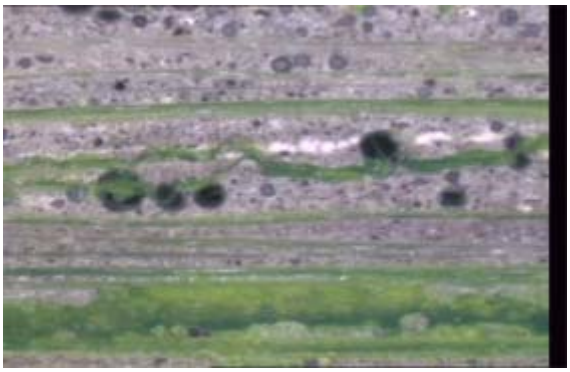

a) Image 37 - 8 mm wide

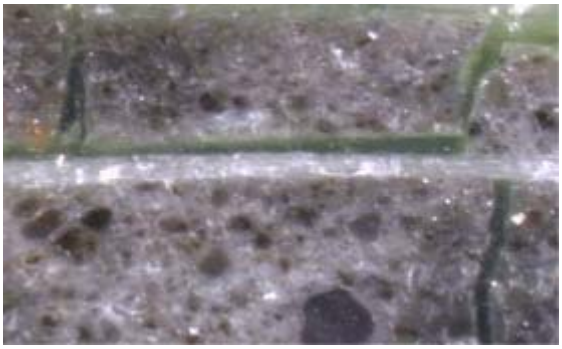

b) Image 39p - 1.125 mm wide

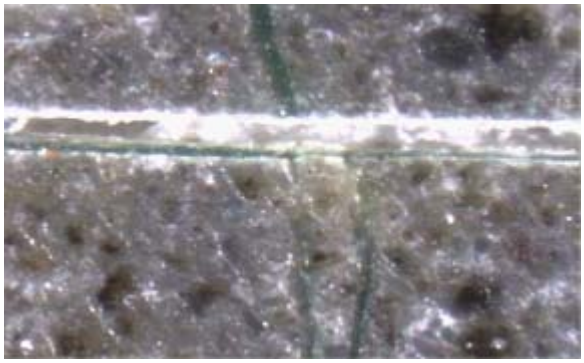

c) Image 40p - 1.125 mm wide

Figure 5.10 The green (dark) bands in polypropylene specimen from debonding.

5.2.3.3 AR glass $(0/90)_s$, $(90/0)_s$ & 90/0/90

Debonding, as shown before in figure 5.8, were the first cracks in the 90° plies. With this alignment the fibers are at there weakest and depend totally on the bond strength. This caused intralaminar cracking, which was along the fiber axis and traversed the specimen width. Without full roving impregnation there existed uncoated fibers providing inherent weak locations. Several examples show how this weak bond allowed unevenly spaced traverse cracking. Hashin described this as typical cross ply composite behavior (30). The cracking continues within the layer traveling from one weak fiber bond to the next, which was similar to flexure behavior. This is displayed in figures 5.11 and 5.12. Sometimes the cracks reached the delamination of the adjacent interfacial layer. This occurred frequently in the $(0/90)_s$ composites and less in the others.

5.2.3.4 Flexure

The glass uniaxial flexural specimens formed debonding cracks parallel to the x-y plane as shown in figure 5.11. The macroscopic view was seen in 5.11a as the debonding caused intralaminar cracks in the 90° layer of the image's lower portion and the 0° layer in the top portion. Figure 5.11b exhibits the developing crack path within the 90° layer as it enters the upper left hand corner from a glass strand and enters the next. The crack the leaves the strand at both ends with reduced width entering other strands. This behavior was clearly demonstrated in 5.11c as the crack path was seen traveling directly through the strands.

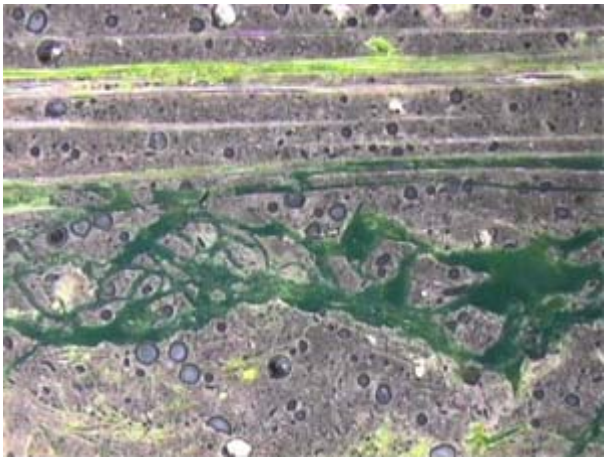

a) Image a5 - 20 mm wide

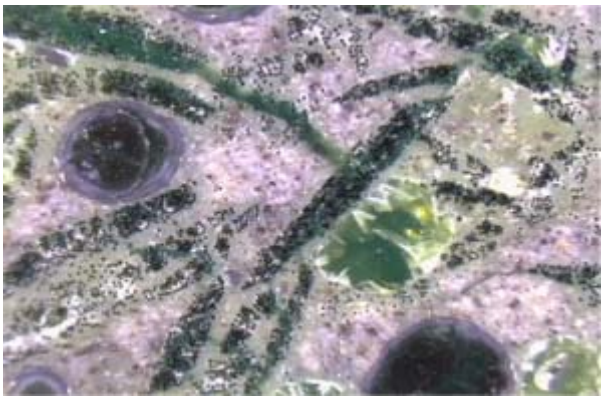

b) Image flexb2 - 5 mm wide

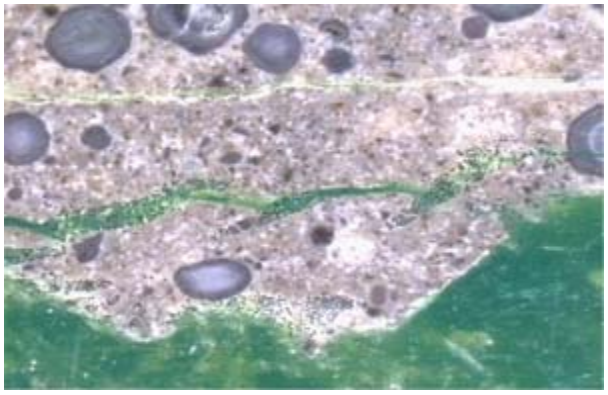

c) Image 82 - 1.75 mm wide

Figure 5.11 The debonding cracks traveling from fiber to fiber strand.

These cracks formed discrete layers called delaminations. All uniaxial specimens tested to end showed some degree of delaminations as shown in figures 5.15a and 5.15b.

The debonding and interfacial zone cracking led to delaminations with crack growth from one fiber rich zone to the next. This micro-mechanical process is shown in figure 5.12 sequence. The magnifications of 100X, 200X, 500X, and 1000X show the actual path of the intralaminar crack through the glass fiber/interface zone. The black circles are the fibers on end in the x-z plane as force is out of the page.

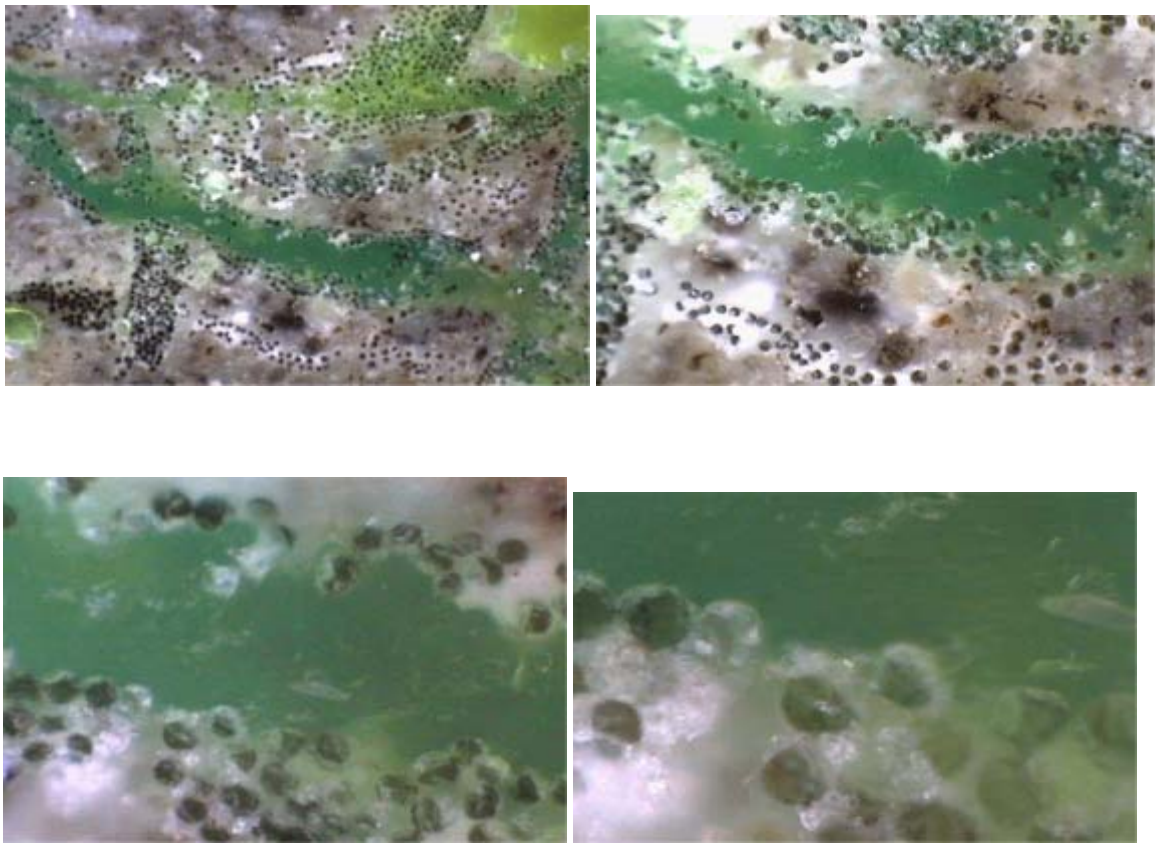

Figure 5.12 Debonding at a microscopic level in a flexure specimen

5.2.4 Delamination or intralaminar cracking

Delamination cracking was observed excessively in the glass flexure and tension crossply specimens. The delamination of the cross ply composites in tension was evident. It was common to have delaminations from one grip to the other.

The $(0/90)_s$ samples showed these cracks running along the interface of the lower 0° and 90° layer and sometimes just within the 90° layer. They were present in every cross ply specimen by test end. The formation of the first major debond /delamination layer signified the LOP in flexure specimens. The delaminations are a result of transverse intralaminar cracks, which originate from fiber/matrix debonding in the 90° layers. Two of the five flexure crossply delaminations were across the top interfacial zone.

The cracked tensile zone on one flexure cross ply was peeled back rather easily due to the extensive delamination by test end. The crack path was mainly within the 90° layer with some sections of the 0° ply peeling off.

5.2.5 Intralaminar cracking

Intralaminar cracking is considered cracking along the fiber axis. At the microscopic level, intralaminar cracking started as debonding and here it formed large surfaces as shown in figure 5.13. A singular crack in a flexural sample is shown in 5.13c.

Half the flexure composite failures were due to fiber/matrix debonding across the width. The ends of two uniaxial flexural samples shown in 5.13a relate the failure mode.

Compression cracking on all uniaxial specimens ran in two directions and is displayed in 5.13b. One direction was along fiber direction while the other perpendicular reaching down into the specimen. The compression zone also suffered from shattering.

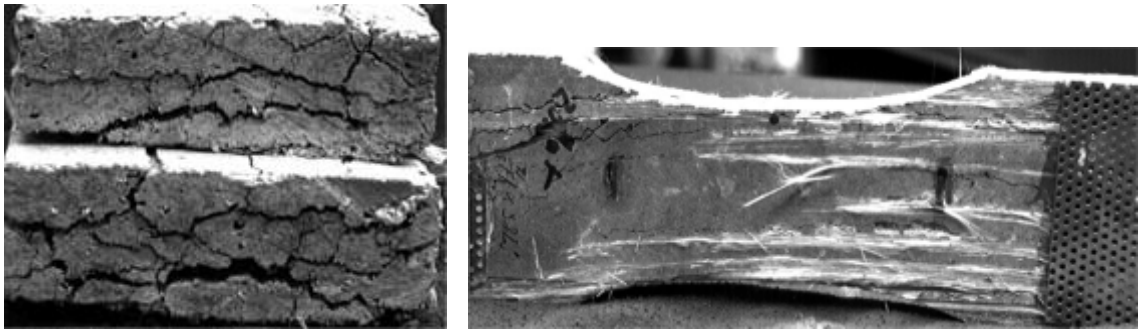

a) Image f11-13-2 - 7.5 cm wide b) Image t23 - 20.0 cm wide

Figure5.13 The intralaminar crack in specimens.

Image 5.13d was a tensile specimen with ear cracking which is an intralaminar crack. The ear cracks were due to stress transfer into the center section with all glass uniaxial specimens containing one. The polypropylene composites had significant ear cracking but none affected the test. This result was affected by the roving's fibrillations bridging the crack surface where the glass composites had no resistance.

5.2.6 Fiber fracture

Half of the flexure specimens fractured their tensile zones. Some fiber fractures were straight across the specimen width as shown in figures 5.14a. These cracks had

fiber pullout lengths of approximately 10mm with no debonding redirection of the crack. Fibers were pulled out the length of specimen distorting and obscuring the fracture surface.

With other flexure specimens debonding tended to deflect the main failure crack along the fiber length (5.14b). Fibers fracture occurred along an indirect path. There was less fiber pullout associated with the deflected cracking.

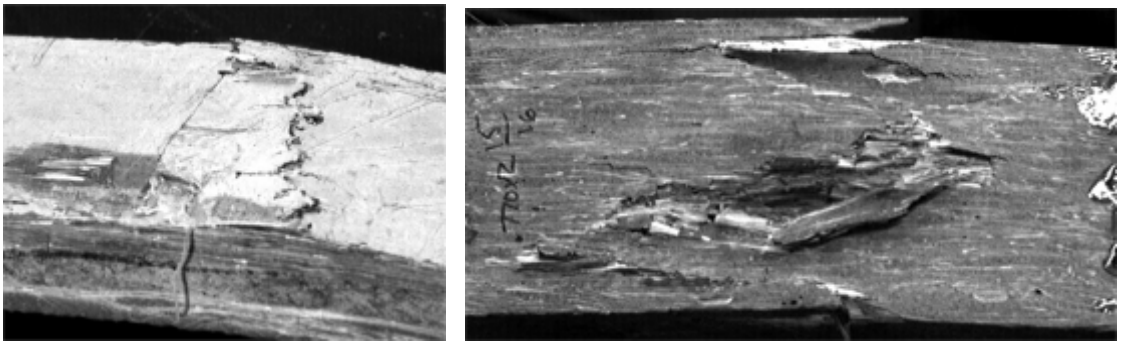

a) Image f9-2 - 7.5 cm wide b) Image f5a-2 - 18 cm wide

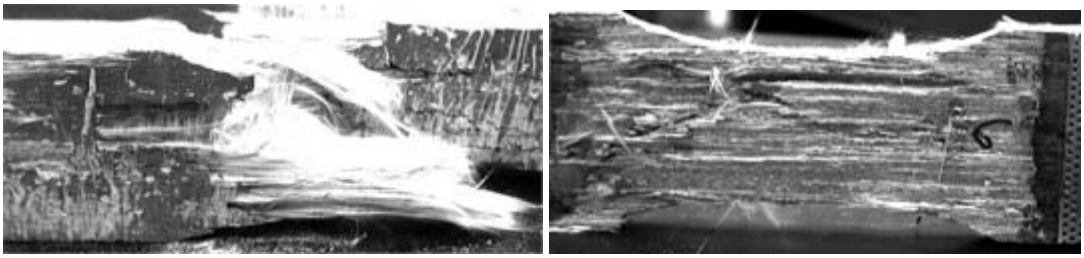

c) Image t322 - 15 cm wide d) Image t6 - 20 cm wide

Figure5.14 Fiber fracture in specimens

The tensile failure of a $(0/90)_s$ composite is shown in 5.14c. Two of the five composites failed in this manner. The delamination of the interior 90° layer and the deflection of the 0° layer crack was evidenced. The fiber pullout was seen. The extended length was due to the lack of roving impregnation loss. Image 5.14d was a uniaxial tensile specimen with crack deflection along the fiber axis as the failure traversed across the piece. Only two of eleven specimens failed this way. Little fiber pullout occurred with these two breaks.

5.3 Testing effects

Tension testing of fiber reinforced cements can be difficult to perform without influencing the results. The testing apparatus contained hydraulic grips with available pressure variation in the range of 4 -7.5 MPa. Even at this low pressure the specimen behavior and failures were affected as seen in figure 5.15.

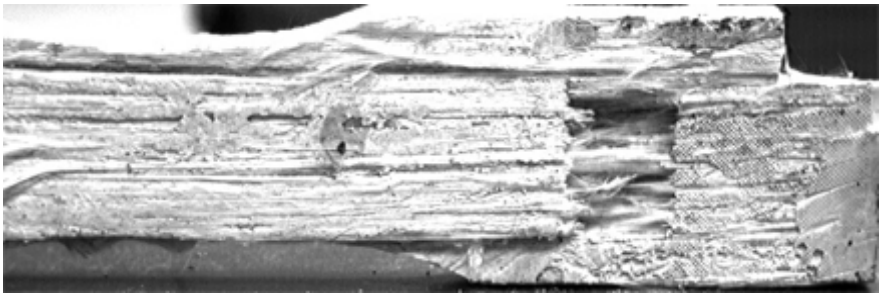

a) Image t26 - 20 cm wide

a) Image t16 - 20 cm wide

c) Image t3-2 - 10 cm wide d) Image t301

Figure 5.15 The effect of tensile testing uniaxial glass specimens.

Several ultimate failures were caused or induced by the grips (figures 5.15a-d). Some tears were noticed early in tests of 0/90/0 samples as in figure 5.15c. This rendered that layer ineffective resulting in an outward bending in the direction of the failed layer. Combination tears of the grips and ear cracks were present at ultimate failure in uniaxial specimens as shown in figure5.15d. Several specimens had delaminations that halted where the grips started after the specimen was removed. Also, specimens were noticeably thinner in the grip hold area due to grip pressure.

5.4 Pressed vs. non-pressed specimens

All specimens not ram pressed (#2- #7 0/90/0) failure by fracture. In the 23 test specimens that were ram pressed only 3 failed by fracture, all being crossplys. Their performance was noted in the table 5.1. The modulus of elasticity was one half the $(0/90_s)$'s value while ultimate stress was significantly lower.

Specimen	Lay up	E_c (GPa)	σ_u (GPa)
2	0/90/0	9.22	25.71
3	0/90/0	10.72	17.95
4	0/90/0	10.65	25.66
7	0/90/0	4.00	17.91
5	0	11.22	38.78

Table 5.1 The effects of no ram pressing

The polypropylene sample that was not ram pressed behaved like the other four except in the initial response of the stress-strain curve. The modulus value was lower compared to the other four after which the curve behaved as the others.

REFERENCES

1 Bentur, Arnon, & Mindness, Sidney, Fiber Reinforced Cementitious Composites, Elsevier Science Publishers LTD, 1990.

2 Balaguru, P. N., & Shah, S. P., Fiber-Reinforced Cement Composites, Magraw-Hill Inc., 1992.

3 Li, V.C., & Wu, H.-C.,"Pseudo Strain-Hardening Design in Cement Based Composites," High Performance Fiber Reinforced Cement Composites: Proceedings of the International RILEM/ACI Workshop (Proceeding 15), Ed. Reinhardt, & H.W., Naaman, A.E., E & FN Spon, 1992, pp.371-387.

4 Li, C., "Mechanical Behavior of Cementitious Composites Reinforced With High Volume Content of Fibers," Doctoral Dissertation Arizona State University, May 1995.

5 Brandt, A.M., Cement Based Composites: Materials, Mechanical Properties, and Performance, E & FN Spon, 1995.

6 Mobasher, B., "Reinforcing Mechanism of Fibers in Cement Based Composites," Doctoral Dissertation Northwestern University, June 1990.

7 Majumdar, A. J., & Laws, V., Glass Fiber Reinforced Cement, BSP Professional Books, 1991.

8 Marsh, H. N., & Clarke L. L., "Glass Fiber Reinforced Cement Based Materials," Fiber Reinforced Concrete: ACI Publication SP-44, American Concrete Institute, 1974, pp. 247-264.

9 Mobasher, B., Stang, H., & Shah, S. P., "Microcracking in Fiber Reinforced Concrete," Cement and Concrete Research, Vol. 20, 1990, Pergamon Press, pp. 665-676

10 Wang, A. S. D., "Fracture Analysis of Interlaminar Cracking," Interlaminar Response of Composite Materials: Composite Material Series Volume 5, Ed. Pagano, N. J., Elsevier Science Publishers B. V., pp. 69-109

11 Mallick, P. K., Fiber-Reinforced Composites: Materials, Manufacturing and Design, Marcel Dekker Inc., 1993

12 Bijsterbosch, H., & Gatmans, R. J., "Pultrusion Process: Nylon 6/Glass Fibers," FRC '90 Fiber Reinforced Composites, pp. 101-104.

13 Meyer, Raymond W., Handbook of Pultrusion Technology, Chapman and Hall, 1985.

14 Krenchel, H., & Hansen, S., "New Recipes and New Production Techniques for High Performance FRC Materials," High Performance Fiber Reinforced Cement Composites: Proceedings of the International RILEM/ACI Workshop Proceeding 15, Ed. Reinhardt, & H.W., Naaman, A.E., E & FN Spon, 1992, pp.65-83.

15 El-Korchi, T., Toutanji, H., Katz, R. N., Leatherman, G. L., Lucas, & H., Demers, C., "Tensile Testing of Fiber Reinforced Cementitious Composites," Fiber - Reinforced Cementitious Materials: Materials Research Society Symposium Proceedings Volume 211, Ed. Mindness, S., & Skalny, J., Materials Research Society, 1990, pp 221-228.

16 Hattori, T., Suzuki, K., Nishigaki, T., Matsuhashi, T., Saito, K., & Shiraki, K., "Development of Panels Made with Continuous Carbon Fiber Reinforced Cement Composite," Fibre Reinforced Cement and Concrete: Proceedings of the Fourth RILEM International Symposium Proceedings 17 , Ed. Swamy, R. N., E & FN Spon, 1992, pp.988-999.

17 Johnston, C. D., "Methods of Evaluating the Performance of Fiber-Reinforced Concrete," Fiber-Reinforced Cementitious Materials: Materials Research Society Symposium Proceedings Volume 211, Ed. Mindness, S., & Skalny, J., Materials Research Society, 1990, pp 15-24.

18 Dyczek, J. R. L., & Petri, M. A., "Polypropylene FRC: Fiber-Matrix Bond Strength," Fibre Reinforced Cement and Concrete: Proceedings of the Fourth RILEM International Symposium Proceedings 17 , Ed. Swamy, R. N., E & FN Spon, 1992, pp. 324-342.

19 Hibbert, A. P., & Hannant, D. J., "Toughness of Fiber Cement Composites," Composites, April 1982, Butterworth & Co., pp. 105-111.

20 Singh, B., Walton, P. L., & Stucke, M. S., "Test Methods Used to Measure the Mechanical Properties of Fiber Cement Composites at the Building Research Establishment," Testing and Test Methods of Fiber Cement Composites: Rilem Symposium 1978, The Construction Press, 1978, pp. 377-388.

21 Hansen, W., & Tjiptobroto, P., "Tensile Strain Hardening in Fiber Reinforced Cement Composites," High Performance Fiber Reinforced Cement Composites: Proceedings of the International RILEM/ACI Workshop Proceeding 15, Ed. Reinhardt, & H.W., Naaman, A.E., E & FN Spon, 1992, pp.419-428.

22 Beaudoin, James J., Handbook of Fiber-Reinforced Concrete: Principals, Properties, Developments and Applications, Noyles Publications, 1990.

23 Page, C. L., "Microstructural Features of Interfaces in Fibre Cement Composites," Composites, April 1982, Butterworth & Co., pp. 140-151.

24 Brandt, A. M., “Influence of the Fiber Orientation on the Energy Absorption at the Fracture of SFRC Specimens,” Brittle Matrix Composites 1, Ed. Brandt, A M., Li, V. C., & Marshall, I.H., Woodhead Publishing Limited, 1994, pp. 403-420.

25 Hashin, Z., “Analysis of Cracked Laminates: A Variational Approach,” Mechanics of Materials, Vol. 4, 1985, Elsevier Science Publishers B. V., pp. 121-136.

26 Karam, G. N., “Effect of Fiber Volume on Tensile Properties of Real Unidirectional Fiber-Reinforced Composites,” Composites, March 1991, Vol. 22, Butterworth-Heinemann Ltd., pp. 84-88.

27 Hibbert, A. P., & Hannant, D. J., “Toughness of Cement Composites Containing Polypropylene Films Compared with Other Fibre Cements,” Composites, October 1982, Butterworth & Co., pp. 393-399.

28 Hannant, D. J., Fiber Cements and Fiber Concretes, John Wiley & Sons, 1978.

29 Talreja, R., “Stiffness Properties of Composite Laminates with Matrix Cracking and Interior Delamination,” Engineering Fracture Mechanics, Vol. 25, Numbers 5/6, 1986, Pergamon Press Ltd., pp. 751-762.

30 Hashin, Z., “Analysis of Stiffness Reduction of Cracked Cross-ply Laminates,” Engineering Fracture Mechanics, Vol. 25, Numbers 5/6, 1986, Pergamon Press Ltd., pp. 771-778.

APPENDIX A

Wiring Diagrams For The Filament Winding System

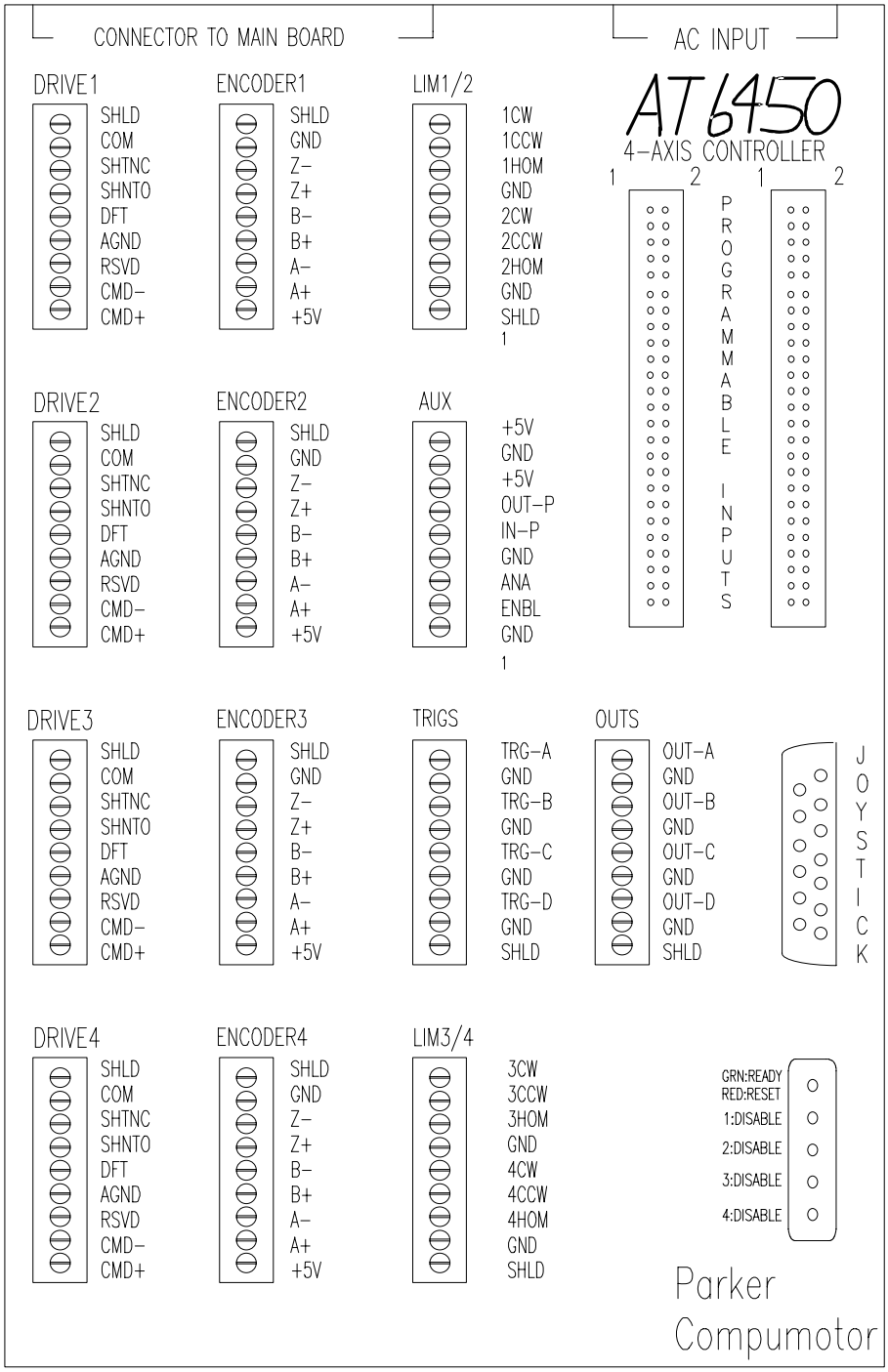

Figure A.1 The AT6450 controller

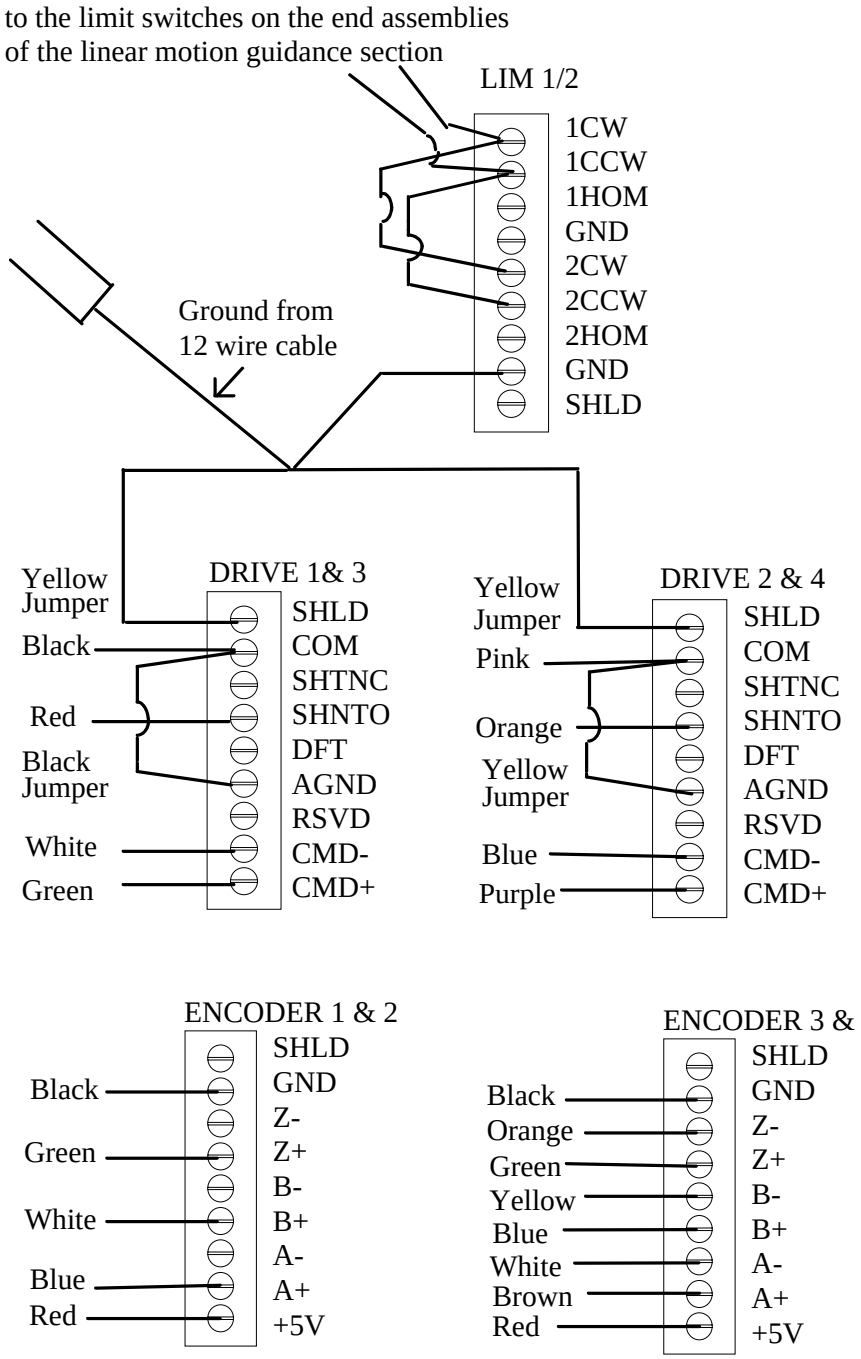

One 12 wire cable is used for drives 1 & 2 and one for drives 3 & 4.
One 10 wire cable is used for encoder s 1, 2, 3, & 4.

Figure A.2 The AT6450 controller wiring diagram.

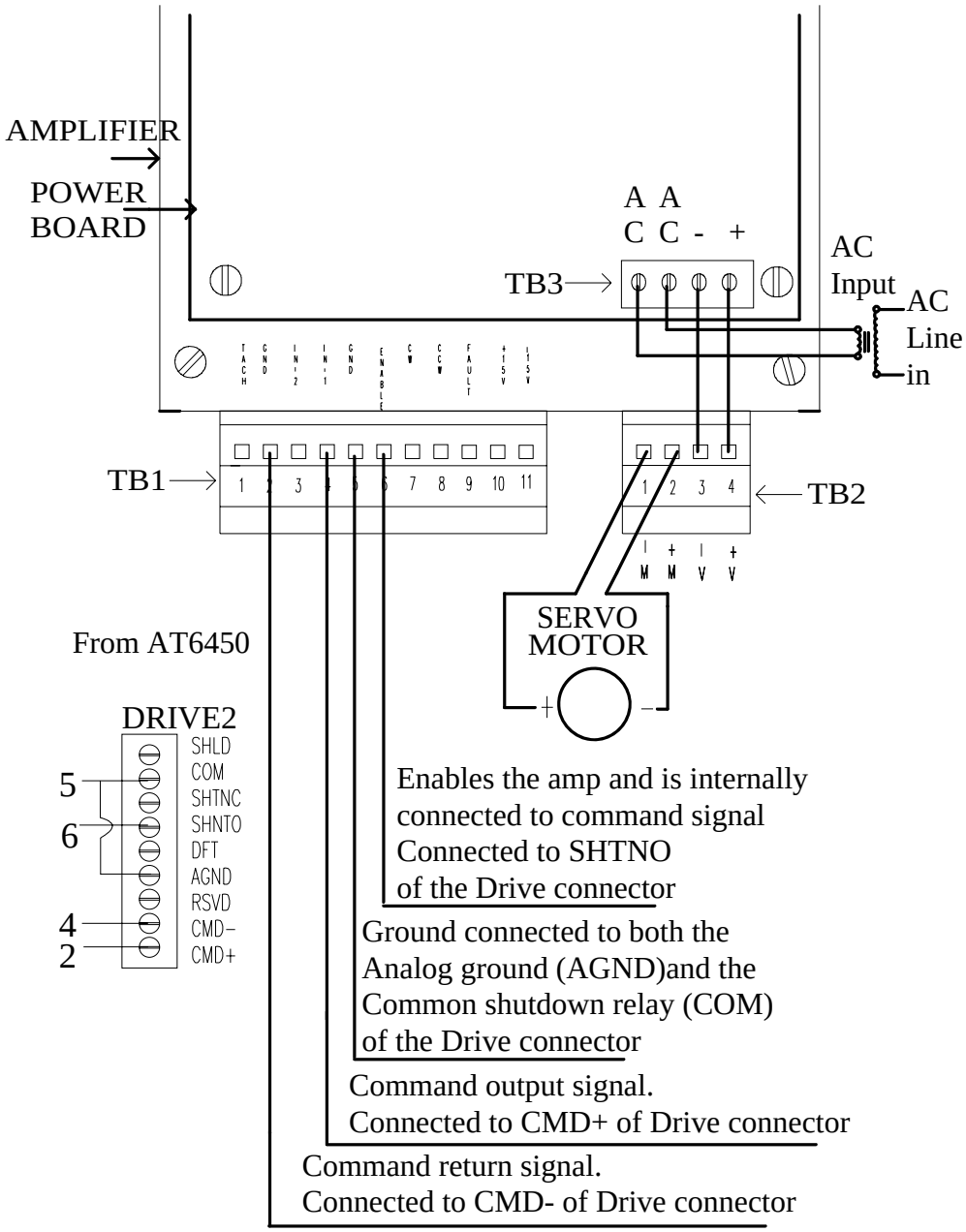

Figure A.3 The wiring diagram for an amplifier.

APPENDIX B

Motion architect 6000 Series command language: example commands

Motion Architect 6000 Series control language: example commands

TAS - Transfer Axis Status - this command returns the status of all axis specified or all four if none are specified. There are 32 bit assignments include Moving/Not Moving (1st bit), Direction CCW, CW (2nd bit),CW or CCW hard limit hit (yes/no) (15th, 16th bits), etc. This command was useful for finding the cause of stopped motion or other incurred difficulties in the development of the system.

ERES -Encoder Resolution - This sets the number of encoder counts per unit travel. The encoders here are 500-line encoders and have a 2000 count/revolution post-quadrature resolution requiring ERES2000. To insure accurately moved distance and velocity the ERES value must be the as the encoders resolution. Range is 200 - 1,024,000.

SMPER- Maximum Allowable Position Error -This sets the maximum allowable position error before the error condition occurs and stops motion. The error is the difference between the actual position and the command position. Range is 0 - 200,000,000 with 0 meaning do not monitor the position error.

SGP, SGV, SGI - Proportional Feedback Gain, Velocity Feedback Gain, and Integral Feedback Gain. This command allows control of the feedback gains in the servo algorithm. Ranges are 0.0 - 2,800,000.0 for all three with the default values of 0.5 for proportional and 0.0 for the others.

TGAIN- Transfer Servo Gains- This command displays the current gain values.

PSET - This command sets the new absolute position for referencing. It will also offset all captured positions before its activation.

TPE, TPER - Transfer Position of Encoder and Transfer Position Error. The first transfers the current position of the each encoder in encoder steps while the second gives the position error on each axis(TPER=TPE-TCP). Remember position error cannot exceed SMPER value.

DRIVE- Drive Enable - energizes or de-energizes the servomotor/drive combination. 1 = enabled , 0 = disabled. Also the command position (TCP) becomes the actual position(TPE)

LH - Hard Limit Enable - This command gives the hard wired limit status on each axis for CCW and CW motion. There are four combinations possible,

Both disabled = 0

CCW enabled, CW disabled = 1

CCW disabled, CW enabled = 2

Both enabled = 3

D, V, A, AD - Distance, Velocity, Acceleration, and Deceleration. These commands are used to input the actual values for distance, velocity, acceleration, and deceleration.

GO - Initiate Motion - This command tells the motor to go according to the inputted motion parameters.

<CTRL>K - Kill Motion - Kills motion on all axis. This is used for emergency stop situations.

Motion Toolbox VI's used by LabView to communicate with Motion Architect

Set Absolute/Incremental Mode - decides whether moves are made based upon current or absolute position. Since we don't have to go off a reference point but the current position for the system its set in the incremental mode (0 for the input).

Set Continuous/Preset Mode - chooses whether the axis move a preset distance or move continuously at a given velocity. The axis is set for the preset mode because the inputs determine the specifications of the sample and the distance is the controlling parameter.

Encoder Resolution - sets the resolution the system to 4000 counts/revolution.

Enable Drives - is inputted from the control panel and energizes the motors.

Send 6000 Block - sends valid 6000 command strings to the 6000 controller.

Initiate Motion - starts motion on the specified axis.

Set Distance - the inputted value gives the total number of encoder counts that the motor will move if it is incremental mode as we are.

Set Velocity - gives the velocity of the axis in units/second

Set Acceleration & **Set Deceleration** - set the acceleration/deceleration in units/second^2.

Wait For Move - waits for all the motors to come to rest before returning to the next program step.

Kill Motion- instantly stops all motion on all axes.

APPENDIX C

Tension Test Results

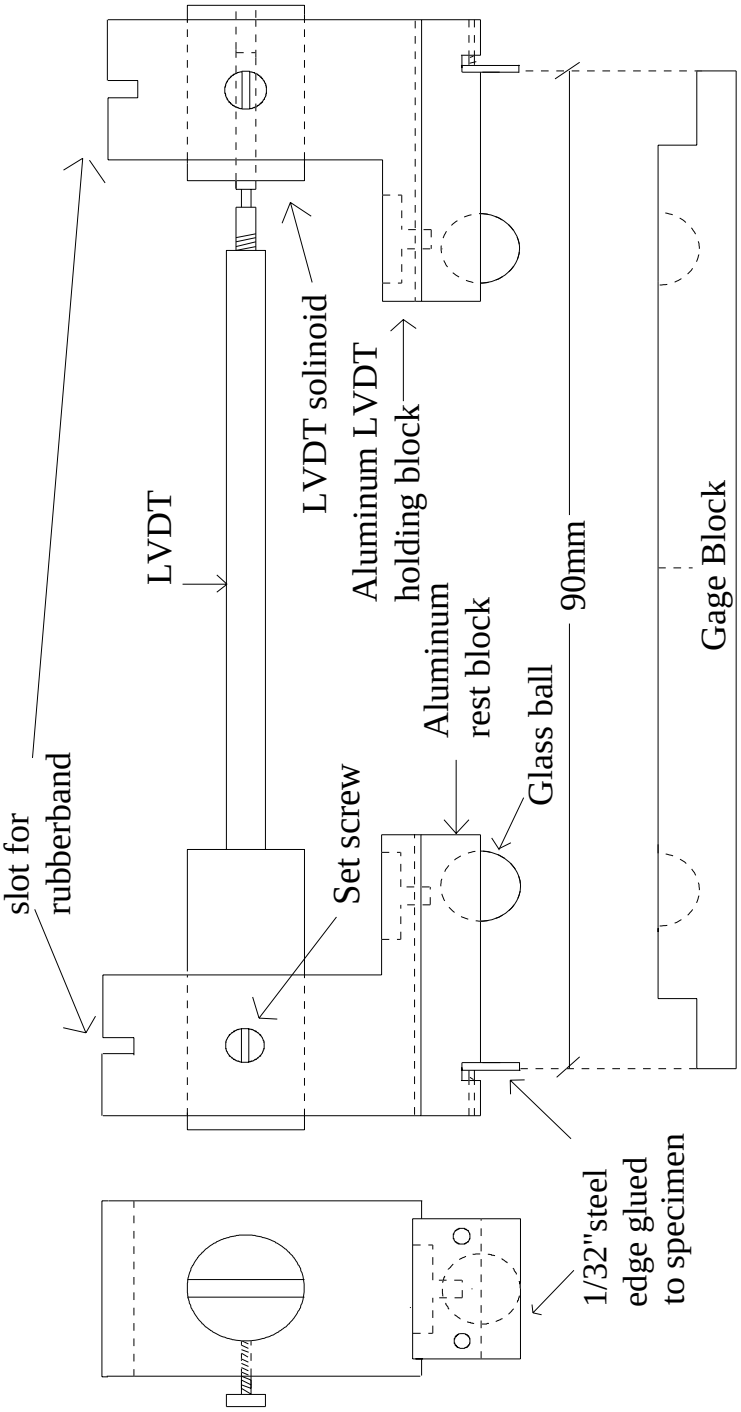

Figure A-5 LVDT Setup For Tension

Table C.1 Tension Test Results

Tension

specimen	E (MPa)	Ultimate stress	Strain ult pt	Test end strain	Toughness G (ult)	G (1%)	BOP stress	BOP strain
0/90/0		MPa	mm/mm	mm/mm	N/mm	N/mm	MPa	mm/mm
#2	9223	25.71	1.08%	1.40%	17.55	4.27	4.39	5.62E-04
#3	10720	17.95	1.92%	1.16%	13.91	11.62	3.20	2.72E-04
#4	10650	25.66	1.15%	1.77%	21.81	14.53	4.93	4.44E-04
#7	3998	17.91	0.69%	0.69%	6.49	6.49	2.79	6.00E-04
average	**8648**	**21.81**	**1.21%**	**1.25%**	**14.94**	**9.23**	**3.83**	**6.26E-04**
stdev	**2325**	**3.88**	**0.36%**	**0.33%**	**4.74**	**3.85**	**0.83**	**1.12E-04**
(0/90)s								
#11	26070	32.25	3.94%	3.94%	81.43	16.86	x	x
#12	32350	39.43	1.47%	2.61%	66.47	18.43	9.64	4.30E-04
#13	17104	26.92	0.87%	1.41%	17.55	12.99	10.31	9.98E-04
#32	22550	41.7	1.29%	1.29%	22.14	13.80	6.26	8.31E-04
#33	10084	51.06	1.13%	1.13%	24.88	20.02	4.20	3.47E-04
average	**21632**	**38.27**	**1.74%**	**2.07%**	**42.49**	**16.42**	**7.60**	**6.52E-04**
stdev	**6430**	**6.95**	**0.88%**	**0.96%**	**25.16**	**2.42**	**2.37**	**2.63E-04**
90/0/90								
#9	13kN jump	23.28	1.13%	1.34%	20.09	13.36	9.48	1.96E-03
#15	10kn jump	38.84	1.25%	4.65%	33.53	15.94	j	j
#16	11668	28.41	0.79%	0.79%	14.07	0.00	9.46	6.65E-04
#17	10593	35.62	1.36%	1.87%	44.15	17.89	4.05	3.08E-04
average	**11131**	**31.54**	**1.13%**	**2.16%**	**27.96**	**15.73**	**7.66**	**0.00**
stdev	**538**	**5.69**	**0.17%**	**1.25%**	**10.88**	**5.90**	**2.41**	**0.00**
0/0/0								
#5	11220	38.78	0.53%	1.78%	28.90	22.83	12.11	1.04E-03
#6	30548	50.4	0.82%	1.36%	39.18	29.09	4.70	1.57E-04
#10	22089	47.18	0.52%	0.52%	12.50	12.50	7.62	3.78E-04
#18	29390	45.85	0.32%	0.32%	7.31	7.31	6.61	2.07E-04
#20	21230	51.17	0.47%	0.47%	10.37	10.37	7.98	3.83E-04
#21	27065	50.2	0.56%	0.56%	14.20	14.20	6.12	2.38E-04
#22	18110	41.51	0.42%	0.42%	8.58	8.58	6.23	3.43E-04
#23	22990	51.4	1.56%	1.56%	23.08	8.57	5.75	2.19E-04
#24	21275	33.37	0.41%	0.41%	7.66	7.66	4.85	2.10E-04
#26	19400	42.33	0.45%	0.45%	9.07	9.07	7.07	3.75E-04
average	**22332**	**45.22**	**0.61%**	**0.78%**	**16.08**	**20.16**	**7.52**	**4.72E-04**
stdev	**4133**	**4.98**	**0.23%**	**0.47%**	**8.58**	**5.41**	**1.43**	**1.51E-04**
45/-45								
#27	n/a	3.35		0.70%	1.62	1.62		
#28	5941	3.9		2.67%	4.39	2.24		
#29	8256	5.87		1.40%	3.67	3.02		
#31	5815	5.58		2.58%	5.38	3.50		
average	**6671**	**5.12**		**1.99%**	**3.77**	**3.26**		
stdev	**1057**	**0.81**		**0.54%**	**0.60**	**0.45**		

		Ultimate	Strain	Test end	Toughness		BOP	BOP
Polypropylene								
#1	26543	13.37	2.62%	2.62%	24.72	7.93	8.61	3.59E-04
#2	23845	12.62	2.66%	2.66%	23.11	7.36	7.82	1.01E-03
#3	20116	12.34	2.77%	2.77%	25.46	7.75	7.22	4.61E-04
#4	31793	13.22	2.81%	2.81%	25.84	7.66	7.93	4.07E-04
#5	10179	18.56	2.71%	2.71%	24.39	7.15	6.02	5.07E-04
average	**22495**	**14.02**	**2.71%**	**2.71%**	**24.70**	**7.57**	**7.52**	**5.49E-04**
stdev	**5878**	**1.82**	**0.06%**		**0.76**	**0.25**	**0.72**	**1.84E-04**
				Gbar8.56%		**#5 PP**		
				158930		J/m^2		

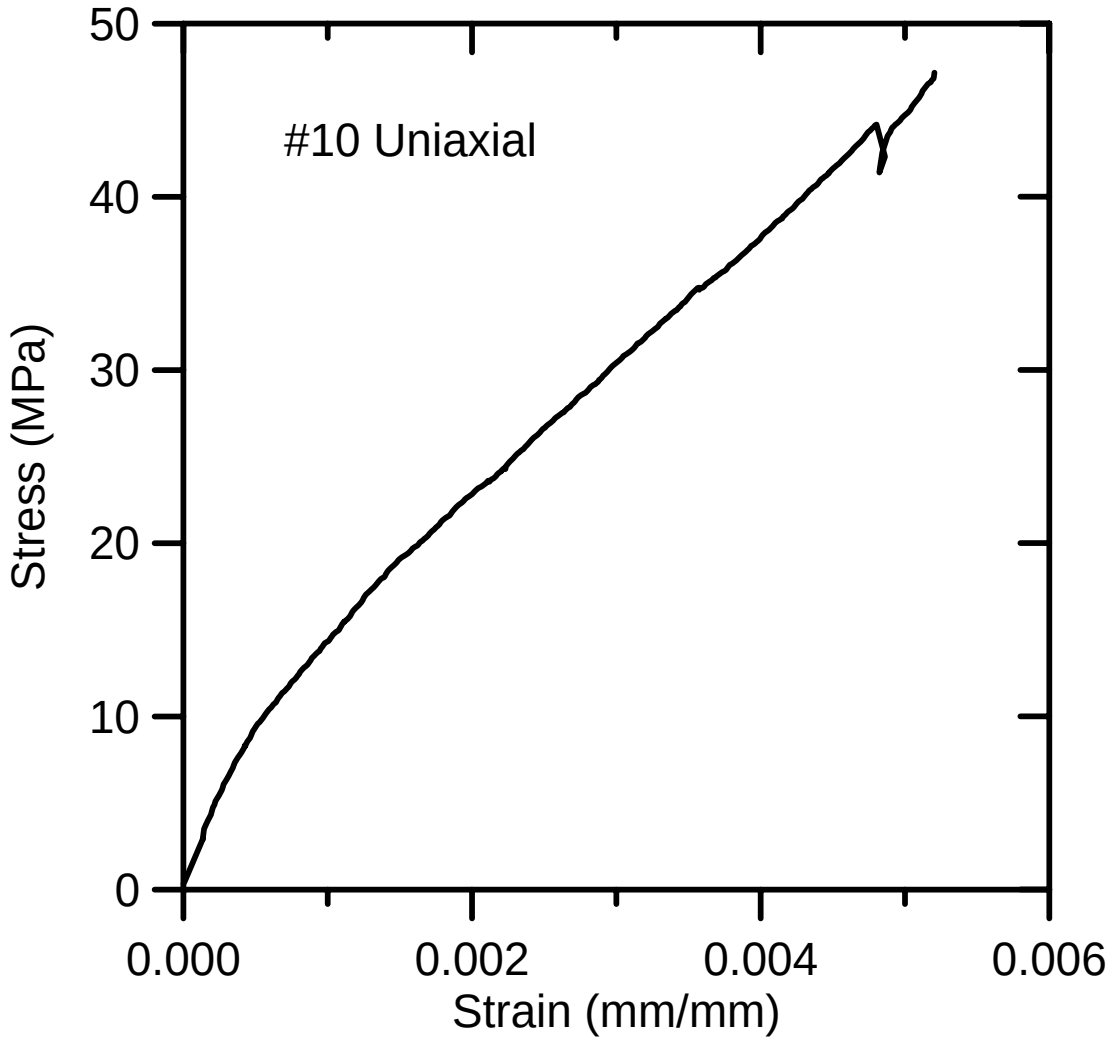
#10 Uniaxial
Stress (MPa)
Strain (mm/mm)
0
10
20
30
40
50
0.000
0.002
0.004
0.006

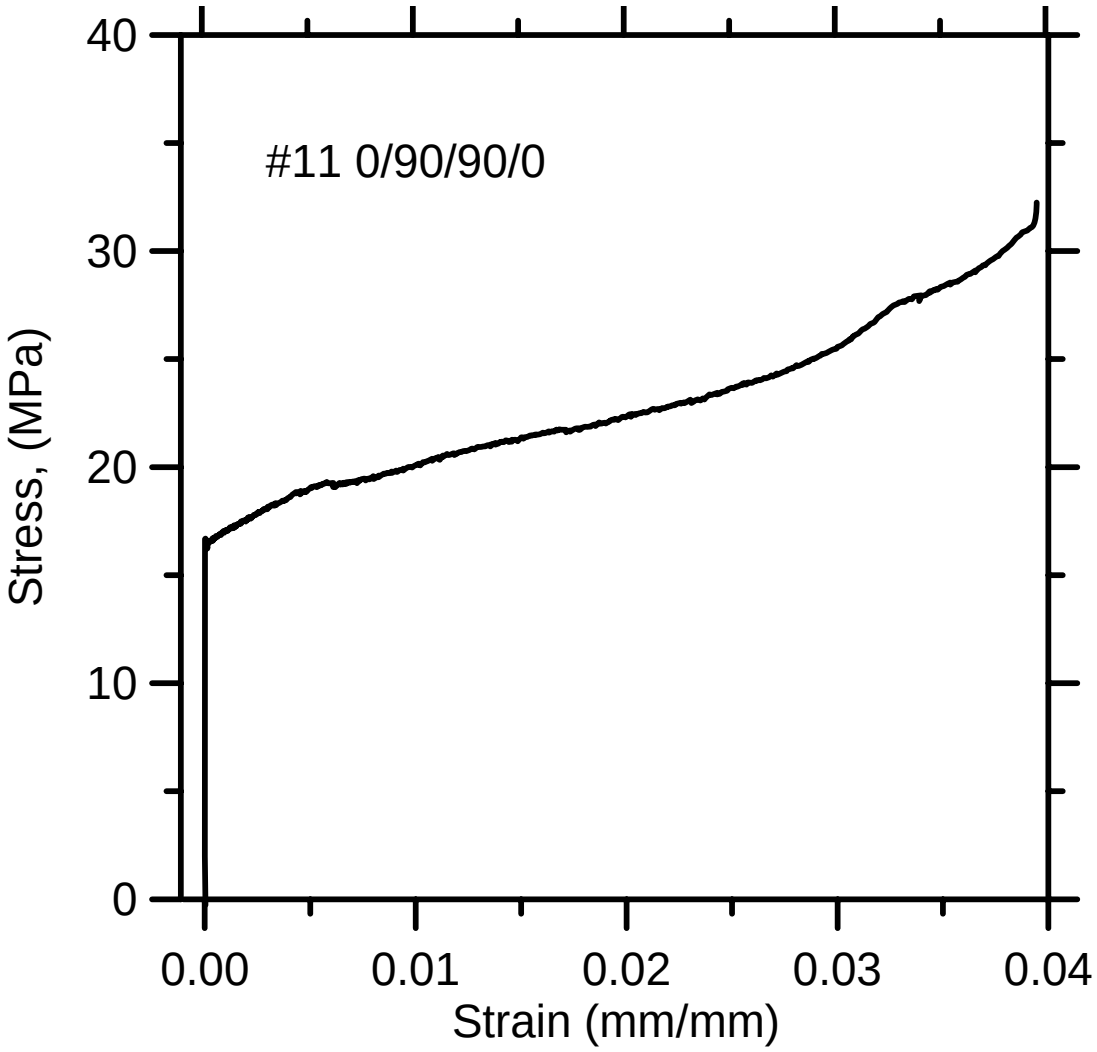
#11 0/90/90/0
Stress, (MPa)
Strain (mm/mm)
0
10
20
30
40
0.00
0.01
0.02
0.03
0.04

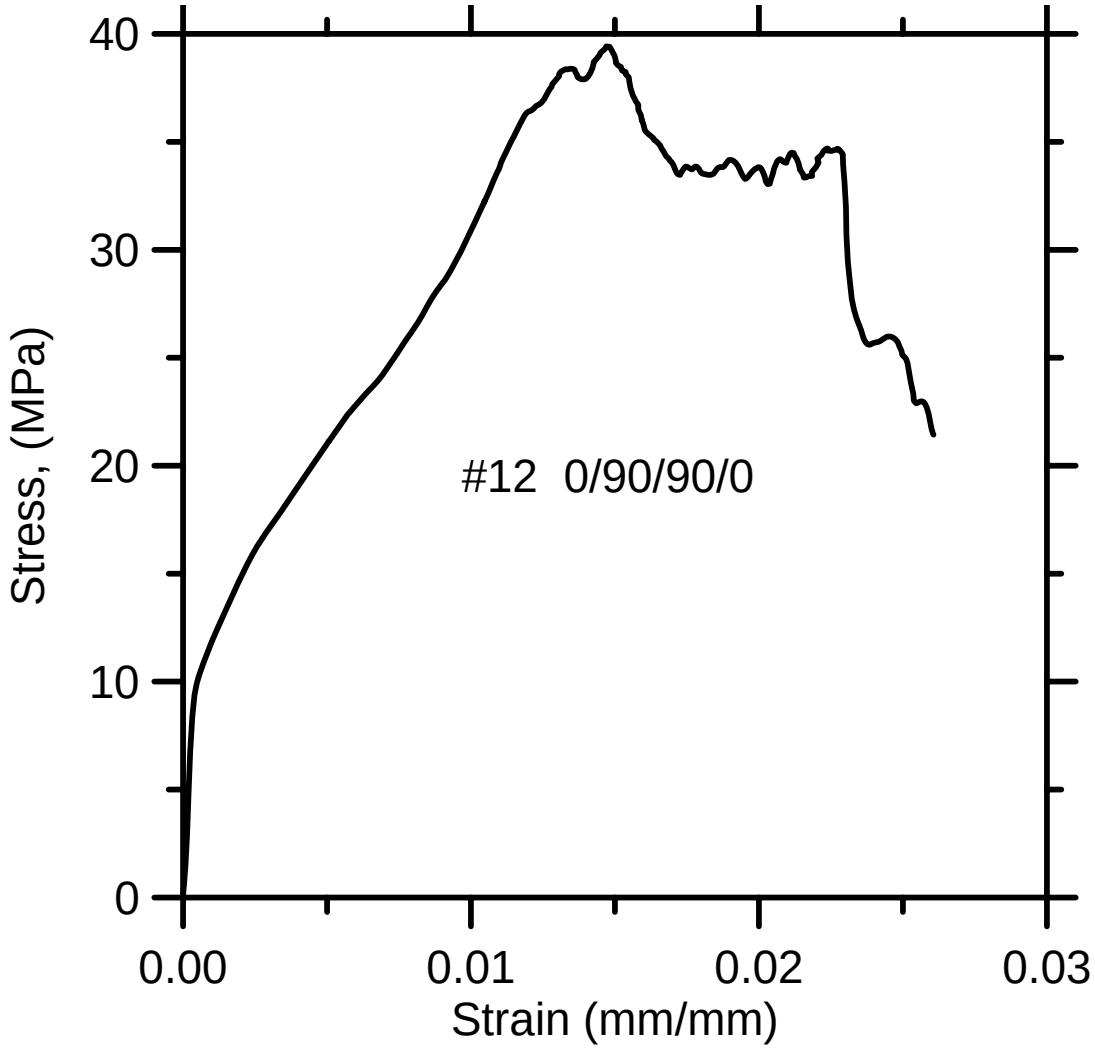
40
30
20
10
0
Stress, (MPa)
#12 0/90/90/0
0.00
0.01
0.02
0.03
Strain (mm/mm)

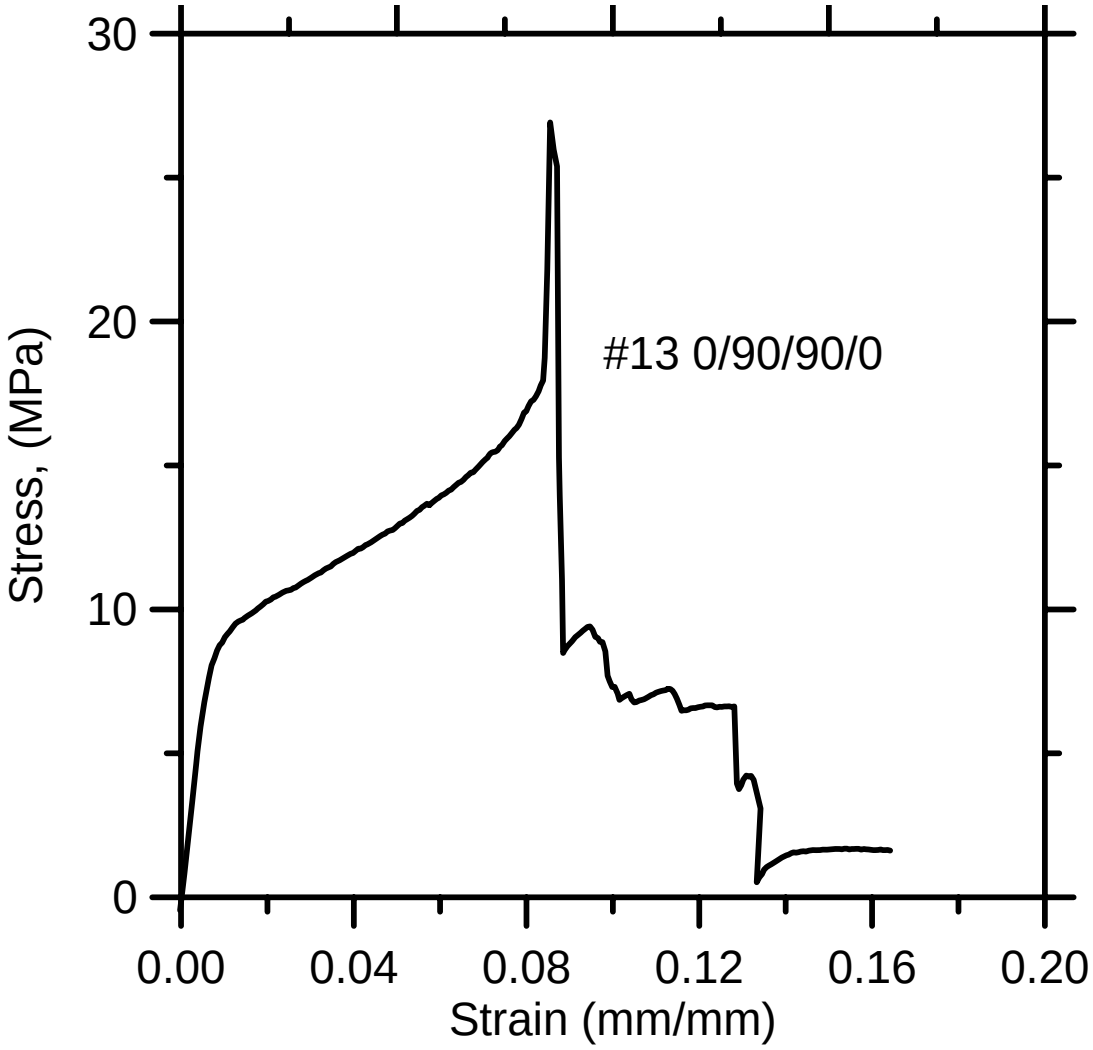
30
20
10
0
Stress, (MPa)
#13 0/90/90/0
0.00
0.04
0.08
0.12
0.16
0.20
Strain (mm/mm)

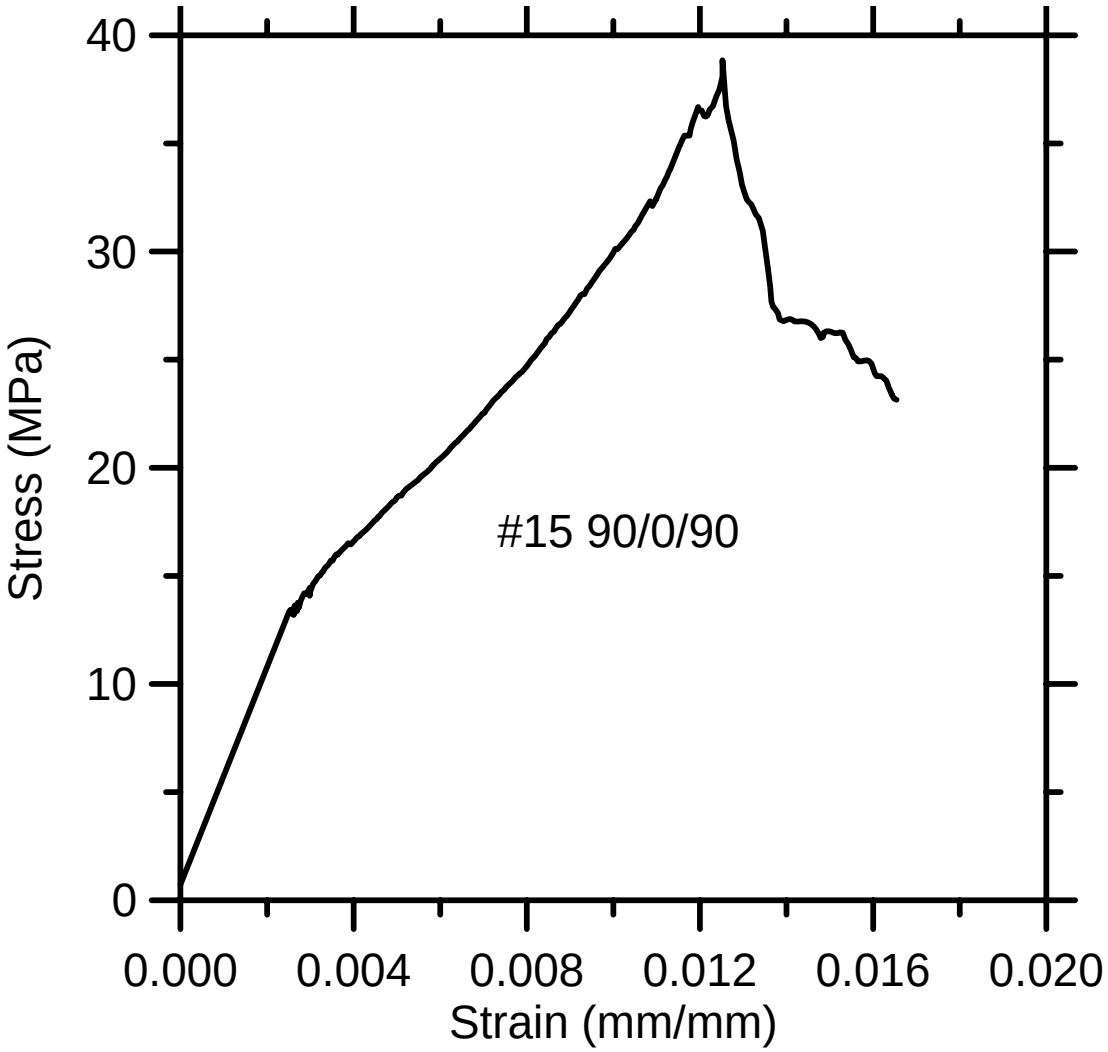
40
30
20
10
0
Stress (MPa)
#15 90/0/90
0.000
0.004
0.008
0.012
0.016
0.020
Strain (mm/mm)

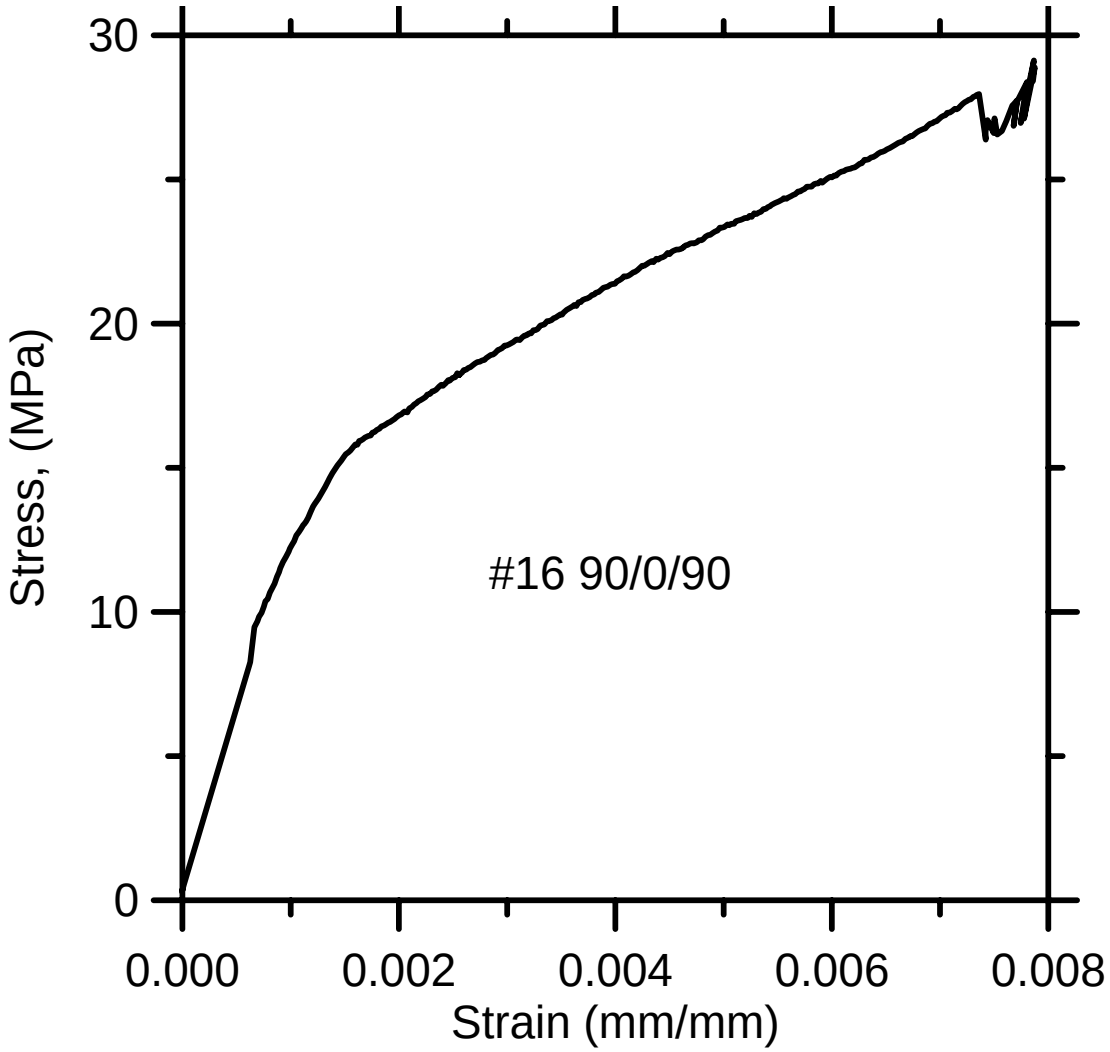
30
20
10
0
Stress, (MPa)
#16 90/0/90
0.000
0.002
0.004
0.006
0.008
Strain (mm/mm)

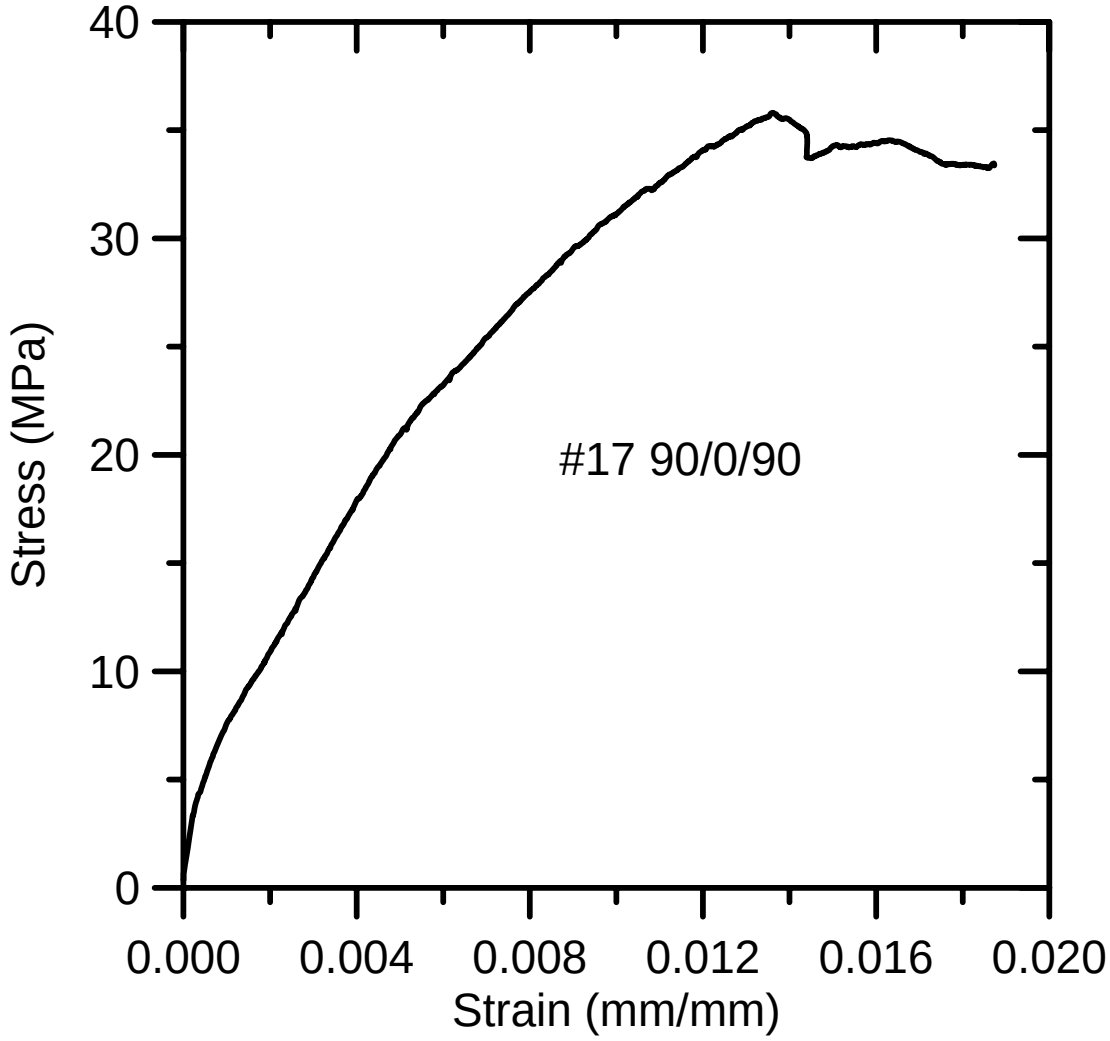
40
30
20
10
0
Stress (MPa)
#17 90/0/90
0.000
0.004
0.008
0.012
0.016
0.020
Strain (mm/mm)

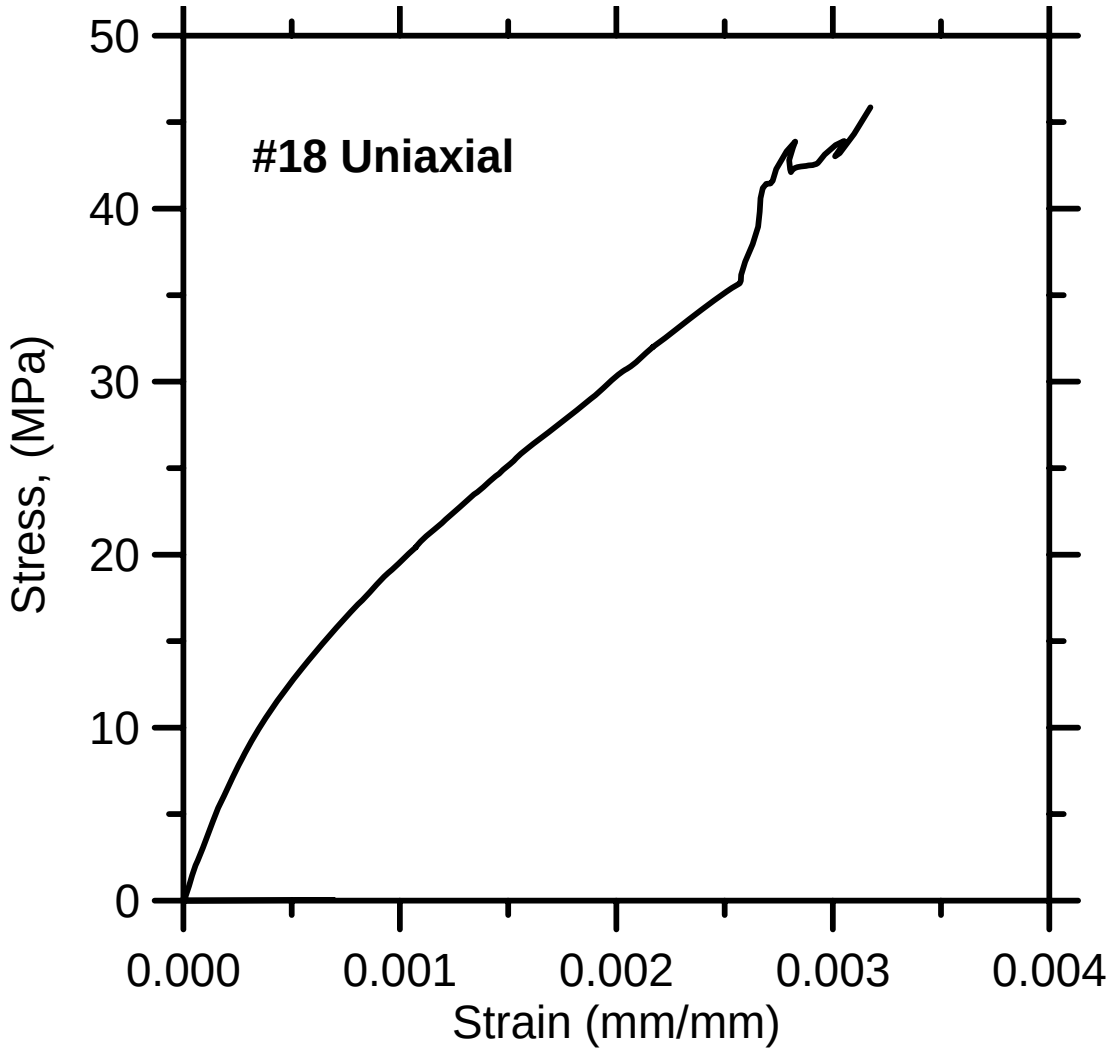
#18 Uniaxial
Stress, (MPa)
Strain (mm/mm)
0
10
20
30
40
50
0.000
0.001
0.002
0.003
0.004

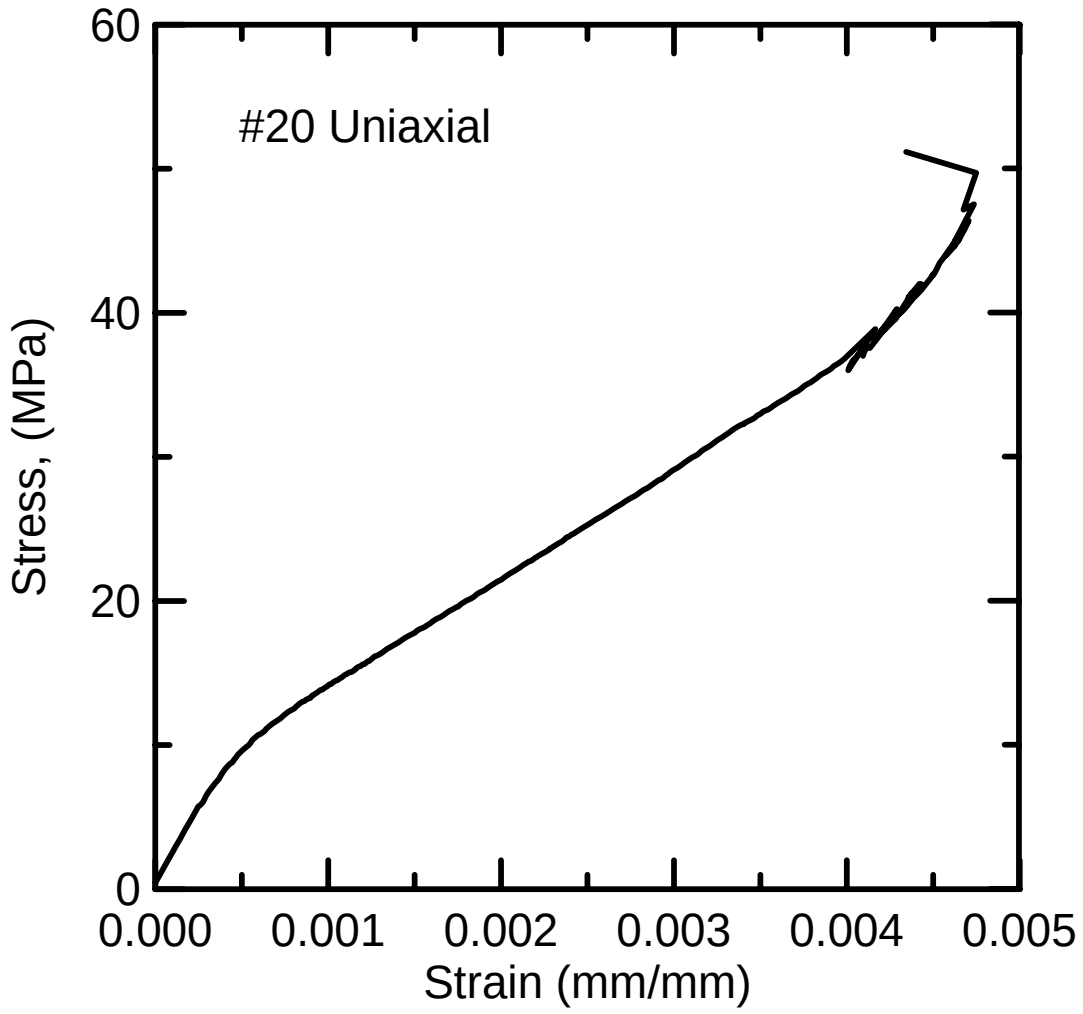
#20 Uniaxial
Stress, (MPa)
Strain (mm/mm)
0
20
40
60
0.000
0.001
0.002
0.003
0.004
0.005

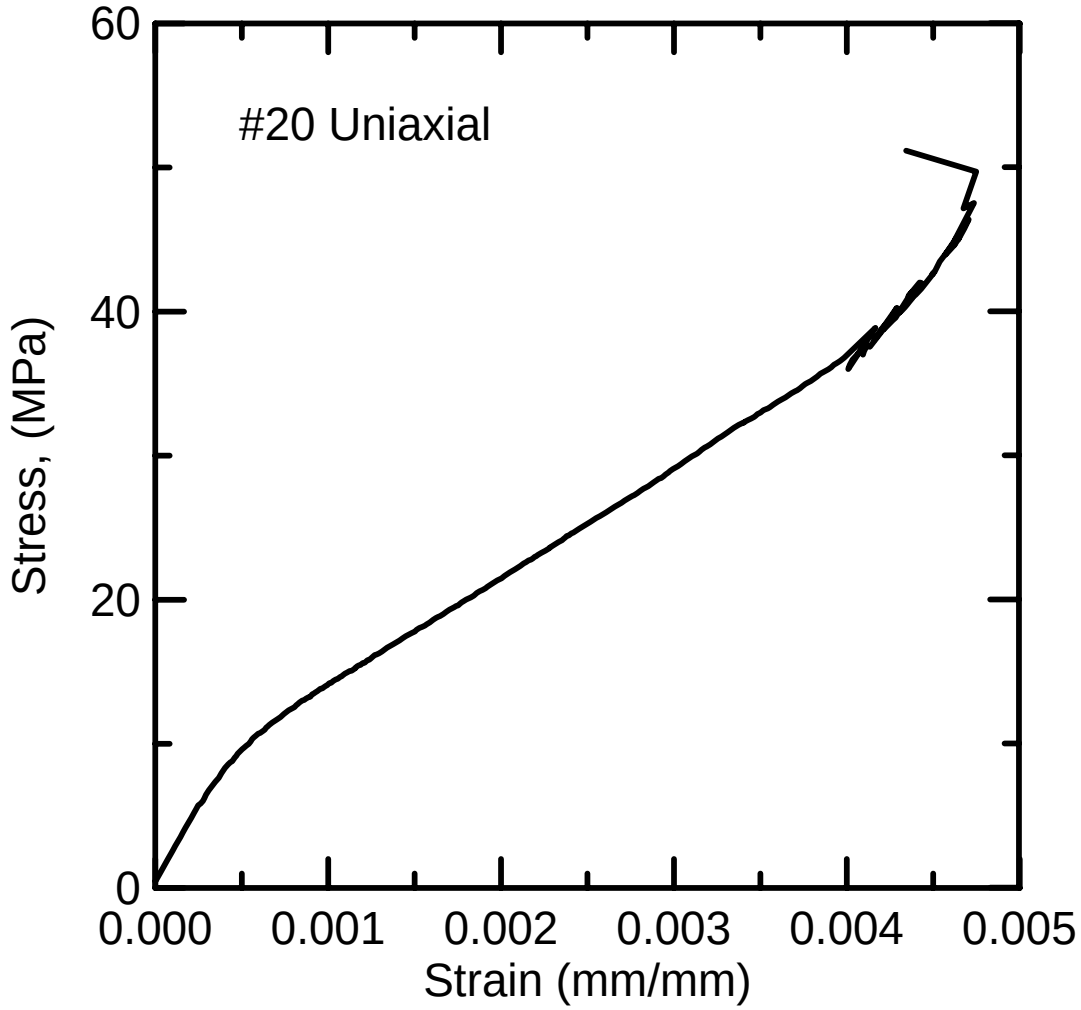
#20 Uniaxial
Stress, (MPa)
Strain (mm/mm)
0
20
40
60
0.000
0.001
0.002
0.003
0.004
0.005

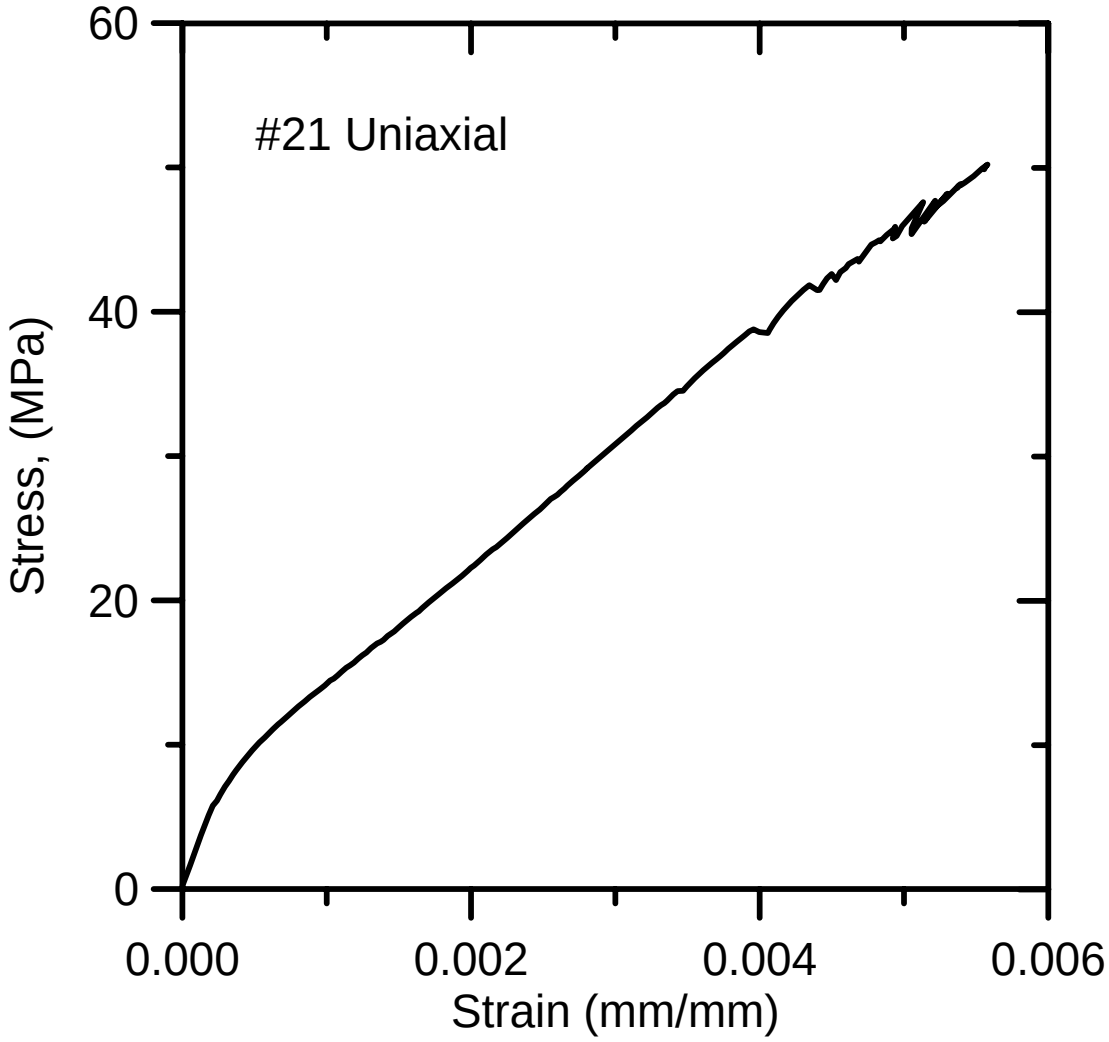
#21 Uniaxial
Stress, (MPa)
Strain (mm/mm)
0
20
40
60
0.000
0.002
0.004
0.006

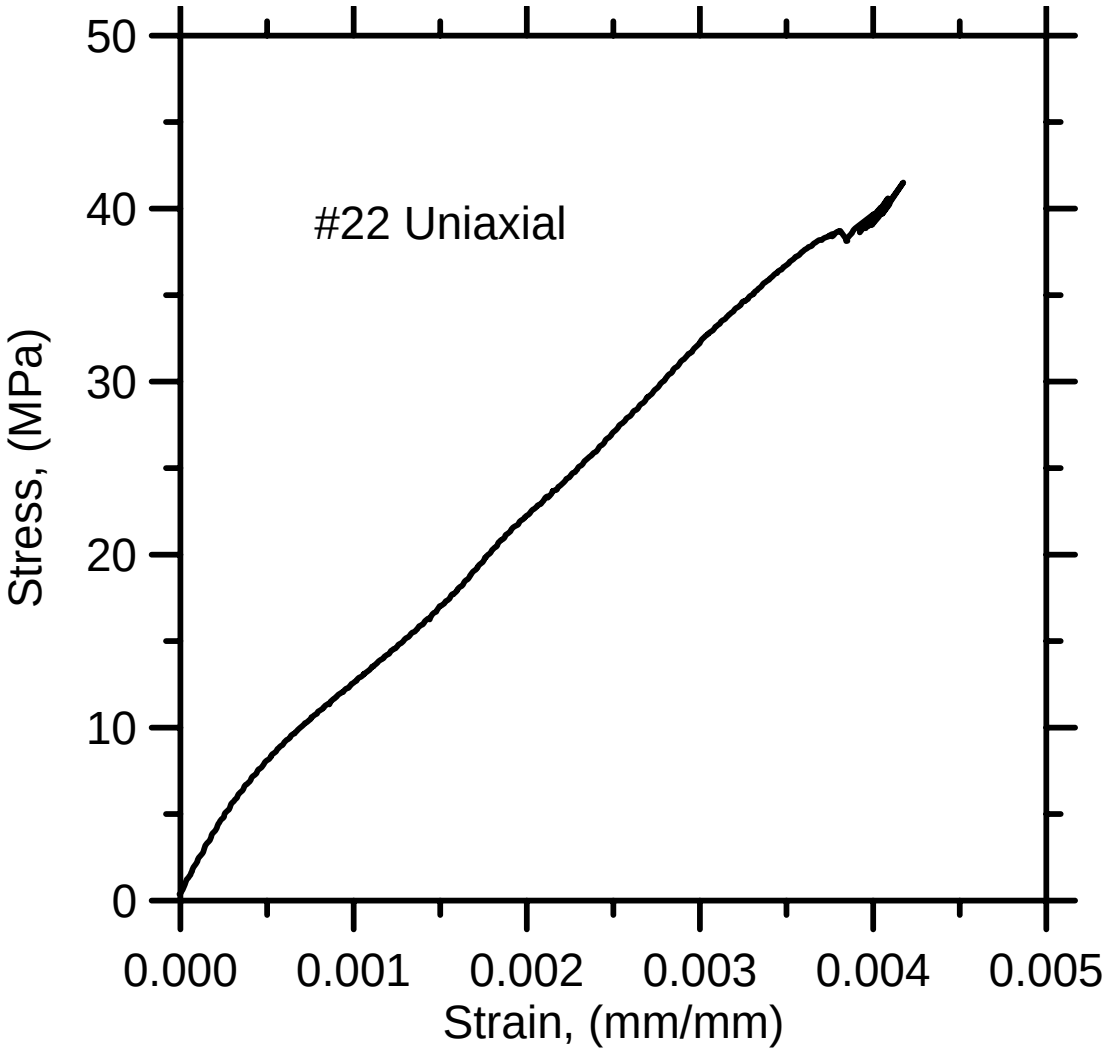
#22 Uniaxial
Stress, (MPa)
Strain, (mm/mm)
0
10
20
30
40
50
0.000
0.001
0.002
0.003
0.004
0.005

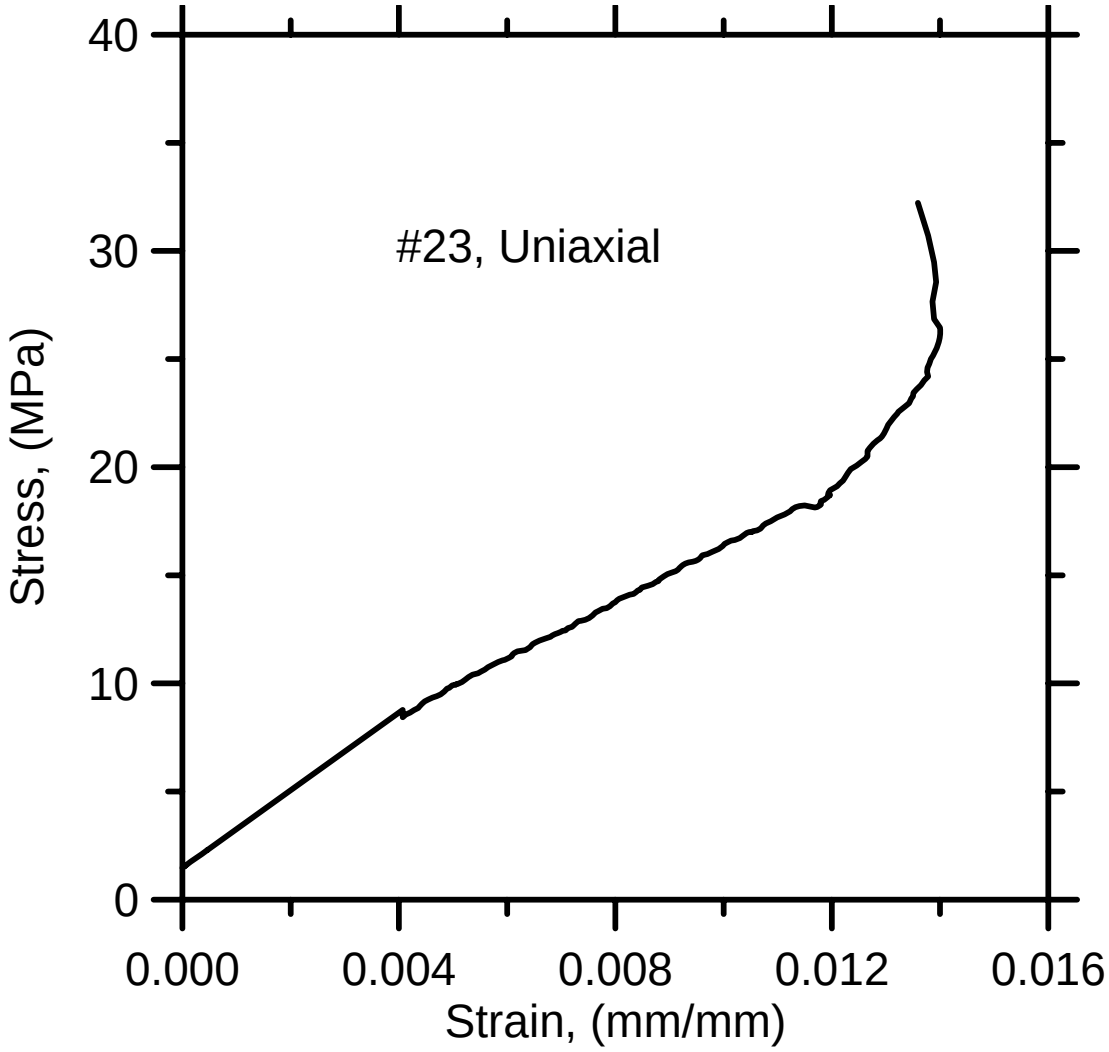
#23, Uniaxial
Stress, (MPa)
Strain, (mm/mm)
0
10
20
30
40
0.000
0.004
0.008
0.012
0.016

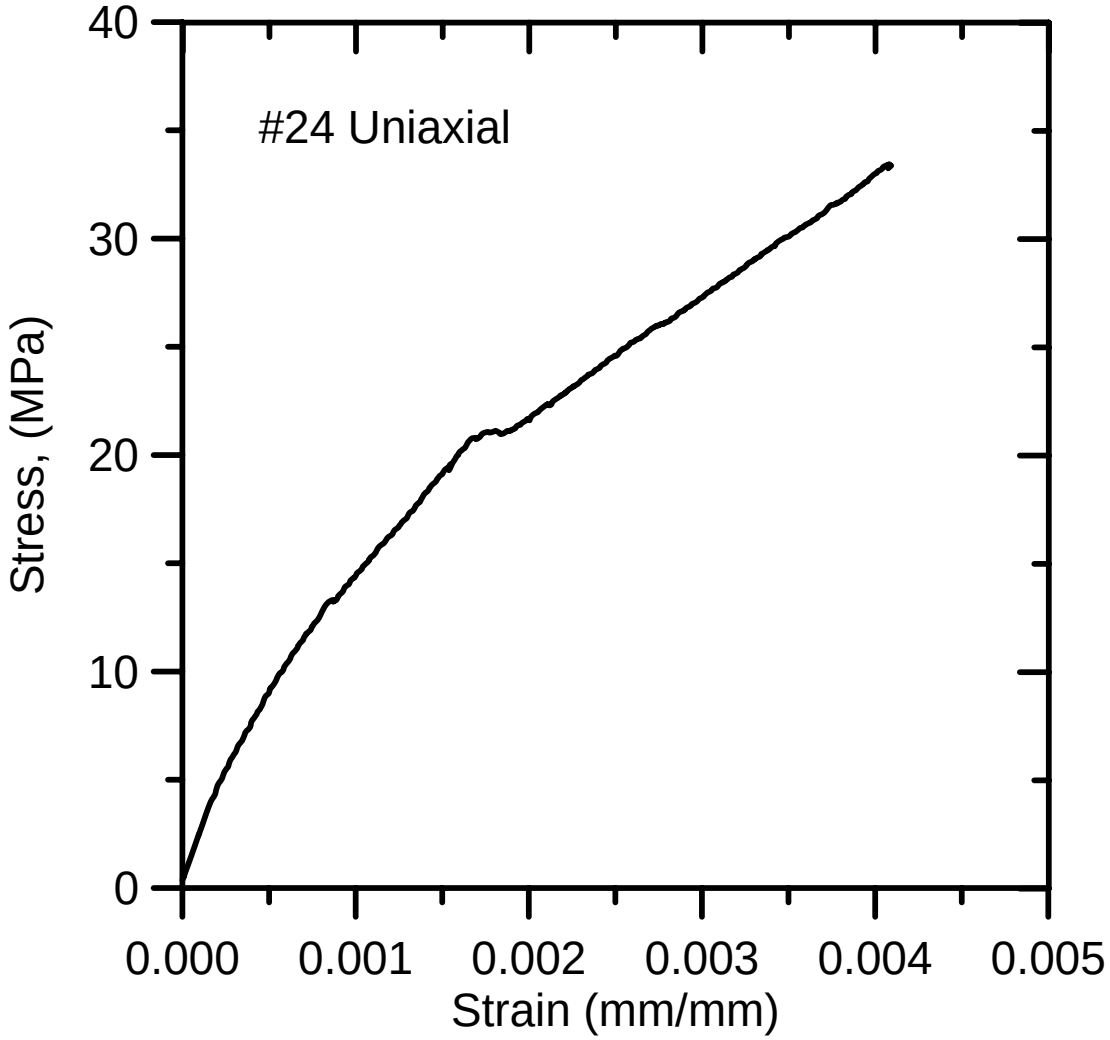
#24 Uniaxial
Stress, (MPa)
Strain (mm/mm)
0
10
20
30
40
0.000
0.001
0.002
0.003
0.004
0.005

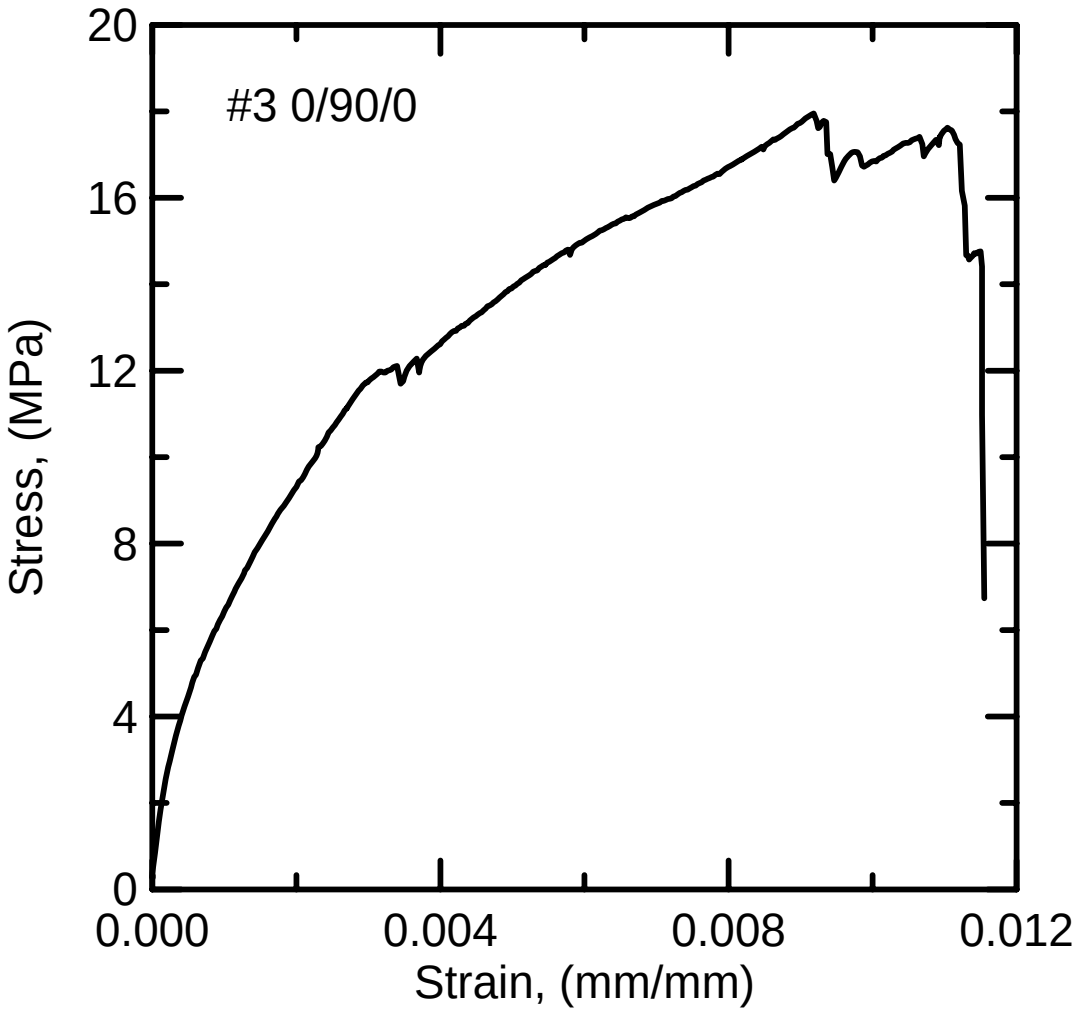
#3 0/90/0
Stress, (MPa)
Strain, (mm/mm)
0
4
8
12
16
20
0.000
0.004
0.008
0.012

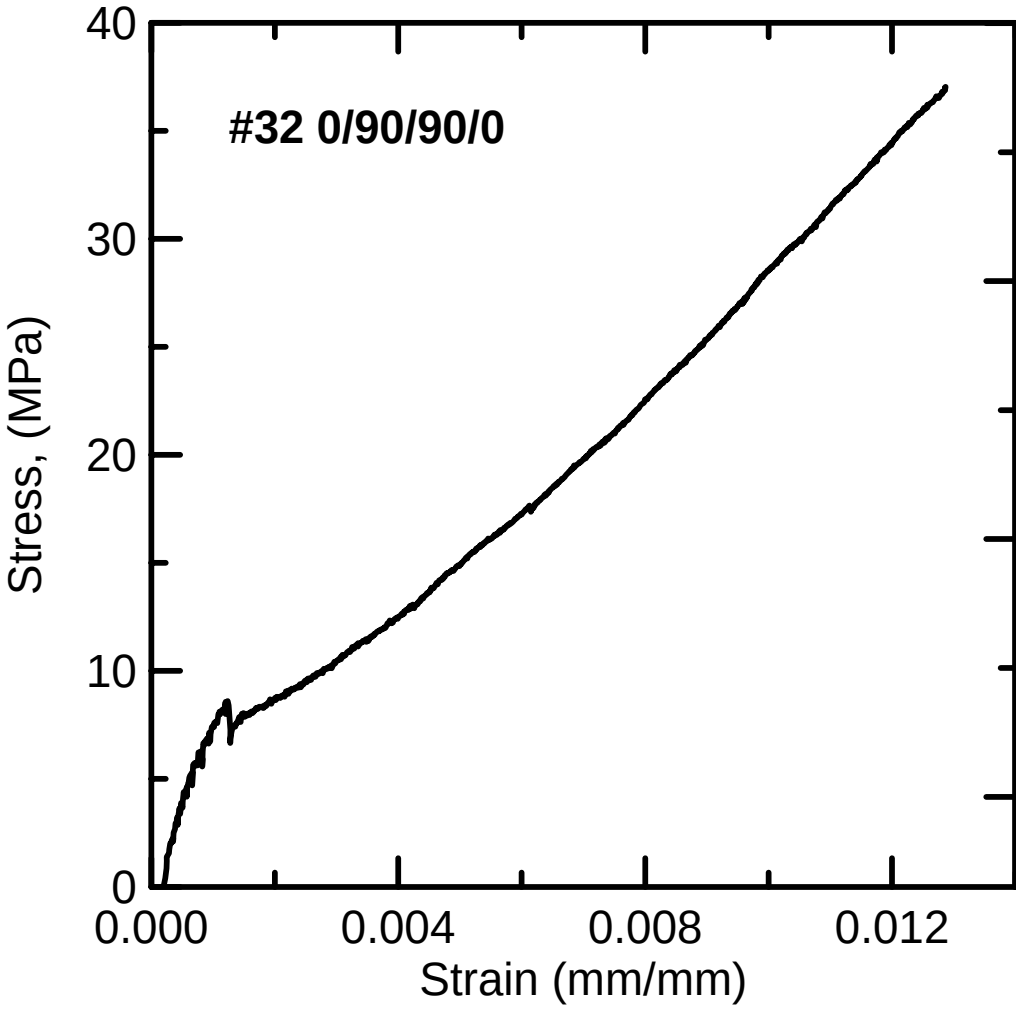
#32 0/90/90/0
Stress, (MPa)
Strain (mm/mm)
0
10
20
30
40
0.000
0.004
0.008
0.012

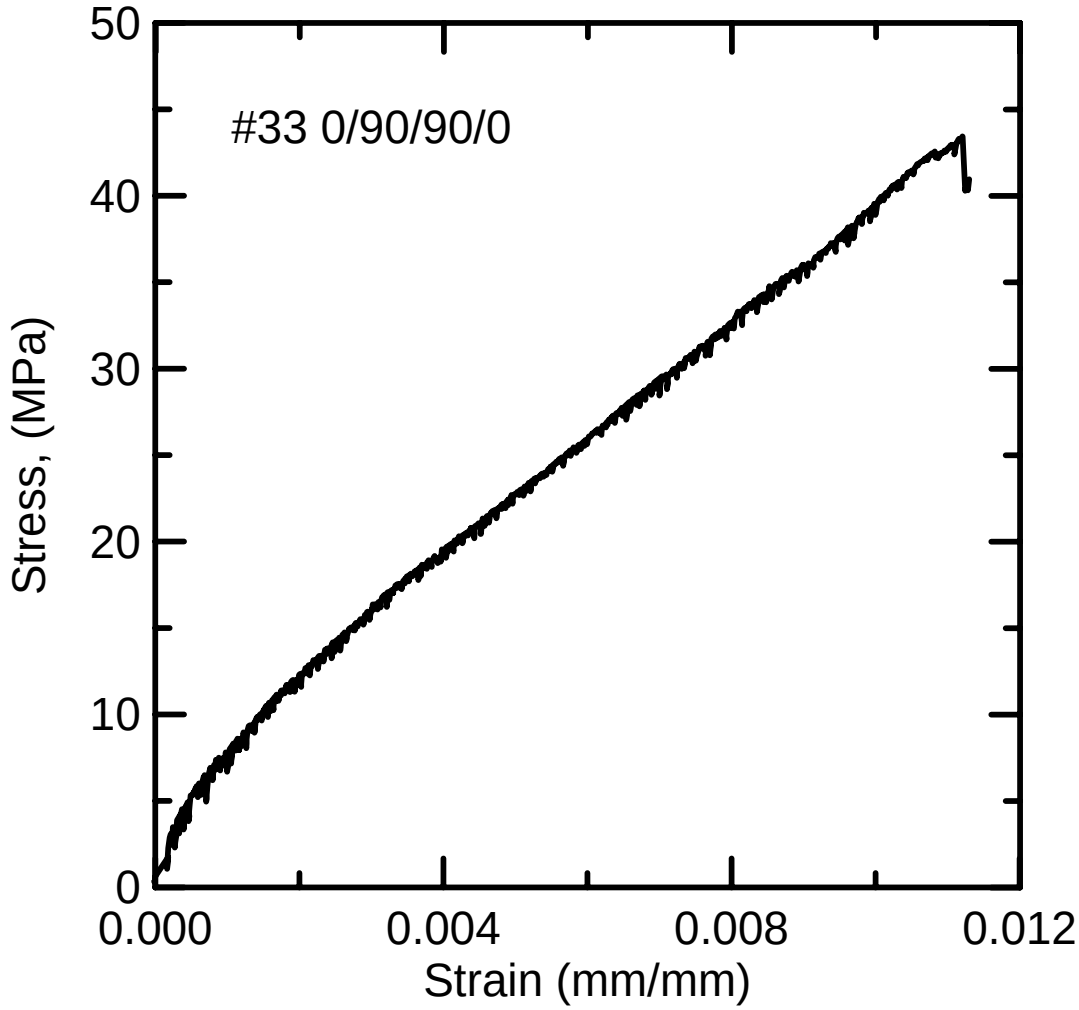
#33 0/90/90/0
Stress, (MPa)
Strain (mm/mm)
0
10
20
30
40
50
0.000
0.004
0.008
0.012

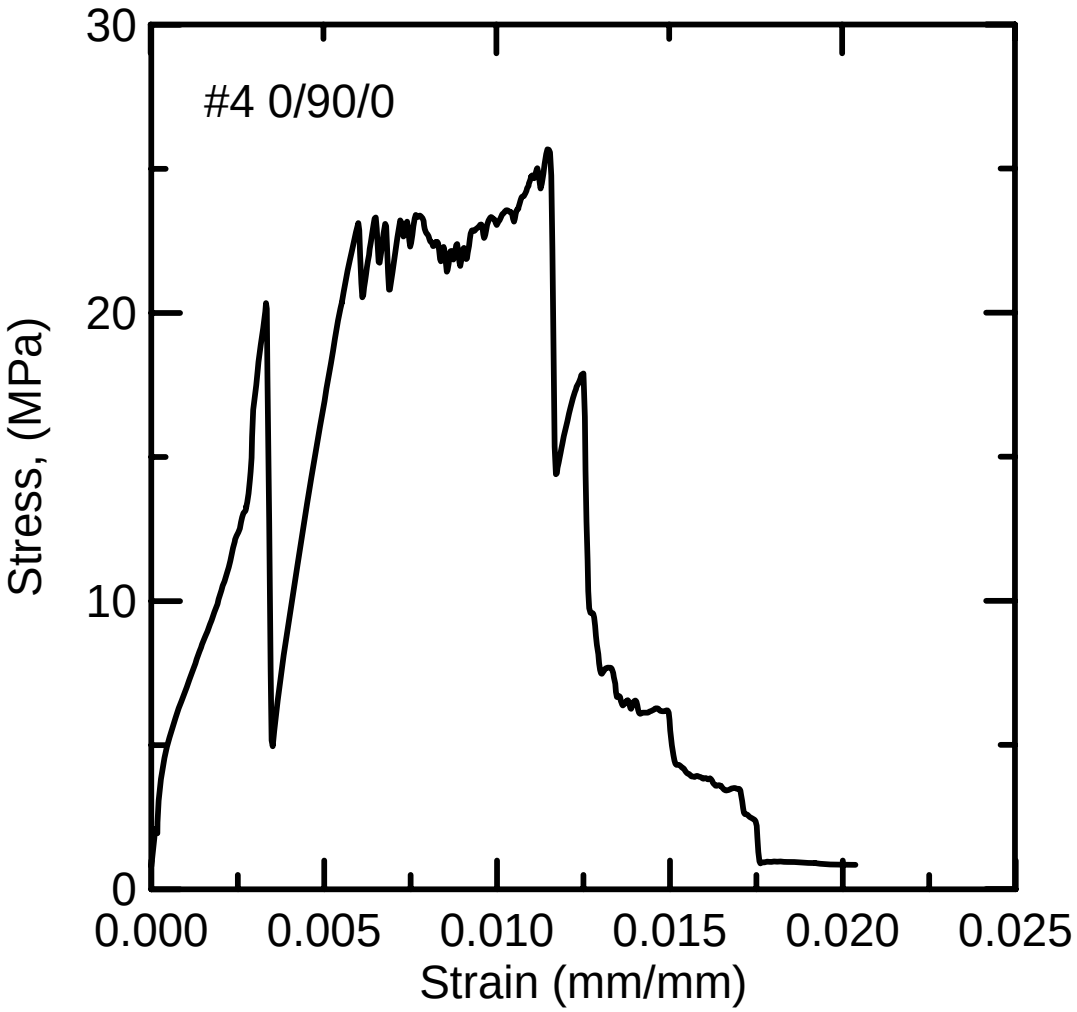
#4 0/90/0
Stress, (MPa)
Strain (mm/mm)
0
10
20
30
0.000
0.005
0.010
0.015
0.020
0.025

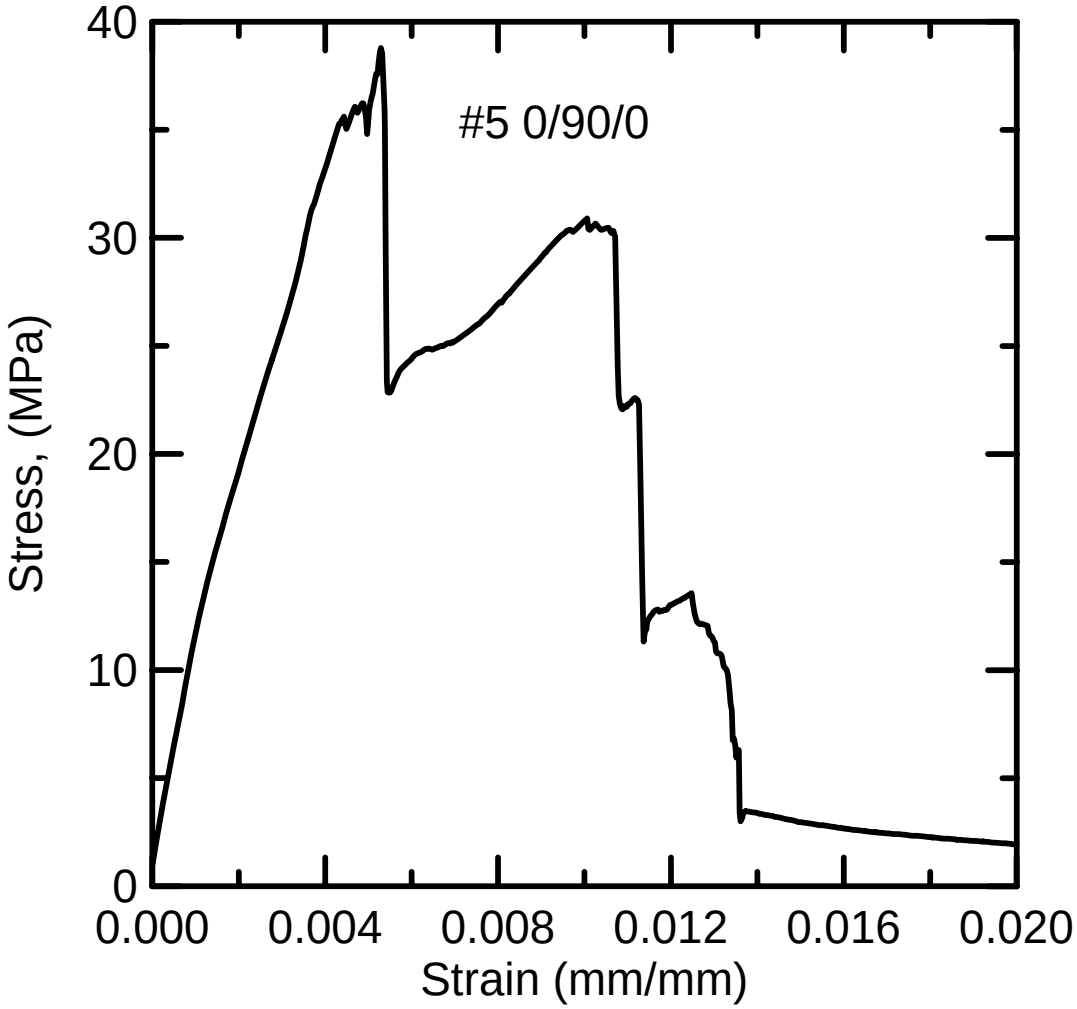
#5 0/90/0
Stress, (MPa)
Strain (mm/mm)
0
10
20
30
40
0.000
0.004
0.008
0.012
0.016
0.020

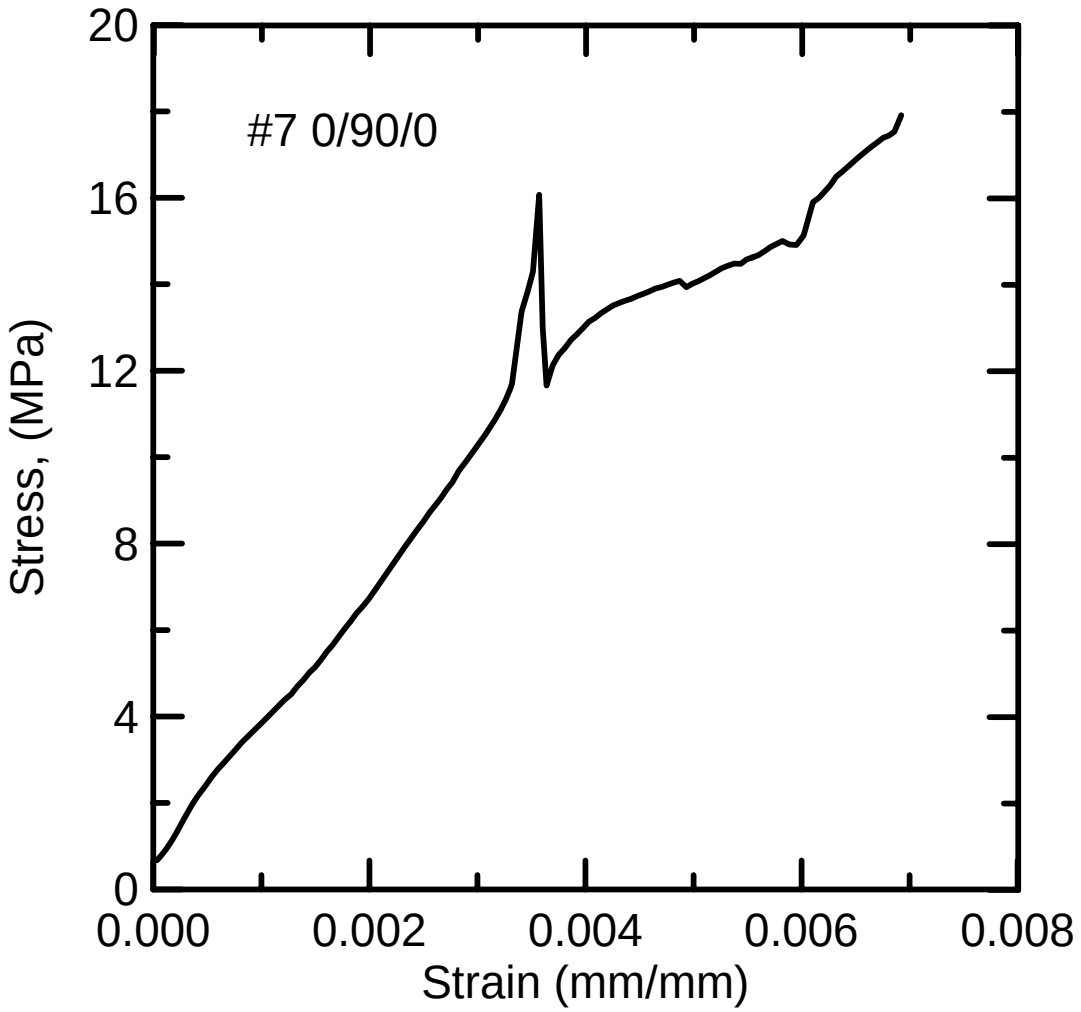
#7 0/90/0
Stress, (MPa)
Strain (mm/mm)
0
4
8
12
16
20
0.000
0.002
0.004
0.006
0.008

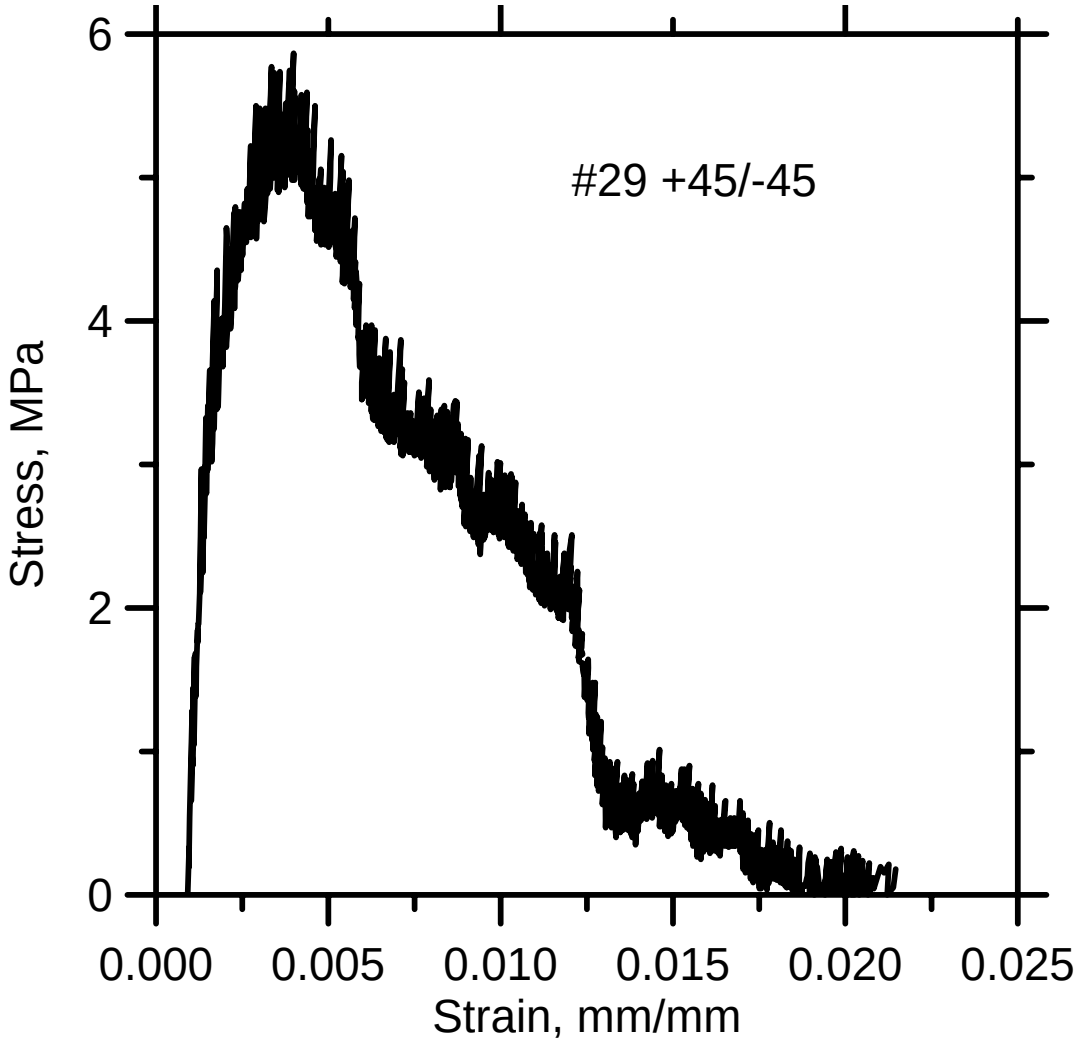
#29 +45/-45
Stress, MPa
Strain, mm/mm
0
2
4
6
0.000
0.005
0.010
0.015
0.020
0.025

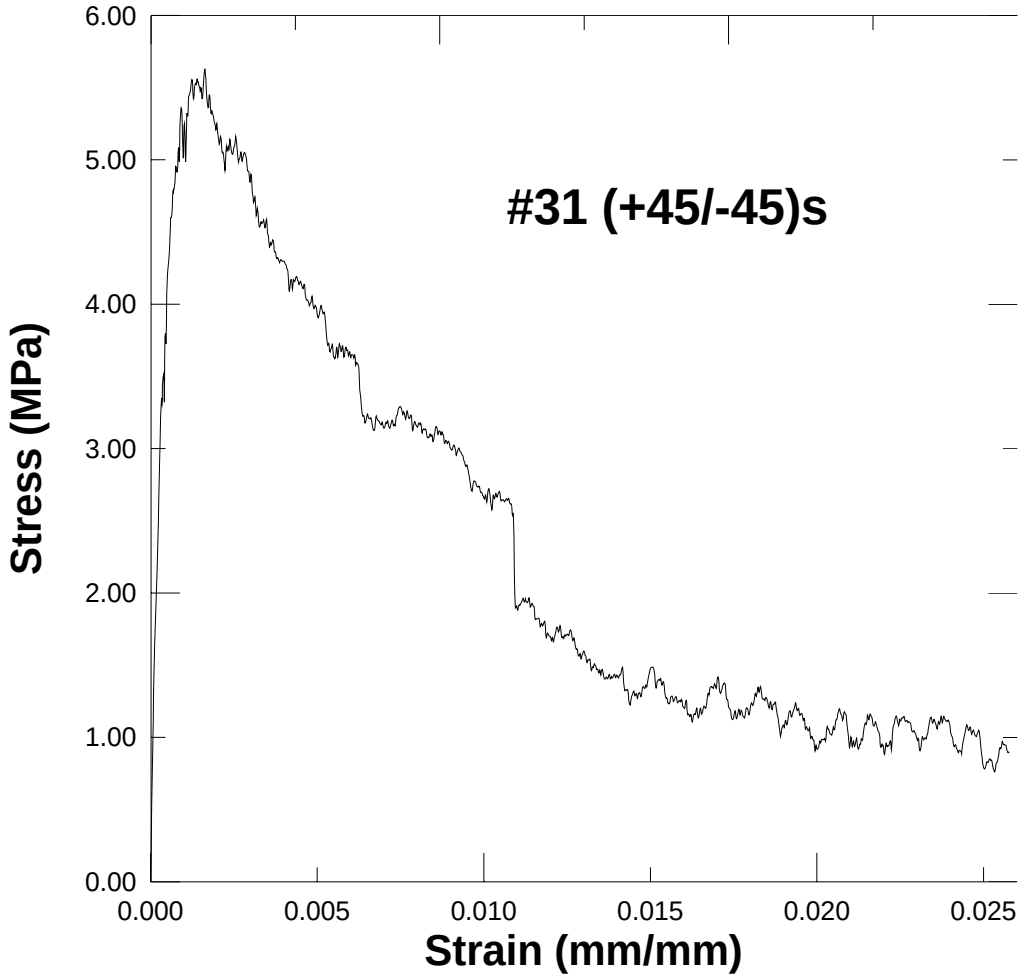
#31 (+45/-45)s
Stress (MPa)
Strain (mm/mm)
6.00
5.00
4.00
3.00
2.00
1.00
0.00
0.000
0.005
0.010
0.015
0.020
0.025

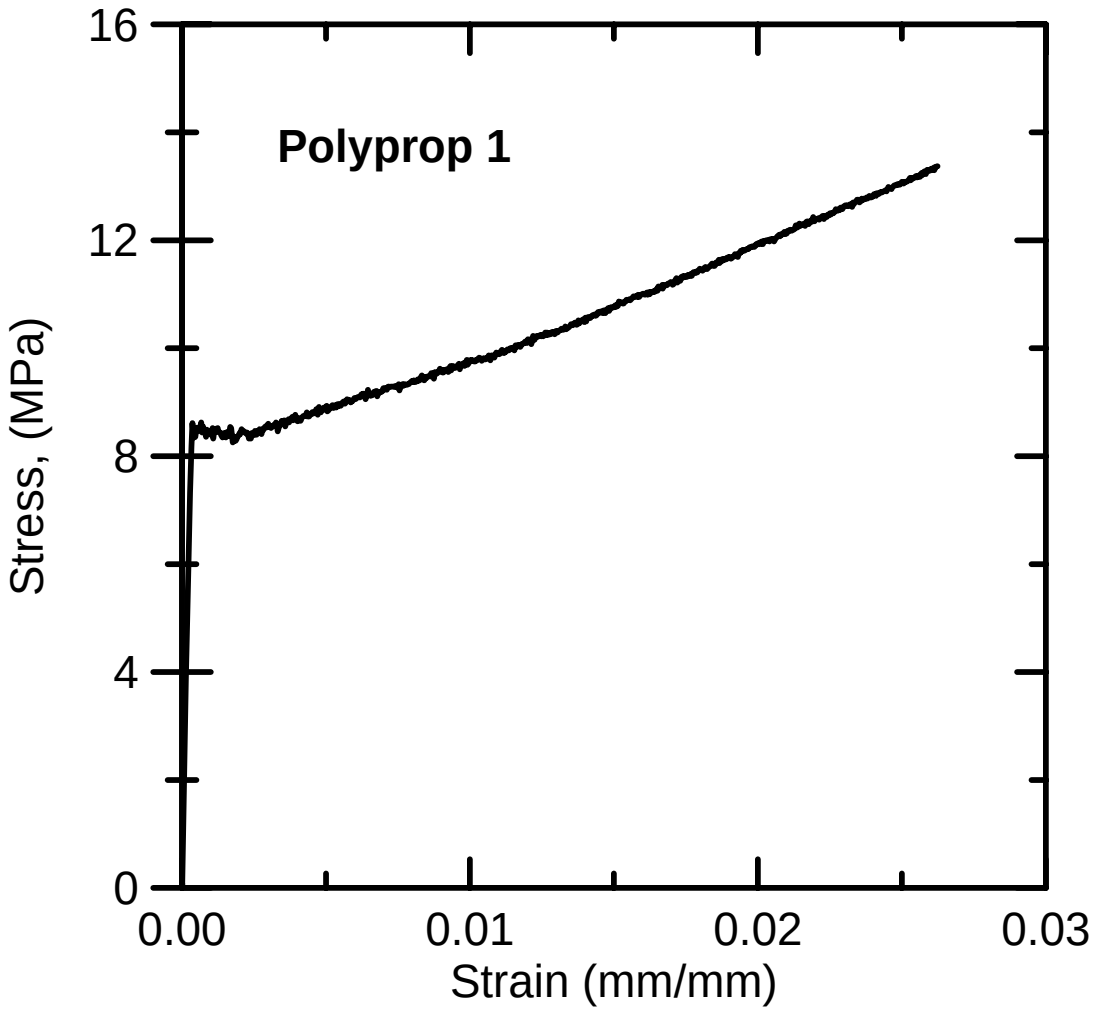
Polyprop 1
Stress, (MPa)
16
12
8
4
0
0.00
0.01
0.02
0.03
Strain (mm/mm)

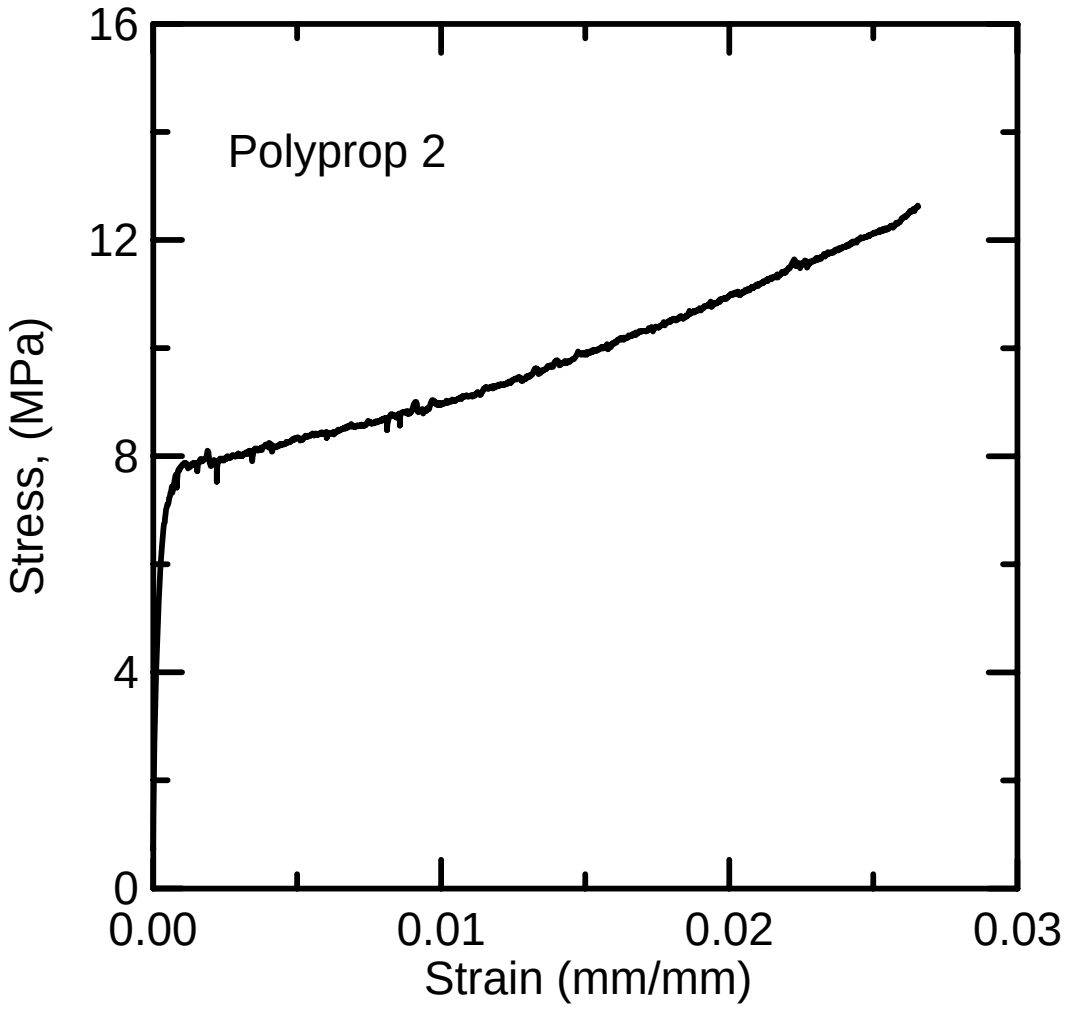
Polyprop 2
Stress, (MPa)
Strain (mm/mm)
0
4
8
12
16
0.00
0.01
0.02
0.03

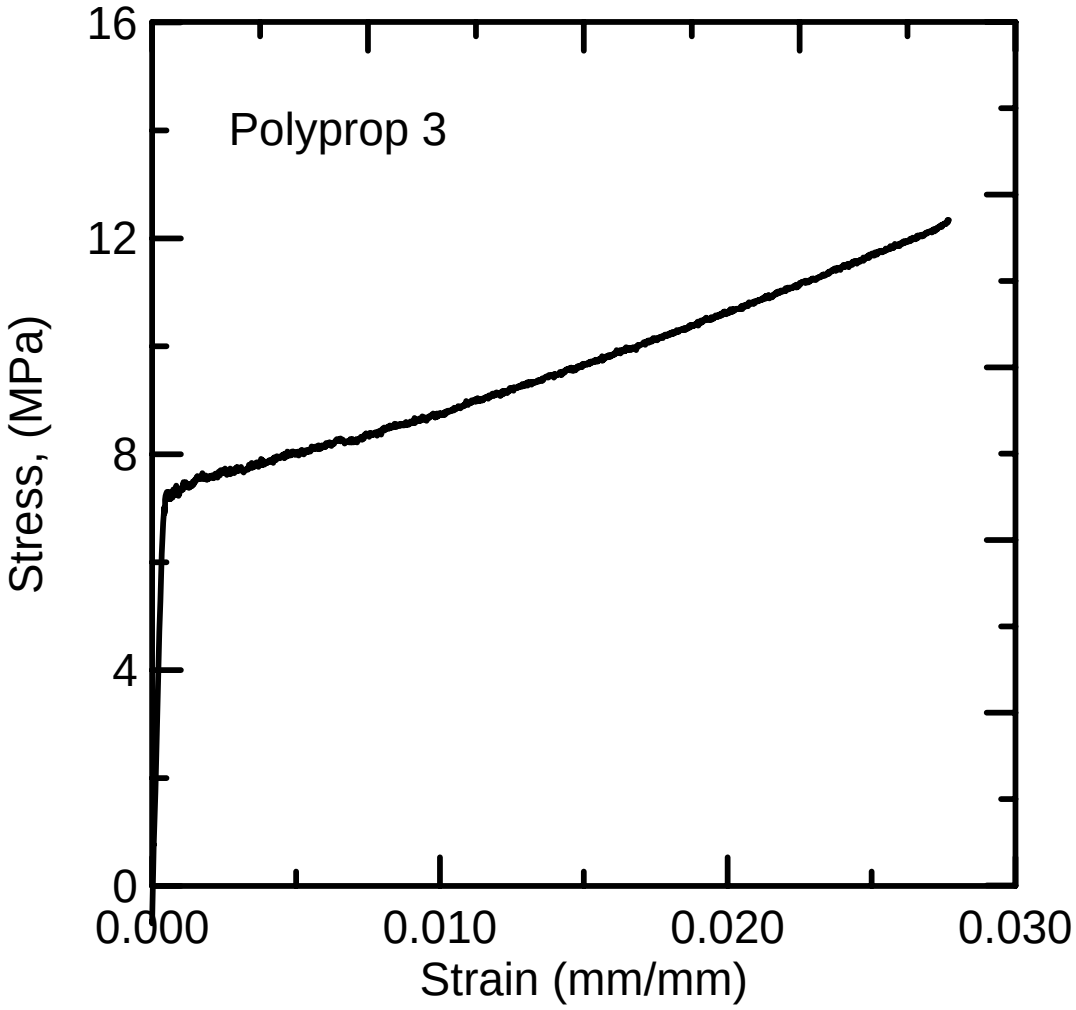
Polyprop 3
Stress, (MPa)
Strain (mm/mm)
0
4
8
12
16
0.000
0.010
0.020
0.030

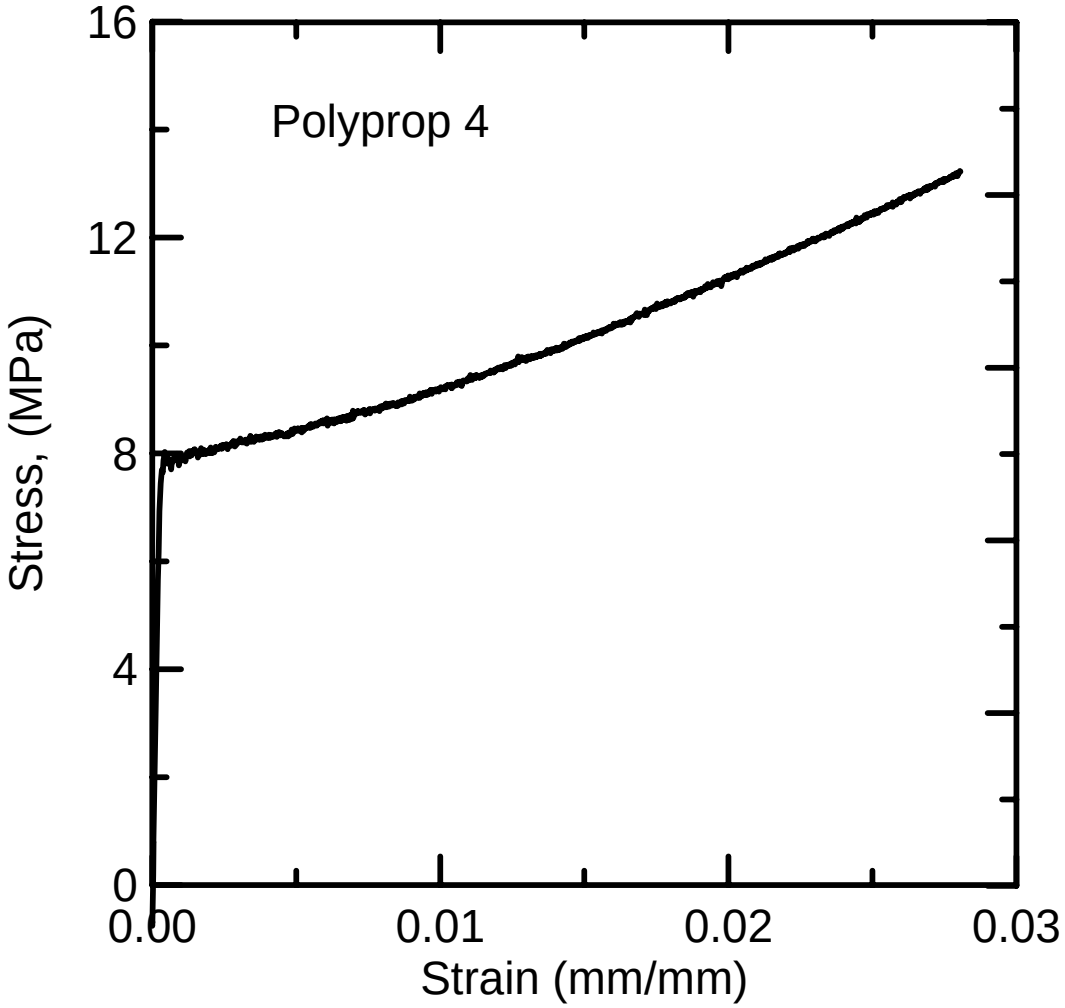
Polyprop 4
Stress, (MPa)
Strain (mm/mm)
16
12
8
4
0
0.00
0.01
0.02
0.03

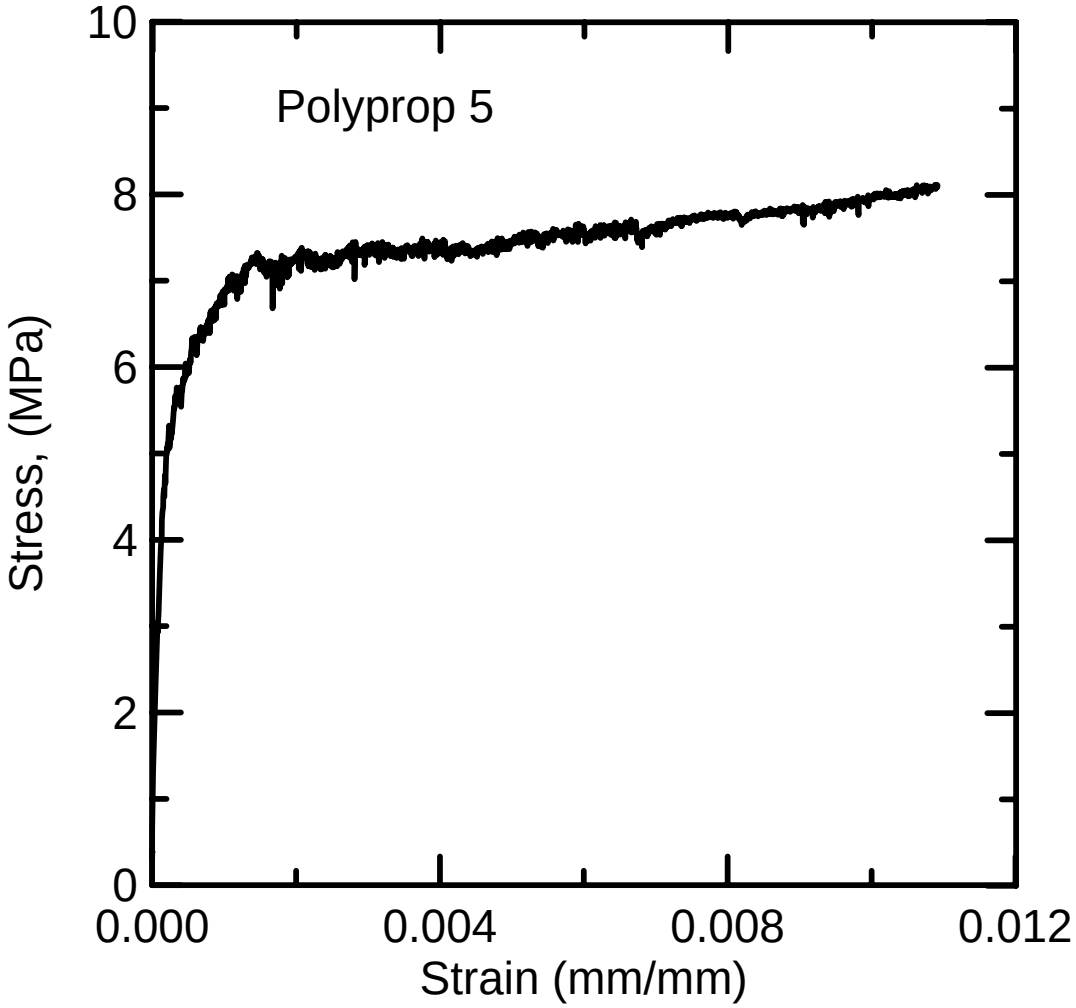
Polyprop 5
Stress, (MPa)
Strain (mm/mm)
0
2
4
6
8
10
0.000
0.004
0.008
0.012

APPENDIX D

Flexural Test Results

Table D.1 Flexural Test Results

	FLEXURE			AR-Glass					Toughness	
	E	MOR	MOR	PEL	PEL	LOP	LOP	end	Normalized	
Specimen	MPa	Stress	Deflect	Stress	Deflect	Stress	Deflect	Deflect	MOR	Test
0/0/0		MPa	mm	MPa	mm	MPa	mm	mm	N/mm	N/mm
1u*	8.11	25.87		6.75	0.70			4.77	4.41	
2u*	10.25	25.48		5.00	0.40			3.84	2.19	
3u*	12.16	28.08		4.50	0.98			4.37	2.93	
4u	18.41	56.27	5.62	12.00	1.50	56.27	5.62	25.67	13.94	42.31
5u*	18.63	38.78		4.50	0.30			3.41	4.08	
5au	12.51	58.20	7.27	22.00	1.90	58.20	7.27	18.92	17.12	27.88
11u	18.01	47.00	4.18	13.00	1.20	47.00	4.18	31.82	9.45	53.88
12u	17.66	52.40	3.60	13.50	0.95	52.40	3.60	23.74	9.78	53.40
13u	15.05	40.24	9.66	12.00	0.90	37.20	5.30	28.95	22.68	53.28
14u	19.80	55.25	4.06	17.00	0.90	55.25	4.06	20.20	9.58	42.42
15u	18.50	34.40	2.30	11.00	0.60	34.40	2.30	29.23	5.45	45.65
x2cr	14.07	54.50	6.22	12.50	2.21	44.90	4.55	21.57	12.98	40.41
average	16.75	49.78	5.36	11.15	1.05	48.20	4.61	25.01	12.62	44.90
stdev	2.55	8.51	2.34	5.31	.58	8.91	1.48	4.69	5.37	8.84
Tests 1-3, 5, and x1 were not carried to										
so not included in ultimate calculations just										
0/90/90/0										
6cr	17.04	29.84	14.38	10.00	0.65	29.10	4.10	22.29	21.59	33.34
7cr	17.15	19.92	3.43	15.00	0.55	19.30	2.80	19.73	4.13	11.93
8cr	13.40	18.80	15.69	7.20	0.65	11.90	2.05	34.11	12.59	29.85
9cr	39.01	21.16	12.70	19.50	0.65	19.50	0.65	33.80	13.82	31.74
10cr	36.49	24.42	17.18	25.00	0.77	24.42	0.77	33.45	20.31	34.43
x1cr*	13.85	25.27	4.86	6.15	0.47	20.05	1.80	ultimate	8.08	
average	22.82	23.24	11.37	13.81	.62	20.71	2.03	28.68	13.42	28.26
stdev	11.69	4.10	5.81	7.43	.10	5.76	1.30	7.06	6.78	9.29

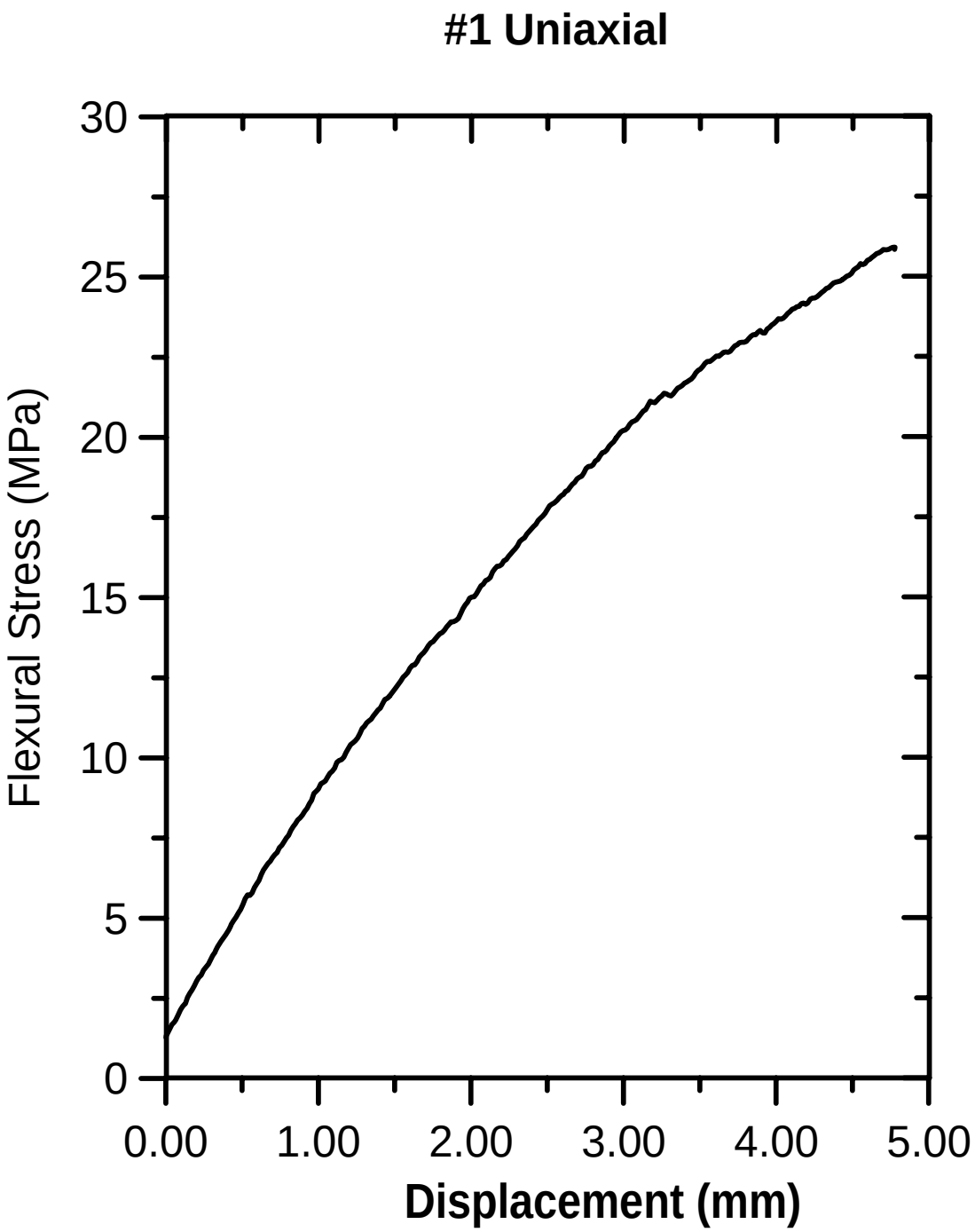
#1 Uniaxial
Flexural Stress (MPa)
30
25
20
15
10
5
0
0.00
1.00
2.00
3.00
4.00
5.00
Displacement (mm)

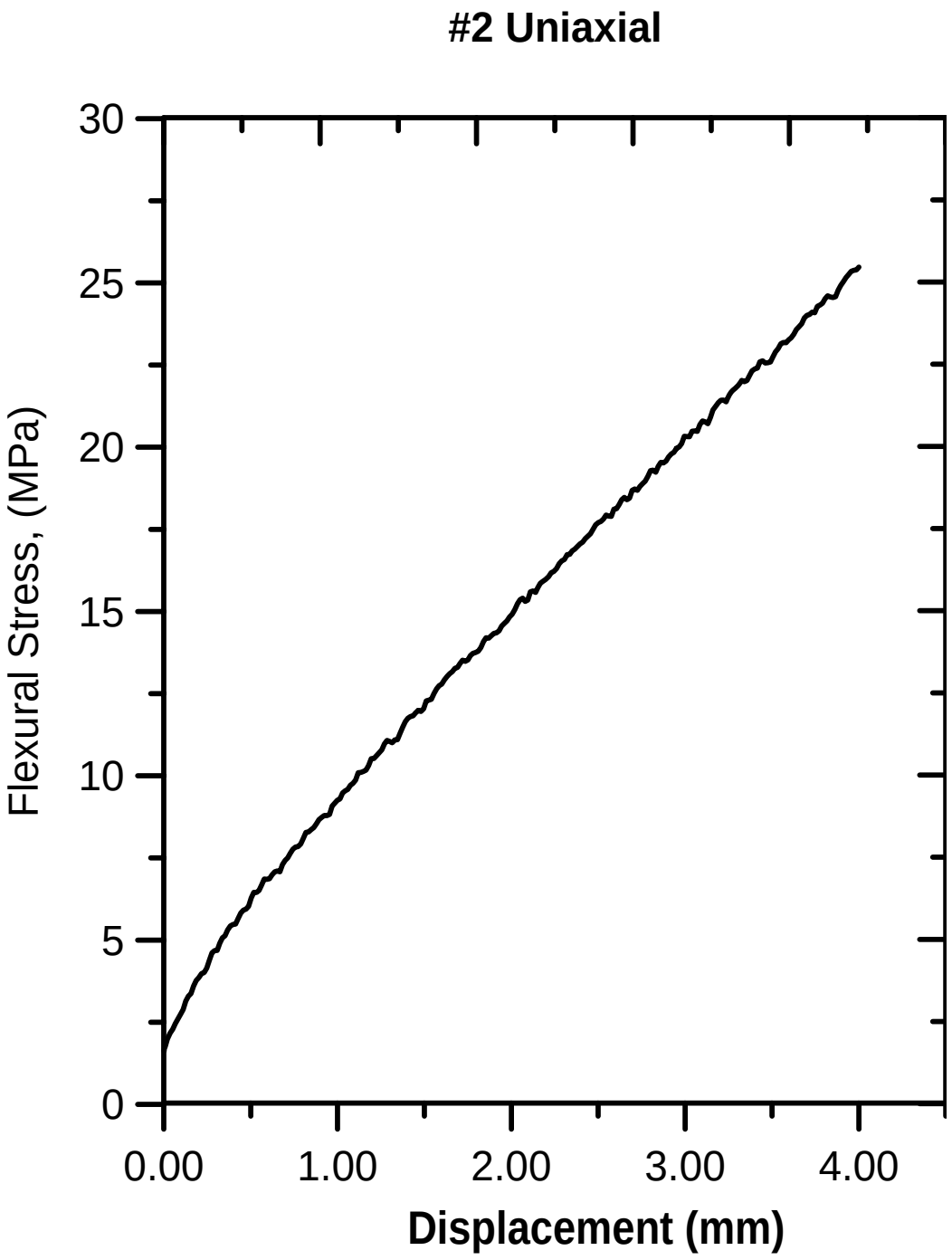
#2 Uniaxial
Flexural Stress, (MPa)
30
25
20
15
10
5
0
0.00
1.00
2.00
3.00
4.00
Displacement (mm)

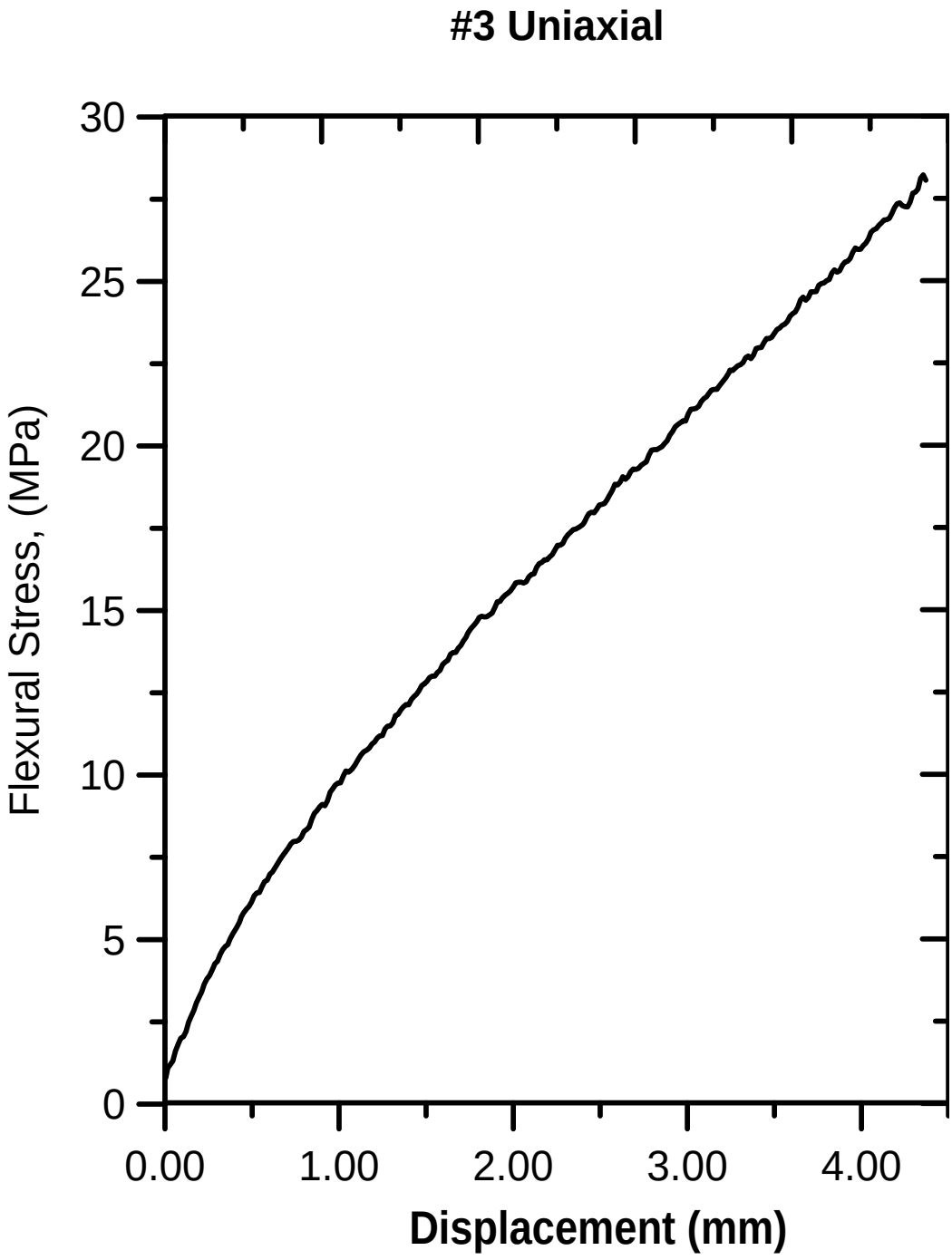
#3 Uniaxial
Flexural Stress, (MPa)
30
25
20
15
10
5
0
0.00
1.00
2.00
3.00
4.00
Displacement (mm)

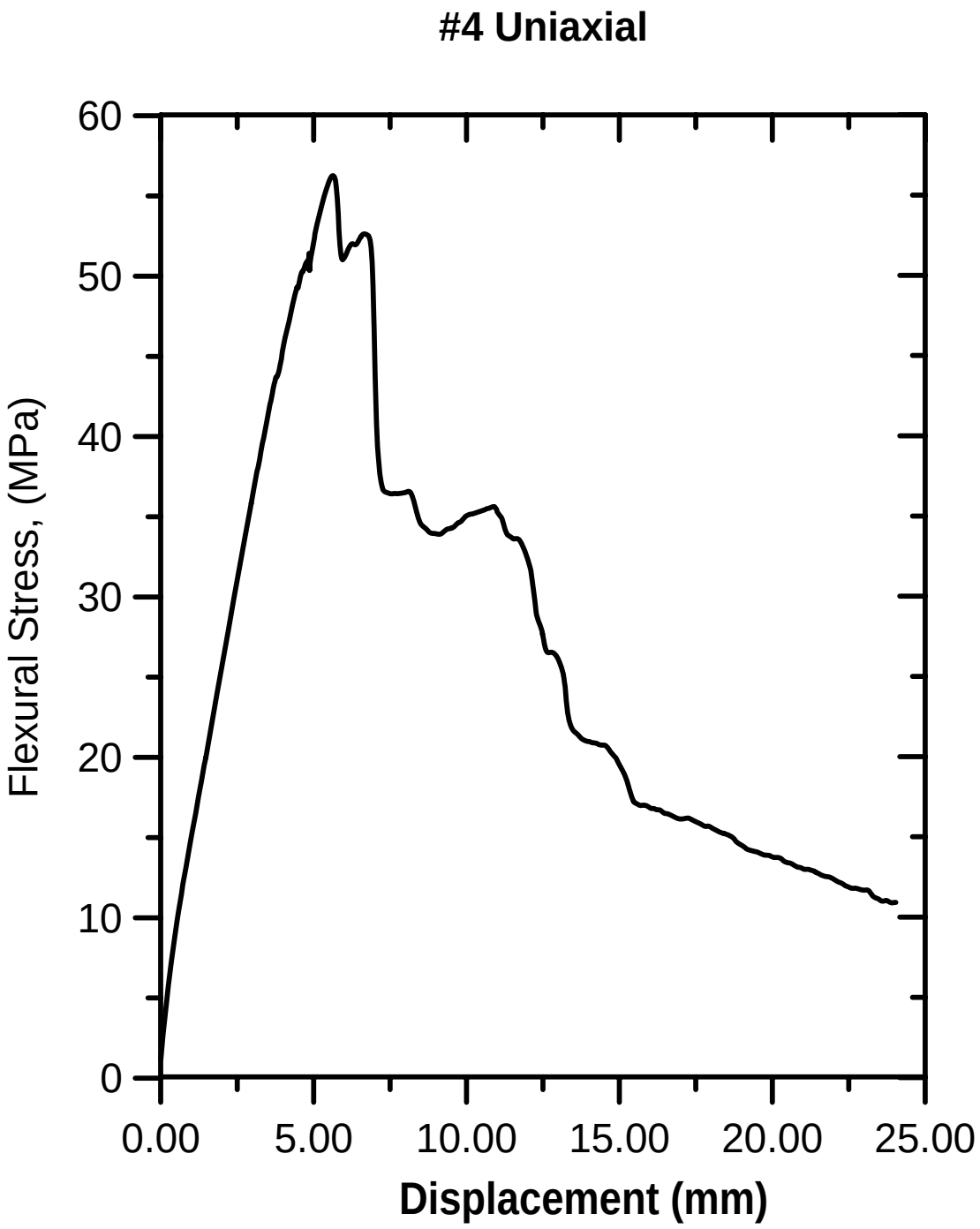
#4 Uniaxial
Flexural Stress, (MPa)
60
50
40
30
20
10
0
0.00
5.00
10.00
15.00
20.00
25.00
Displacement (mm)

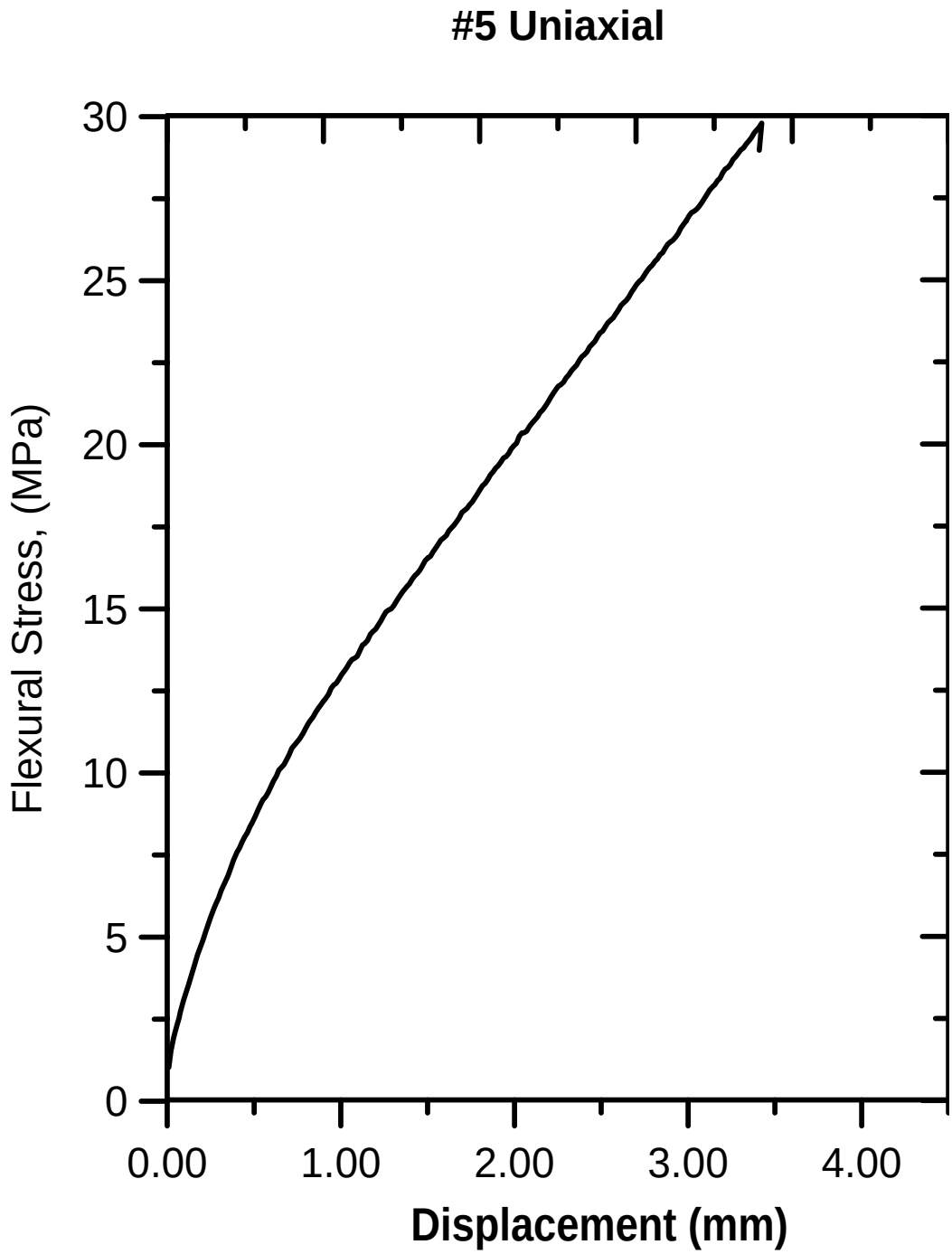
#5 Uniaxial
Flexural Stress, (MPa)
30
25
20
15
10
5
0
0.00
1.00
2.00
3.00
4.00
Displacement (mm)

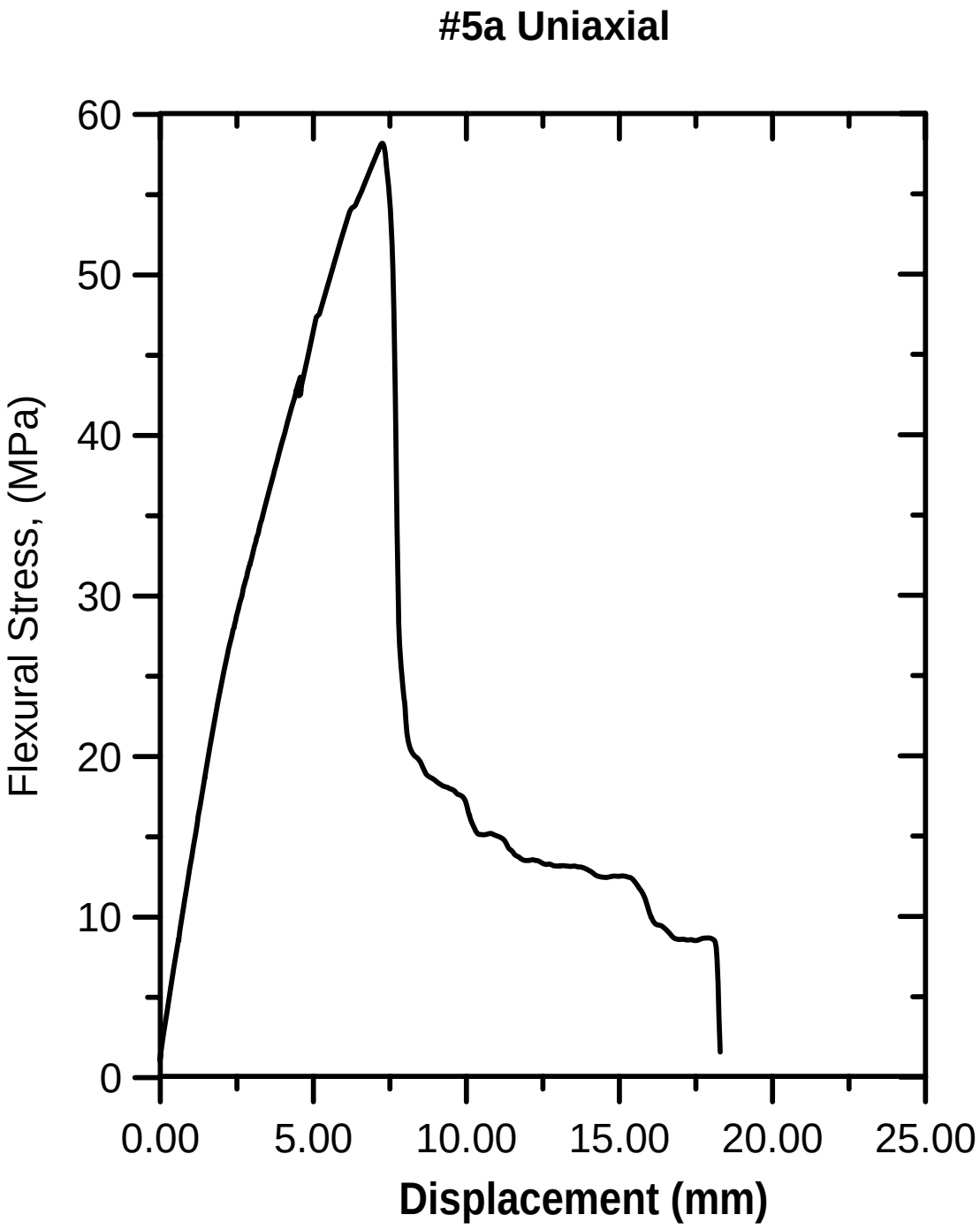
#5a Uniaxial
Flexural Stress, (MPa)
60
50
40
30
20
10
0
0.00
5.00
10.00
15.00
20.00
25.00
Displacement (mm)

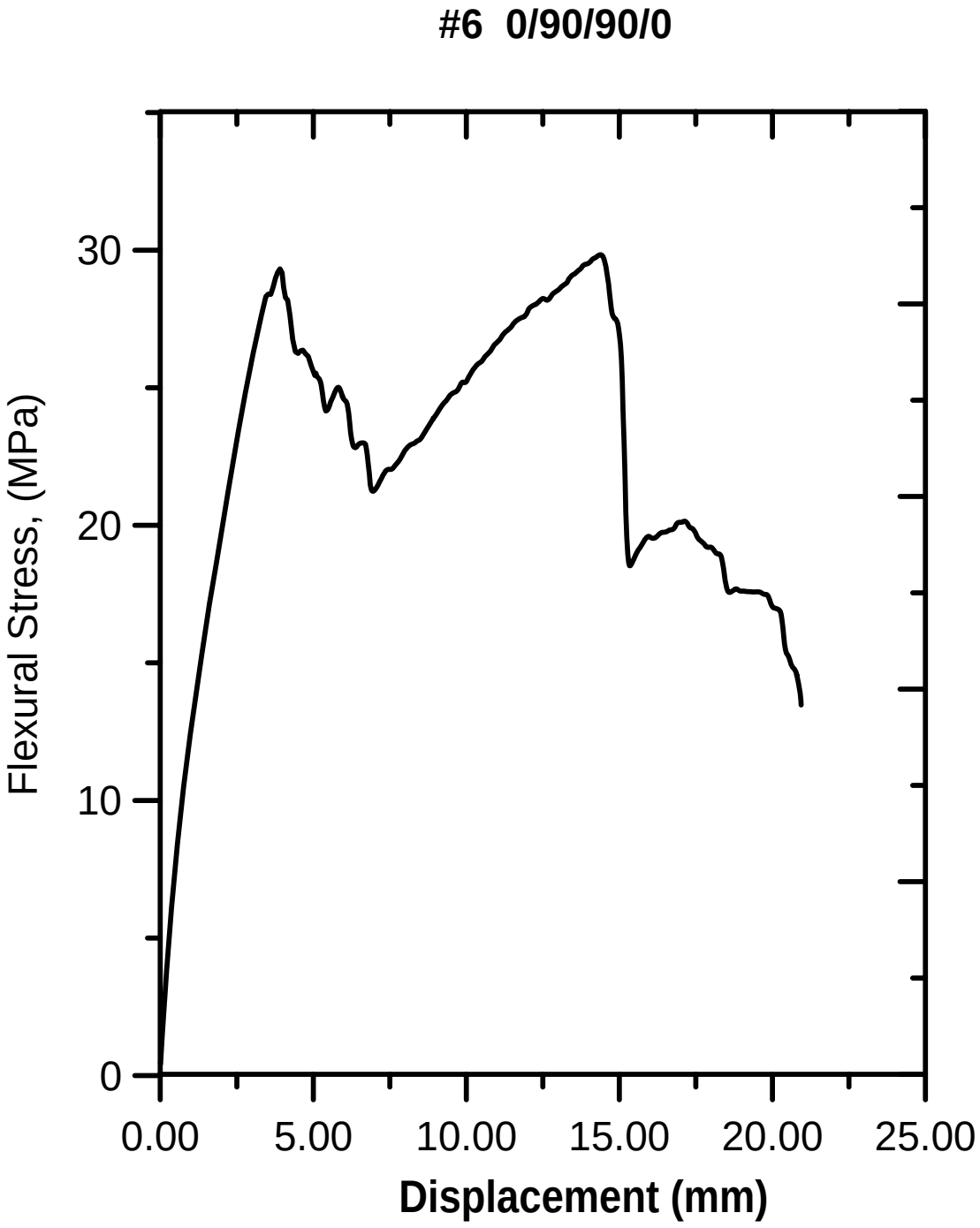
#6 0/90/90/0
Flexural Stress, (MPa)
0
10
20
30
0.00
5.00
10.00
15.00
20.00
25.00
Displacement (mm)

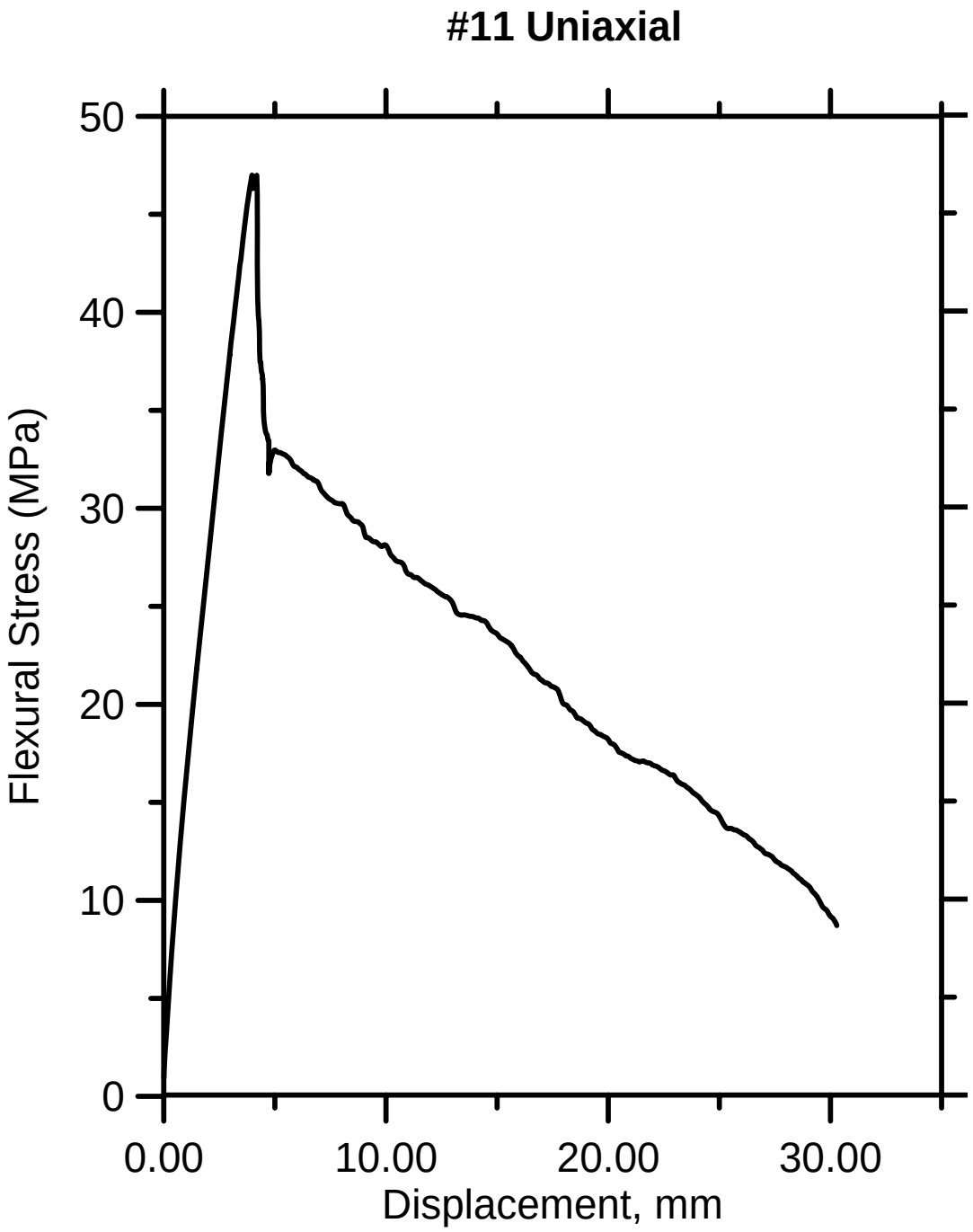
#11 Uniaxial
Flexural Stress (MPa)
50
40
30
20
10
0
0.00
10.00
20.00
30.00
Displacement, mm

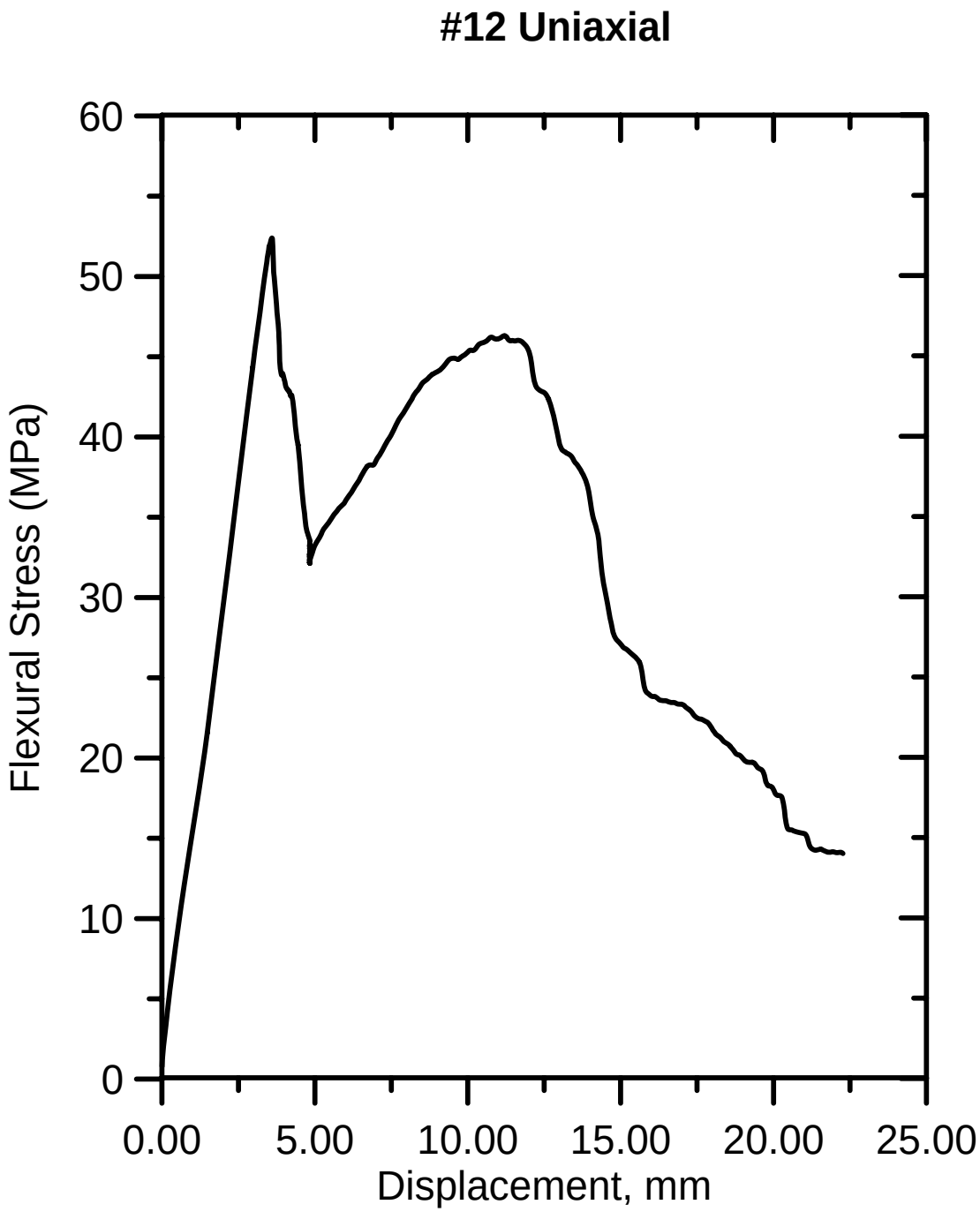
#12 Uniaxial
Flexural Stress (MPa)
60
50
40
30
20
10
0
0.00
5.00
10.00
15.00
20.00
25.00
Displacement, mm

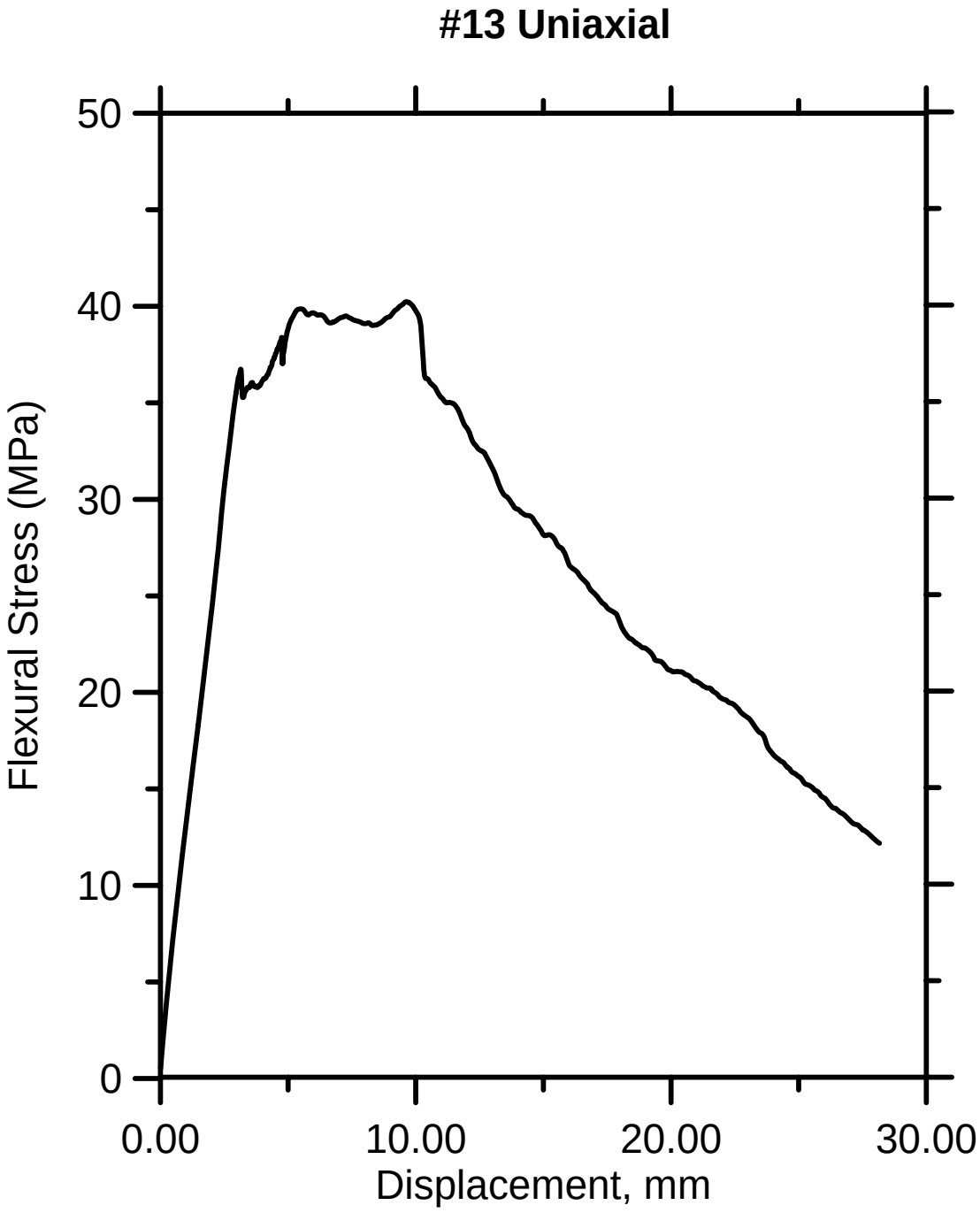
#13 Uniaxial
Flexural Stress (MPa)
50
40
30
20
10
0
0.00
10.00
20.00
30.00
Displacement, mm

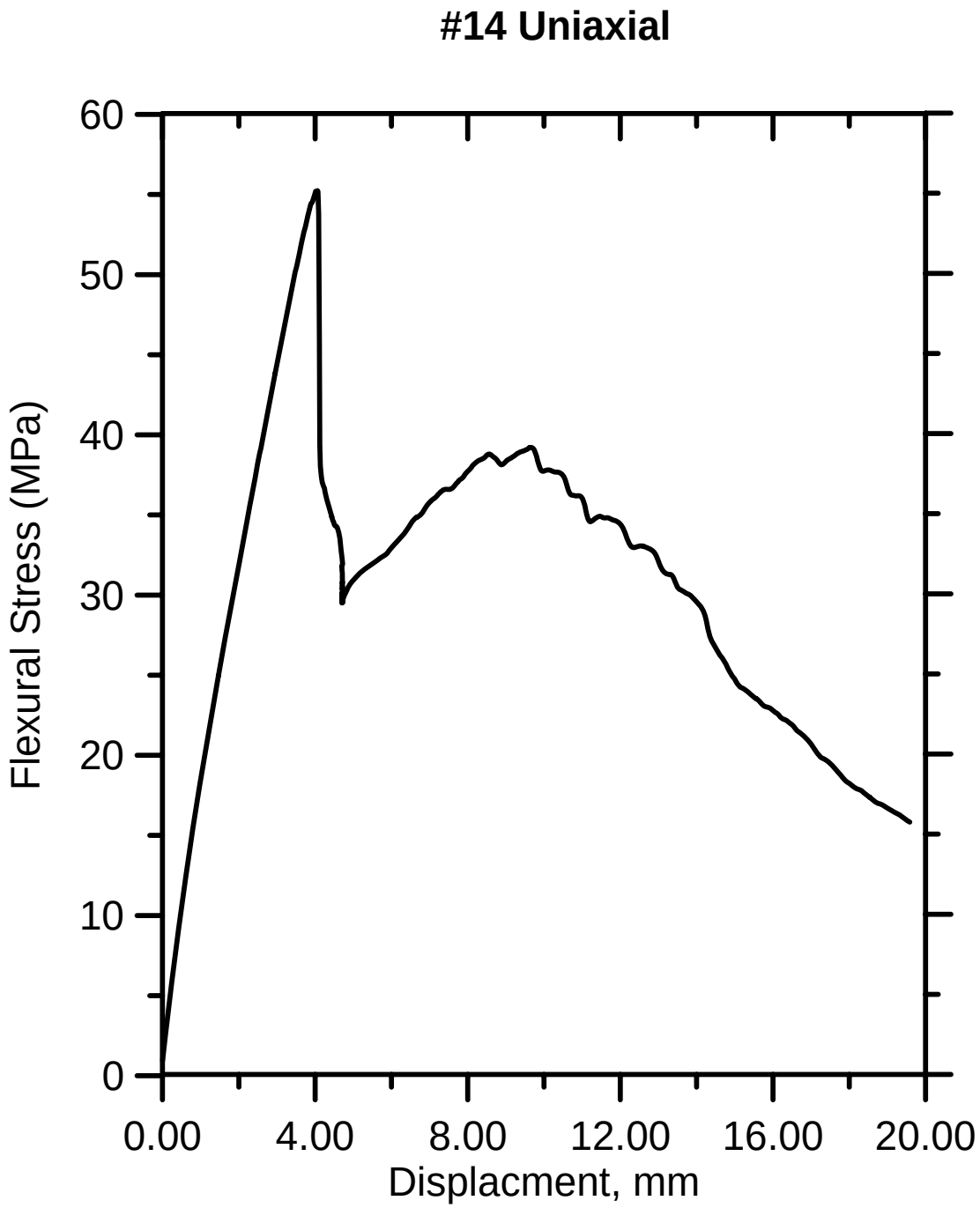
#14 Uniaxial
Flexural Stress (MPa)
60
50
40
30
20
10
0
0.00
4.00
8.00
12.00
16.00
20.00
Displacment, mm

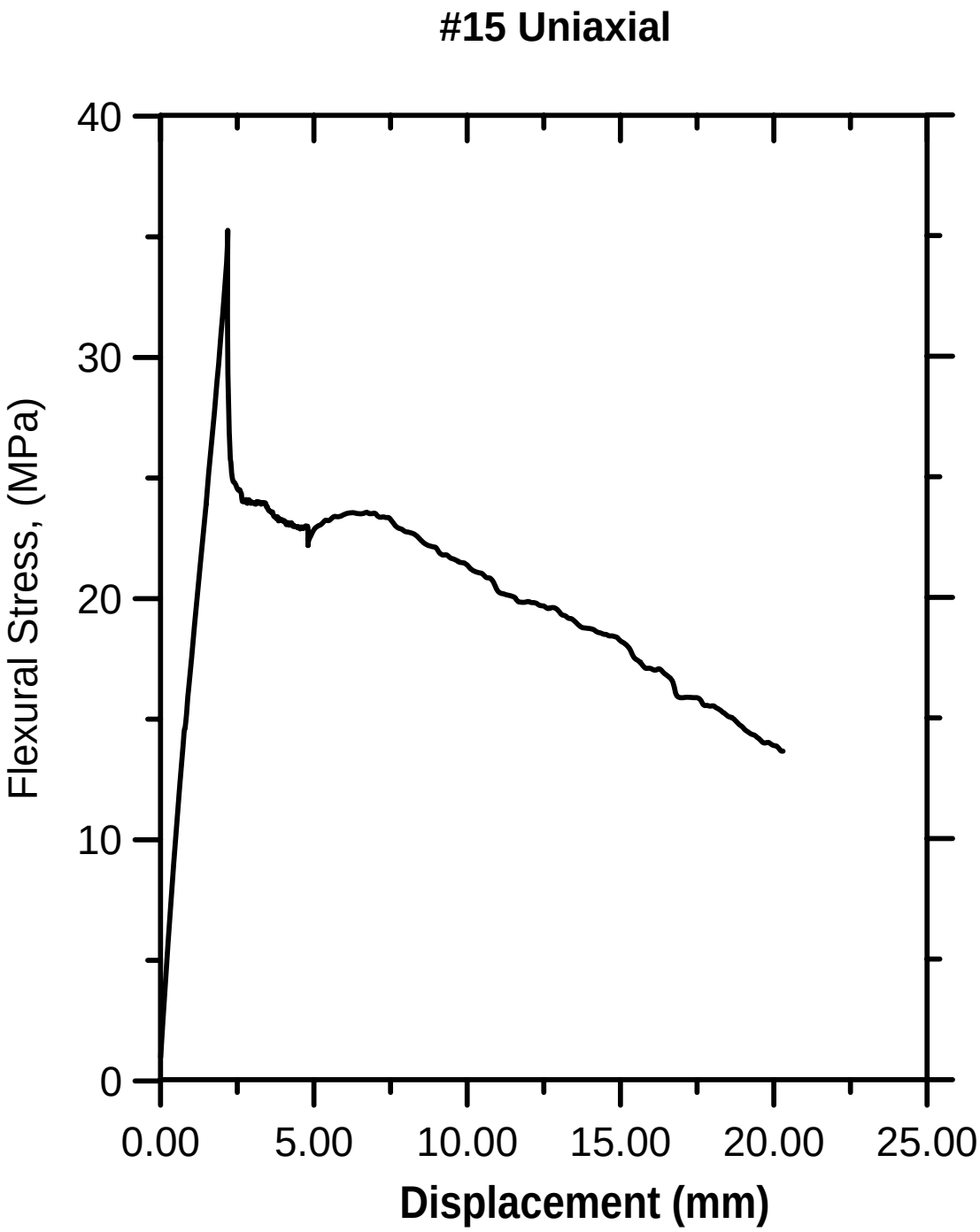
#15 Uniaxial
Flexural Stress, (MPa)
40
30
20
10
0
0.00
5.00
10.00
15.00
20.00
25.00
Displacement (mm)

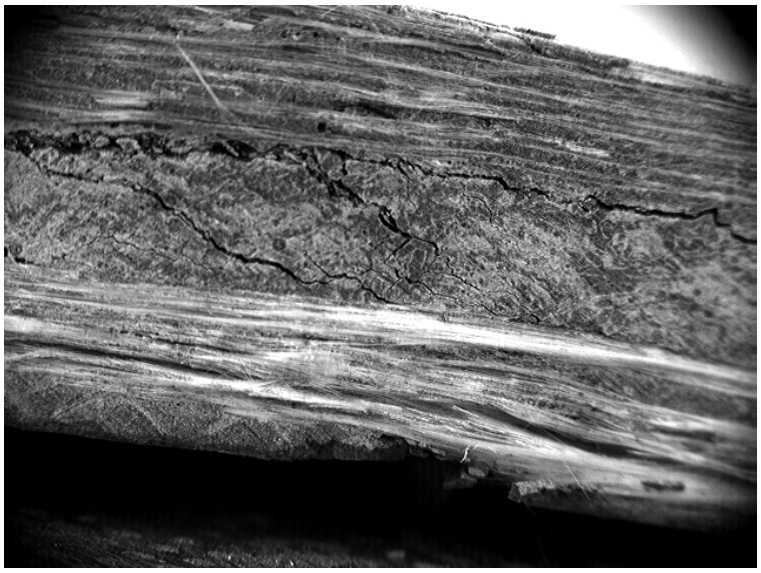

all dimensions in mm